Determination of the Nose Cone Shape for a Large Reusable Liquid Rocket Booster

by

ROBERT LAUREN ACKER

B.S., Massachusetts Institute of Technology
1987

SUBMITTED IN PARTIAL FULFILLMENT
OF THE REQUIREMENTS FOR THE
DEGREE OF

MASTER OF SCIENCE IN
AERONAUTICS AND ASTRONAUTICS

at the

MASSACHUSETTS INSTITUTE OF TECHNOLOGY

February 1988

Signature of Author ____________________
Department of Aeronautics and Astronautics
January 12, 1988

Reviewed by ____________________
C. P. Rubin
Hughes Aircraft Company

Certified by ____________________
Prof. Walter M. Hollister
Thesis Supervisor, Department of Aeronautics and Astronautics

Accepted by ____________________
Prof. Harold Y. Wachman
Chairman, Department Graduate Committee
Department of Aeronautics and Astronautics

Determination of the Nose Cone Shape for a Large Reusable Liquid Rocket Booster

by

Robert L. Acker

Submitted to the Department of Aeronautics and Astronautics
in partial fulfillment of the requirements for the degree of
Master of Science in Aeronautics and Astronautics
January 15, 1988

Abstract

Recently there has been a lot of interest in making reusable space vehicles in an effort to lower launch costs. In addition, the use of liquid propellant in a multistage vehicle provides for the maximum performance. This study examines the forces on the nose cone of the first stage of such a rocket and uses them to determine the best shape for the nose cone. The specific stage looked at is a strap-on booster on a design proposed at Hughes Aircraft Company.

This study consists of extensive literature searches and the use of theories and correlations with past data to determine ascent drag, nose cone mass, reentry heating, and water impact forces. Because no previous research has been done on the water impact of a vehicle with such a small ballistic coefficient, a model was constructed using Froude scaling laws and tested to determine the vehicle dynamics on impact.

The results show that for nose cone geometry with survivable water impact forces, the buoyancy forces not only become very large, but also cause the booster to rebound and experience a second impact. It was determined that a collapseable nose cone was necessary and drag, mass, and heating effects were used to obtain a shape. For a non-ablating nose cone this was found to have a tip radius equal to 73% of the base radius and a half angle of 20°. Preliminary analysis was done to determine the added penalties of using an ablative heat shield, and it was found that the benefits of reduced drag on a nose cone with a smaller angle outweighed the penalties of increased mass. If manufacturing costs are within reason, it was determined that the best nose cone shape is a completely ablative cone with a half angle of just under 15° and a small hemispherical tip.

Thesis Supervisor: Walter M. Hollister
Professor of Aeronautics and Astronautics

Contents

List of Figures

List of Tables

Chapter 1

Introduction

The United States is currently at a crossroads in its space program. As man's access to space steadily increases, so does the need for a launch vehicle which will take large payloads to orbit as cheaply as possible. In order to allow "customizing" of different payloads to their particular mission requirements, a launch vehicle with a varied number of strap-on boosters is one solution. In addition, making both the core and boosters liquid propellant allows them to achieve a maximum I_{sp}/performance. Finally, by making the boosters reusable, there is a potential for a large cost savings.

This study explores the problem of determining the shape of the nose cone on such a booster. The basic geometry of most nose cones can be summarized as shown in Figure 1.1. Here r is the tip radius, θ is the nose cone half angle, ϕ is the frustum half angle, and R is the base radius. (In order to simplify the calculations, most of the configurations analyzed will be simply a cone with a hemispherical tip.)

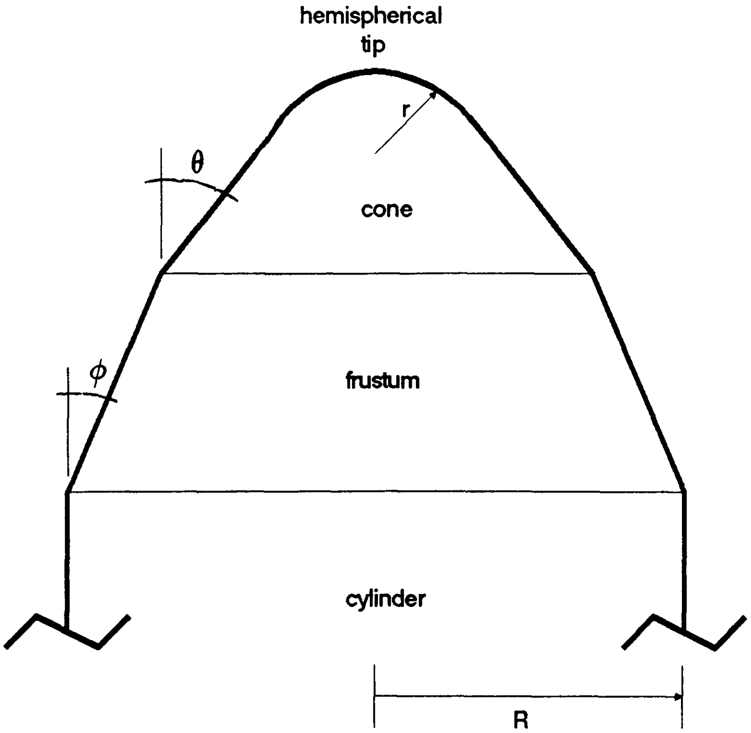

Figure 1.1: **Nose Cone Geometry**

In order to properly determine a shape, each stage of its trajectory must be looked at closely. During the ascent stage the performance of the launch vehicle is obviously of prime importance. It can be improved by reducing both the aerodynamic drag on the booster and the nose cone weight. During descent the goal is to insure the reusability of the booster. The high heating must thus be kept low enough to maintain its structural integrity. In addition, the booster will land in the ocean nose-first in order to help protect the engines from salt-water contamination. Therefore, the nose cone must be able to both withstand the impact loads and provide a favorable influence on the post-impact vehicle dynamics. In order to come up with a specific nose cone shape, the influence of various shapes on ascent drag, weight, reentry heating, and water impact must be analyzed. When the effect of drag on vehicle performance and the effects of reentry heating and water impact on booster reusability are each determined, a range of "acceptable" nose cone shapes can be defined from which an optimum can be chosen.

This problem is a unique one which has never been analyzed in its entirety before. Though the Space Shuttle Solid Rocket Boosters (SRB's) are a reusable booster, they are separated at a relatively low altitude, after which their nose cones are detached and they impact the ocean nozzle-first. In addition, they use solid rocket propellent, and only the outer shell is reused after an extensive (and expensive) refurbishment. Though some missiles are designed to leave the atmosphere and then reenter, there is little concern for insuring either their structural integrity on impact or their reusability. Early manned launch vehicles were obviously designed to return to Earth, but the shape determination problem was solved by optimizing for ascent, and then just reentering a small portion (capsule) of the vehicle in the reverse direction to minimize heating. In addition, these vehicles and capsules were never reused.

The only study the author could find on optimizing the shape of a launch vehicle nose cone dealt with the Saturn V fairing. In a report entitled "Launch Vehicle Nose Shroud Optimization" [1], E. S. Hendrix and D. L. Baccus determined which factors had the greatest effect on vehicle performance and approximated the best shroud shape for a given sized payload. They analyzed nose cones consisting of simple cones, cones with frustums, and cones with frustums and cylindrical extensions. The latter were used to allow a larger payload, something unnecessary in a booster. They found that the time the nose cone, or shroud, is jettisoned has the greatest influence on the vehicle's performance. Nose cone drag and weight also played a role, but their relative effects were dependent on the jettison time. If the shroud is jettisoned early, a nose cone with a small half angle was found to be best since it minimized drag, but was not on long enough for its mass to have much of an adverse effect on the performance. On the other hand, if the shroud is left on for most of the flight, the importance of the weight soon overtakes that of drag, and a large cone angle is best. (This latter condition is most like that of the reusable booster.) Because of the need to pack payload under the shroud, the optimum nose

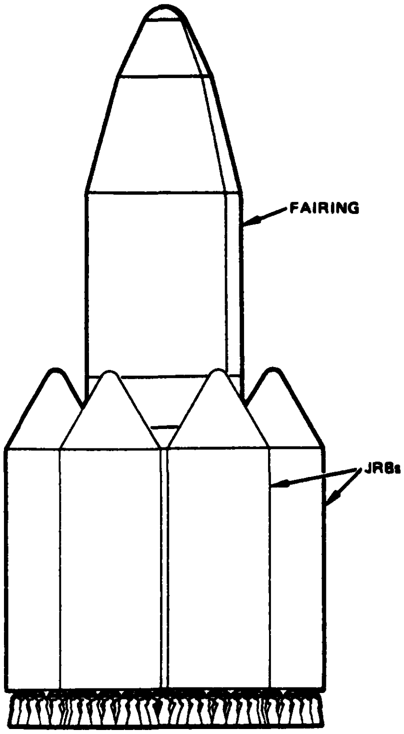

Figure 1.2: **Jarvis Launch Vehicle Configuration**

cone eventually derived had a nose cone half angle of 25° (which minimized weight — see Table 2.1) and a frustum half angle from 5° to 15° depending on the total volume of the shroud. The volumes above a certain limit required that a cylindrical extension be added to the cone.

The specific booster which will be analyzed in this study is called the Jarvis Recoverable Booster, or JRB. More like a first stage, it is part of the Jarvis Launch Vehicle (JLV) currently being studied by Hughes Aircraft Company's Space and Communications Group. The launch vehicle in its largest configuration with six JRB's is shown in Figure 1.2.

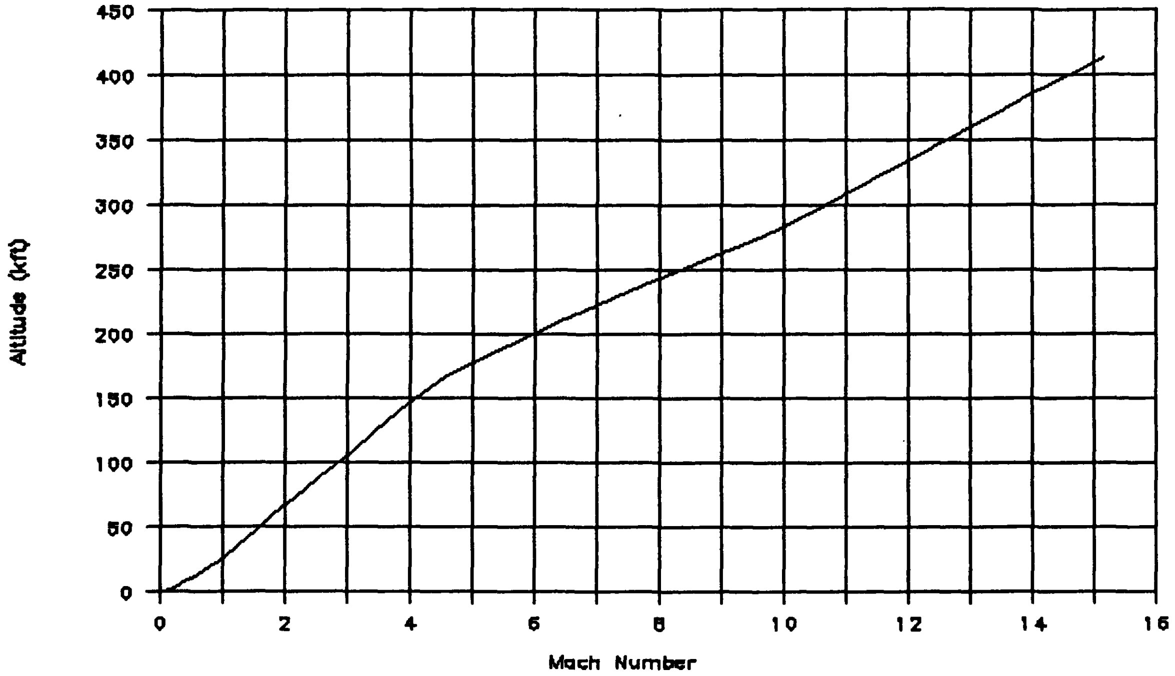

Figure 1.3: **Mach Number Versus Altitude**

The trajectory of this six strap-on case will be used as a worse-case in order to analyze the JRB nose cones. Because of the loaded vehicle's great mass, during the first part of the flight it moves quite slowly, gradually building momentum. This has the effect of allowing it to leave the dense part of the atmosphere before building up speed and increasing drag. (See Figures 1.3 and 1.4.) As seen in Figure 1.3, the JRB's are separated at a height of over 400 kft and at a speed of 13,600 ft/sec. It is thus obvious that reentry heating should play a larger role in the nose cone design.

The JRB's themselves are shown in Figure 1.5. The nose cone shown is a 30.5° cone with a tip radius of 30 inches, and will be used as the nominal case in this report. As the figure shows, there are many small liquid propellant engines on the

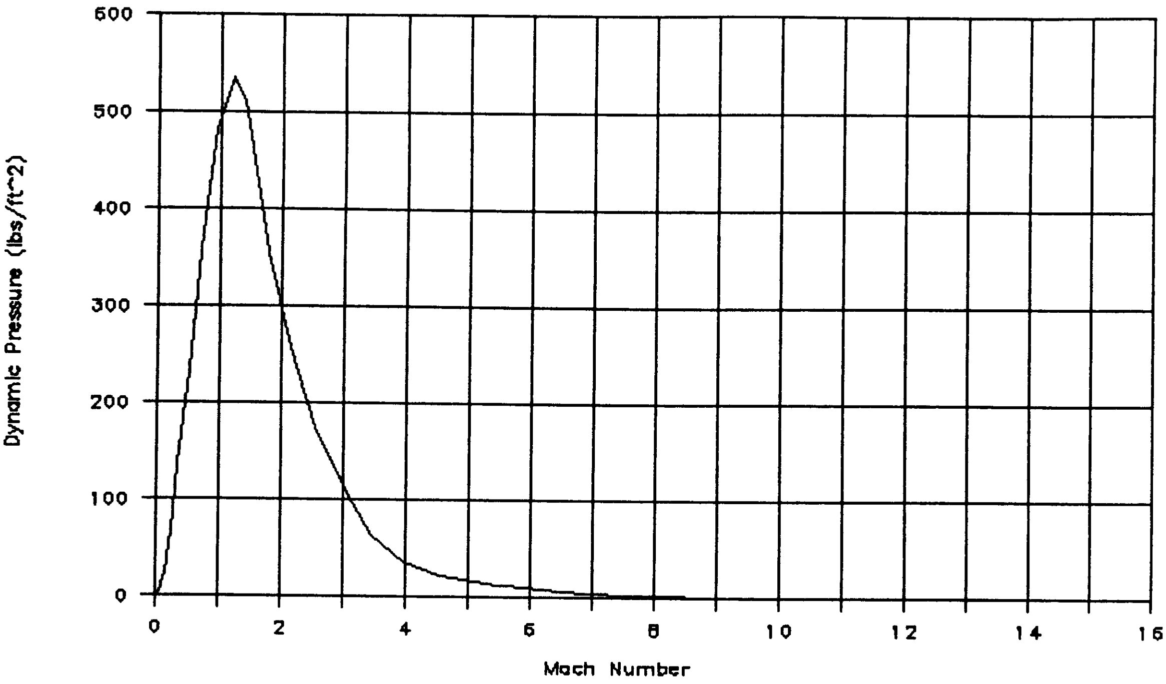

Figure 1.4: **Mach Number Versus Dynamic Pressure**

bottom of the booster. These require special care, especially during water entry, to keep them from getting damaged or contaminated by the sea water. The mass of the entire booster after staging will be approximated at 60,000 lbs, with the weight of the engines causing the center of mass to be located in the rear, as shown in Figure 1.5.

In this analysis it is assumed that the JRB's follow an ascent trajectory like that just discussed, after which they separate and return to earth in a ballistic trajectory. Along this trajectory some sort of control system, such as a deployable device or a monoprop attitude control system, is used to keep the velocity vector in line with the booster's longitudinal axes. Each booster will land in the ocean and remain there for up to several hours until a surface ship can recover them. Because of their

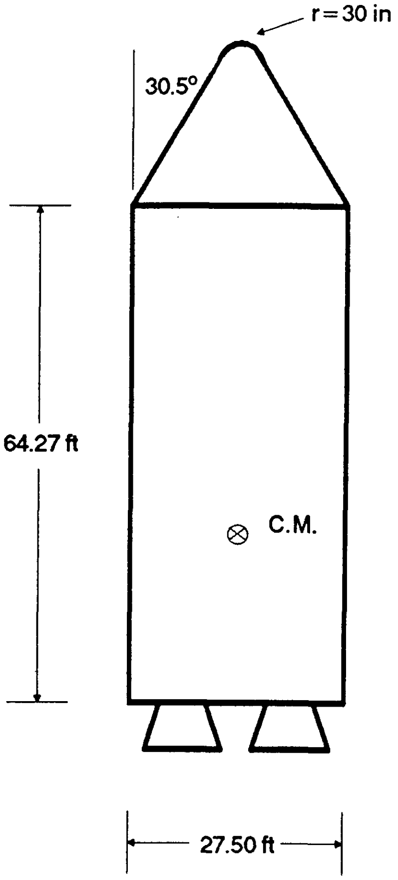

Figure 1.5: **Jarvis Recoverable Booster Geometry**

buoyancies and the location of their centers of mass, they will float on their sides, and a suitable method for keeping the engines from getting wet is assumed to have been devised.

Finally, as part of the design for a low-cost reusable booster, the nose cone must help meet the following design goals:

- Low design and construction costs
  - Simple design
  - Existing technology and materials
- Minimum Refurbishment
  - No or minimal ablation
  - Survivable impact loads (for the booster)
  - Integrity of structure (if possible)
- Reliability
  - No active parts
  - Maximum possible failure tolerance

Note: In this study, equations have been obtained from a wide range of sources. An attempt has been made to consolidate the variables used as much as possible and to define them when they are first introduced. In addition, a nomenclature section has been included as Appendix A.

Chapter 2

Ascent: Drag and Mass

2.1 Introduction

The purpose of the JRB's is to provide the most efficient boost possible, allowing the rocket to take up the most payload mass. The shape of the booster nose cones can affect this in two ways: through their mass and through their contribution to the vehicle's total aerodynamic drag. An "ideal" nose cone would provide both the minimum aerodynamic drag and the minimum weight for a given base diameter. Since these two criterion cannot be met simultaneously,[1] the importance of each must be determined by first finding the relationships that drag and booster mass have to the total payload mass to orbit. These relationships can then be used to design an optimal ascent nose cone. This chapter will begin by examining the

---

[1] For example, the minimum weight nose cone is simply a disc, which has a very high pressure drag.

role drag and nose cone weight play in vehicle performance. Next drag theory with respect to rockets at various Mach numbers will be looked at. Finally, some theories of optimum aerodynamic shapes and the computation of drag and mass for specific shapes and configurations will be covered.

2.2 Vehicle Performance

2.2.1 Drag

The performance of a rocket can be approximated by several simple equations. First, summing up the equations of motion (assuming no lift and an angle of attack of zero):

$$T' - D - Mg\cos\alpha = M\frac{dV}{dt} \tag{2.1}$$

with T' = thrust, D = drag, M = booster mass, α = the angle between the rocket's longitudinal axis and the vertical, and V = velocity. The rocket equation is

$$T' = \dot{m}u_e + (P_e - P_a)A_e \tag{2.2}$$

with $\dot{m}$ = the mass flow rate of exhaust, u = exhaust velocity, P = pressure, A = cross-sectional area, and the subscripts e and a referring to conditions at the exit plane of the engine nozzle and in the atmosphere, respectively. Using $dM/dt = -\dot{m}$, assuming I_{sp} = constant[2] so $u_e = I_{sp}g$, and assuming a matched condition[3] with $P_e = P_a$,

$$T' = -\frac{dM}{dt} I_{sp} g_o$$

Drag is defined as

$$D = \frac{1}{2}\rho V^2 C_D A.$$

Because

$$g = g_o(\frac{R_e}{R_e + y}) = .96 g_o,$$

at the altitude of booster separation (y = 413 kft) one can approximate $g \approx g_o$ for the full flight and Equation 2.1 becomes:

$$M\frac{dV}{dt} + \frac{dM}{dt} I_{sp} g_o + \frac{1}{2}\rho V^2 C_D A + M g_o \cos\alpha = 0$$

Rearranging terms and integrating with

$$\frac{1}{M}\frac{dM}{dt} = \frac{d}{dt}(\ln M),$$

$$V_f + \ln(\frac{M_f}{M_o}) I_{sp} g_o + \frac{A}{2}\int \rho V^2 C_D \frac{1}{M} dt + g_o \overline{\cos\alpha} = 0 \qquad (2.3)$$

where V_f = final velocity (the initial velocity is assumed to be zero), M_f = remaining total mass of core and structural mass of boosters right before separation, M_o = initial total mass of rocket, and $\overline{\cos\alpha}$ is the average value of $\cos\alpha$ integrated over

---

[2] According to Reference [2], I_{sp} usually increases by less than 20% over the altitude increase of the flight.

[3] According to Reference [2], if $\dot{m}$ is constant the thrust varies by less than 20% between sea level and high altitude.

time. Defining

$$\eta = \frac{1}{2}\int \rho V^2 \frac{1}{M} dt,$$

M_{PL} = payload mass, t_B = total ascent burn time, $M'_f = M_f - M_{PL}$, and assuming that C_D = constant, Equation 2.3 becomes:

$$M_{PL} = M_o e^{-\frac{1}{I_{sp}g_o}(AC_D\eta + g_o t_B \cos\alpha + V_f)} - M'_f \tag{2.4}$$

In this equation, the term V_f is much larger than $AC_D\eta$. The drag coefficient thus plays just a small roll in the exponential, and eventually the value of M_{PL}.

The drag term in Equation 2.3 can also be rewritten following the technique of Reference [2] by nondimensionalizing the integral:[4]

$$\frac{1}{2}A\int \rho V^2 C_D \frac{1}{M} dt = \frac{t_B \rho_{ave} V_f^2}{M_o/A}\int_0^1 C_D \frac{M_o}{M}\left(\frac{V}{V_f}\right)^2 d\left(\frac{t}{t_B}\right) \tag{2.5}$$

Since M_o/A is large for the JLV, the drag penalty is reduced. In addition, these equations assume constant thrust, however the JLV moves fairly slowly through the lower denser regions of the atmosphere, thus effectively reducing ρ_{ave} and the drag penalty.

The only way to get an exact relationship between drag and payload to orbit is to use a numerical solution of Equation 2.1. This was done for the JLV by David Russ, using a trajectory program at Hughes Aircraft Company. By using a multiplier to vary the drag penalty he was able to get a corresponding value of payload to orbit. The four data points obtained are shown in Figure 2.1. Computing

---

[4] See Reference [2], pages 3 to 16.

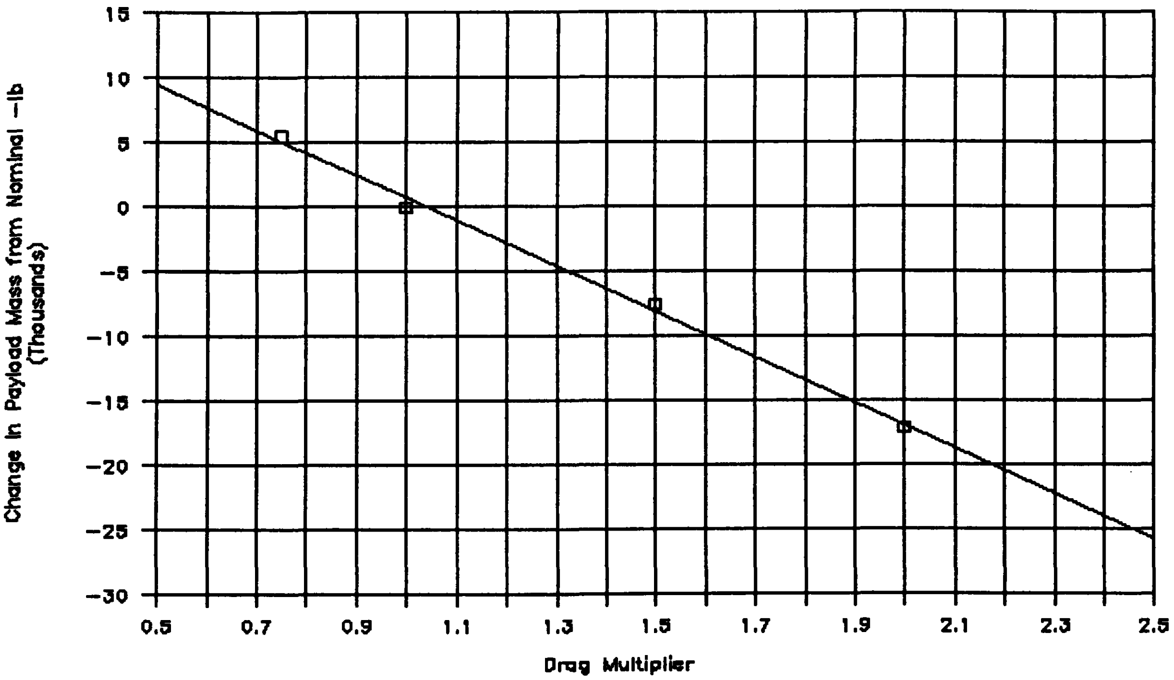

Figure 2.1: **The Effect of Drag on Payload Mass to Orbit**

a linear regression on these points, the change in payload mass is found to vary with the drag multiplier (K_D) by the equation:

$$\Delta M_{PL}(\text{lbm}) = -17,613.1(K_D) + 18,357.1 \tag{2.6}$$

This line is also shown in Figure 2.1. However, since by definition when the drag multiplier is zero $\Delta M_{PL} \equiv 0$, and by Equation 2.6, $\Delta M_{PL}(0) = 744$ lb, this equation does not give results accurate to less than ~ 1000 lb.

2.2.2 Nose Cone Mass

The effect each JRB's nose cone mass has on the total payload to orbit will now be explored. Neglecting gravity and drag, Equation 2.1 from the previous section can be rewritten as

$$T' = M\frac{dv}{dt}.$$

Now, using

$$\frac{dM}{dt} = -\dot{m},$$

defining

$$c = u_e + \frac{(P_e - P_a)A_e}{\dot{m}},$$

and using Equation 2.2, this becomes

$$\frac{dV}{dt} = -\frac{dM}{dt}\frac{1}{M}c = -c\ln\frac{dM}{dt}.$$

Integrating gives the basic equation of rocket performance:

$$\Delta V = c\ln\frac{M_o}{M_f}.$$

Since this is a two stage booster, each stage of which contributes a ΔV, the equation is actually of the form

$$\Delta V = c_1\ln\frac{M_{o_1}}{M_{f_1}} + c_2\ln\frac{M_{o_2}}{M_{f_2}}. \tag{2.7}$$

Defining M_{NC} as the change in mass of a JRB nose cone from the nominal, $M_{o_1} =$ total nominal vehicle loaded mass $+\ 6M_{NC}$, $M_{o_2} =$ total second stage loaded mass (including payload), $M_{f_1} = 6\times$ (strap-on structural mass) $+\ M_{o_2} + 6\ M_{NC}$, and $M_{f_2} =$ second stage structural mass + payload mass. Since $M_{o_1}/M_{NC} \approx 5000$ if the nose cone weight was more than doubled, and $M_{o_1} \cong 5M_{f_1}$, $M_{o_1} > M_{f_1} \gg M_{o_2} > M_{f_2}$, and $M_{o_2}/M_{f_2} \gg M_{o_1}/M_{f_1}$, increasing or decreasing M_{NC} by a small amount with a constant ΔV will have a minor effect.

This problem was also looked at by David Rušs using the Hughes trajectory program to iterate on Equation 2.1. Varying the JRB weights and computing the corresponding weight to orbit showed that for every one pound gain in *each* JRB, the corresponding payload weight was reduced by 1.80 lbs.

2.3 Aerodynamic Drag

2.3.1 Components of Drag

There are a variety of ways of dividing the drag operating on the vehicle into several components. These in turn provide an easier, more systematic way of evaluating the total drag. The most common method is to divide the drag force into tangential and normal forces. The tangential force is called viscous, or skin friction drag, since it is caused by the viscosity of the air. As shown by Nielson [3, p. 262], when S is the total surface area of the rocket, V_∞ is the free-stream velocity, $\hat{t}$ is the unit tangential at a point on the rocket, and τ is the local skin friction per unit area, the skin friction drag is

$$D_f = \iint_S \tau \cos(\hat{t}, V_\infty)\, dS. \tag{2.8}$$

The normal component of the drag force is called the pressure drag, and is caused by the pressure forces on the rocket. When P is the pressure and $\hat{n}$ is the unit normal, it can be written as

$$D_p = -\iint_S P \cos(\hat{n}, V_\infty)\, dS. \tag{2.9}$$

The pressure drag itself is often subdivided into base drag and pressure foredrag. The base drag is the drag on the rear of the rocket, and is almost exclusively pressure drag. This is due to the fact that the flow coming off the sides of the rocket enters the stagnated region behind it, exciting this stagnated air and attempting to pump it away, thereby reducing its pressure. Pressure foredrag, which will hence simply be called pressure drag in this discussion, is the non-viscous drag on all of the rocket's surface except the base. Each of these components of drag behaves very differently in subsonic, transonic, and supersonic flow, and over differently shaped bodies. They will each now be discussed relative to a body of revolution like a rocket.

Skin Friction Drag

Caused by the viscosity of the atmosphere, skin friction drag varies widely depending on the flow conditions around the body. Though it is the primary drag force at low Reynolds numbers, for a rocket its value is typically a small fraction of the total drag. Its effects are confined to the boundary layer of air which viscosity holds around the surface of the rocket. As such, it is influenced by the conditions in this boundary layer. The skin friction is related to viscosity and the velocity gradient by the equation

$$\tau = \mu \frac{du}{dy} \tag{2.10}$$

where μ is the absolute viscosity. In order to describe how these terms affect the skin friction, it is important to first specify the different flow conditions in the boundary layer.

A boundary layer can be classified as either laminar, transitional, or turbulent. A laminar boundary layer is characterized by parallel flow with locally constant velocities. As the Reynolds number is increased, a point is reached where the viscous forces lose their "hold" on the air layer and the dynamic forces begin causing turbulent oscillations in the flow. These eventually dominate, and the momentum exchange now occurs in large blocks of air, increasing the skin friction.

In laminar boundary layer flow the skin friction is often approximated by the equation[5]

$$C_{f_{lam}} = 1.328/\sqrt{R_l}$$

where $C_{f_{lam}}$ is the average coefficient over a surface, defined by

$$C_{f_{lam}} = D_{lam}/(qS),$$

and

$$R_l = Vl\rho/\mu \equiv \text{Reynolds number of the body dimension } l.$$

Thus, up until the transition region, the skin friction on the accelerating rocket decreases with increasing velocity. As pointed out by Hoerner [4, p. 17–4], the density and temperature have a very minor effect.

---

[5] See Reference [4], page 2–4.

The transition region is defined by a transition Reynolds number, above which turbulent effects change and complicate the prediction of C_f. Because of this, a good theoretical equation for C_f has not been found. The equation most often used[6] is that of Schoenherr,

$$\log(R_l C_f) = 0.242/\sqrt{C_f},$$

which is closely approximated by Schultz-Grunow's equation:

$$C_f = 0.427/(\log R_l - 0.407)^{2.64} \tag{2.11}$$

In a turbulent boundary layer there is an increase in temperature as the kinetic energy of the free-stream is reduced around the body. This has two effects. The first is to increase the viscosity according to the Sutherland formula,[7] which approximates μ as a function of the temperature T:

$$\mu = \mu_{ref}\left(\frac{T}{T_{ref}}\right)^{\frac{1}{2}}\left(\frac{1 + const./T_{ref}}{1 + const./T}\right).$$

The second is to decrease the density by the ideal gas law

$$\rho = P/RT.$$

As explained in Reference [3], this reduction in density couples with the increase in viscosity to reduce R_l, which in turn causes an increase in the boundary layer thickness. In such a thicker boundary layer du/dy is reduced more than the temper-

---

[6] See Reference [4], page 2–5.

[7] See Reference [5, p. 23]

ature raises μ, and by Equation 2.10, the skin friction is decreased.[8] Thus, although in a turbulent boundary layer the skin friction is initially much greater than in a laminar boundary layer, it falls both do to increasing velocity/Mach number and the corresponding temperature increase. Cooling the nose cone of a rocket is thus one way to reduce C_f in the turbulent regime. However, the best solution is to provide as stable a boundary layer as possible, in other words, raising the transition Reynolds number (R_{tran}) to as high a value as possible.

Experimentation has shown that usually $R_{tran} \approx 10^6$ for a flat plate. By using a conical shape, the boundary layer is constantly thinned flowing along it. This will stabilize the boundary layer so that R_{tran} can approach 10^7. (See Fig. 4, p. 17–4 in Reference [4].) In transonic and supersonic flow over ogival and parabolic shapes, Prandtl-Meyer expansion occurs around the bodies. This causes negative pressure gradients, which further stabilize the boundary layer and allows R_{tran} to pass 10^7 at Mach numbers above three or four. (See Fig. 5, p. 17–6 in Reference [4].) Finally, surface roughness can also trigger turbulent flow, so a smooth surface is desired.

Base Drag

As previously described, base drag is caused by the boundary layer coming off of the back of the cylinder and mixing with the stagnated air behind the base. Besides causing turbulence at the end of the rocket or booster, this flow also pulls the air

---

[8] This effect does also happen in a laminar boundary layer, but to a much lesser degree.

away in a jet-like motion. This rear-pulling force is the base drag. Defining the base drag coefficient as

$$C_{DB} = D_{base}/(qA),$$

when it is compared to the Mach number it is found that C_{DB} rises to a peak at $M = 1$, stays relatively constant until about $M = 2$, and then constantly falls as the Mach number increases. This can be partly explained in that compression shock waves begin to form at the rear of the booster at supersonic Mach numbers. Up until about $M = 2$, flow behind the last compression shock still returns to the base. At greater Mach numbers this backflow stops, and mixing from the boundary layer is reduced as the flow constricts behind the base, forming a conical shock wave. At this point base drag has become primarily wave drag [4, p. 16–6]. For subsonic speeds, base drag is usually calculated as a function of the skin friction of the forebody (C_{FB}), since this determines the boundary layer thickness which reaches the base. According to Reference [4], a typical relationship for a cylindrical body is

$$C_{DB} = .029/\sqrt{C_{FB}}.$$

Transonic values are usually obtained by comparing the subsonic value of C_{DB} to data plots of C_{DB} versus M. Supersonic values are taken from both plots and theory.

When a rocket is thrusting, its base drag is greatly reduced. This is because the thrust plume eliminates most of the stagnated air at the base of the vehicle. Predicting the small base drag which does occur in this situation is very difficult, for a thrusting rocket obviously does not lend itself well to windtunnel tests. In addition, most of the data that is available on this subject is classified.

Pressure Drag

The pressure drag has the largest resistive force on the body, and for subsonic speeds, like skin friction drag, it is also caused by the viscosity of the fluid. In a nonviscous fluid the flow would separate around the front of the rocket and then come back together again at the rear. Equation 2.9 would then be equal to zero. However, because air is viscous, the boundary layer around the rocket gradually loses velocity next to the structure and eventually stagnates, creating a vortex. This causes the flow to separate, and there is thus an incomplete pressure recovery. This difference in pressure over the rocket is the pressure drag. As Hoerner points out [4, p. 3–17], the pressure drag is greater the greater the angle at which the flow separates from the body. Thus, the smaller the angle of a cone (starting with a flat plate), the less the drag. In addition, pressure drag can be reduced by keeping the velocity gradient along the body as smooth as possible. This can be done by keeping the nose cone shape smooth, and adjusting it so that the angle between the nose cone and the body is reduced.

The characteristics of the flow change dramatically as the transonic regime is reached. This regime is defined as starting at the "critical Mach number," the Mach number of the external flow for which the local Mach number reaches 1 at some point on the surface. A shock wave then begins to form at the front of the rocket.

Across this shock wave entropy is increased, and heat is added both to the air and to the vehicle behind it. "As a consequence of viscosity within, and heat-transfer across a shock wave, a momentum deficiency is left behind, thus representing the equivalent of the 'wave drag' experienced by the obstacle."[9] If the body is slender, the weak shock wave will produce just a small increase in entropy, and thus less pressure drag. In this transonic regime the shock wave is detached from the body, and there is subsonic flow present around the body.

Defining the coefficient of pressure drag as

$$C_{DP} = D_{pressure}/(qA),$$

a combination of theoretical and practical results can be used to approximate it for flow over cones. When these are plotted compared to the Mach number, it is seen that C_{DP} is relatively small until about $M = .7$, when it begins to increase greatly. This increase stops between $M = 1.0$ and 1.5, and the drag steadily decreases as supersonic and then hypersonic flow is reached. (This relationship of C_D to Mach number is also very similar for ogival shapes.) When supersonic flow is reached around a cone, the shock wave attaches itself to the tip and becomes conical in shape. The shock wave has a half angle (obviously larger than that of the cone) which constantly shrinks as the velocity increases, thus reducing the pressure drag.

Prediction of C_{DP} is usually done using a combination of empirical data and

---

[9] From Reference [4], page 16–3.

theory. For subsonic flow, similarity rules like the Prandtl-Glauert law[10] are usually used. Axially symmetric flow is approximated with the similar Göthert rule. When the critical Mach number is reached it is necessary to revise these rules because of their linearity. The new form is known as the Von Kármán-Spreiter transonic similarity rule, and is valid from subsonic to supersonic velocities.[11] For hypersonic Mach numbers however, theory can provide approximate equations for pressure drag. To some degree of accuracy, they can also be used for supersonic flow. Such an equation is given in Reference [4] as

$$C_{DP} = 2\sin^2\theta + 0.5(\frac{\sin\theta}{\sqrt{M_\infty^2 - 1}})$$

(Here M_∞ is the free-stream Mach number.) Because equations like this have been derived for hypersonic flow, many people have used them to obtain minimum drag shapes for different parameters. In addition, conical flow theory can be used to evaluate the flow quantities around cones in supersonic flow, and slender body theory can be used at any Mach number. The latter is a potential flow theory and can be approximated as a series of linearized equations, which allows it to also be used to optimize shapes for minimum drag.

---

[10] See Reference [6], Section 12.3.

[11] See Reference [7], p. 258.

2.3.2 Shapes of Minimum Pressure Drag

The determination of the shape of a body with minimum pressure foredrag has been a classical problem of calculas of variations that mathematicians and aerodynamicists as far back as Newton have tackled. The basic proceedure is to use an aerodynamic theory to derive an equation for C_{DP} as a function of the body coordinate system. Next, an equation for either area or volume is derived as a function of body coordinates. End conditions from the body coordinate system can then by used to solve the problem of minimizing the equation for C_{DP} using the geometry equation as a constraint. This section will summarize the results obtained for bodies of revolution neglecting base drag. These results can be divided into two areas, the first (begun by Von Kármán) uses slender body theory, and the second uses Newtonian impact theory.

In his 1936 paper entitled "The Problem of Resistance in Compressible Fluids" [8], Von Kármán used slender body theory to derive the shape of a body with minimum pressure foredrag for a given length and base diameter. This is often called the Von Kármán Ogive in the literature. It is shown for a 27.5 ft diameter booster with a fineness ratio (τ) of 1.15 where

$$\tau \equiv \text{diameter/length}$$

(this corresponds to a 30° cone) in Figure 2.2.[12] Subsequent work by Parker [9] and then Ferrari [10] used a more elaborate streamline function to derive a minimum

---

[12] This was computed using data from Table 9–1 on page 284 of Reference [3].

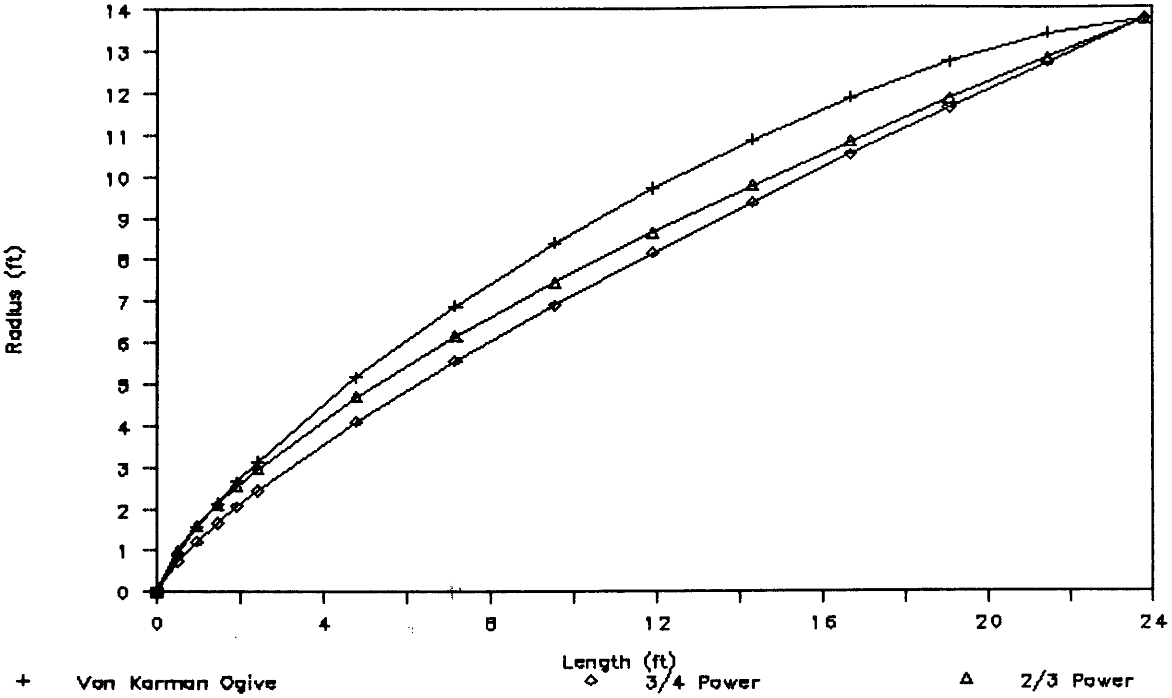

Figure 2.2: **Shapes with Minimum Pressure Foredrag**

C_{DP} shape. As Ferrari points out [10, p. 120], using the approximation $\sqrt{M_\infty^2 - 1} \times \frac{\text{radius}}{\text{length}} \ll 1$, his results reduce to those of Von Kármán. As the Mach number increases, the shock wave moves closer to the body and slender body theory becomes invalid. This is the region of hypersonic flow, which is best approximated by a Newtonian flow model.

The Newtonian flow model assumes that the shock wave has attached to the tip of the nose cone and obtained an angle equal to the body angle. As pointed out on page 186 in Reference [11], the pressure coefficients are calculated by assuming that "particles crossing the shock layer conserve the tangential component of velocity but lose the normal component." The Newtonian pressure law is thus

$$C_{DP} = 2\sin^2\psi \tag{2.12}$$

where ψ is the angle between the free-stream direction and the tangent to the body. Newton was probably the first to use these assumptions to calculate a minimum drag body. In 1957, Eggers, Resnikoff, and Dennis published a paper [12] using the Newtonian pressure law to calculate minimum drag shapes for a variety of given characteristics. They also showed that the shape can be closely approximated by a three-quarter power law of the form:

$$\frac{r}{R} = (\frac{l}{L})^n \tag{2.13}$$

with $n = 3/4$, r = distance from the axis of revolution, and l = distance from the tip of the nose cone. (This shape is shown in Figure 2.2.) Angelo Miele [11, Ch. 13] uses the assumption that the square of the slope of the body is much less than one to simplify the analysis done in Reference [12] so it can be applied to more conditions.

In Chapter 24 of Reference [11], Miele uses the Busemann correction to Newton's impact theory to compute minimum drag shapes. Busemann's correction takes account of the centrifugal forces in the fluid behind the shock wave when the curvature of the body is large. The formula appears in the following form:

$$C_{DP} = 2\,\sin\psi(\sin\psi + \frac{d\psi}{dA}\int_0^A \cos\psi\, dA) \tag{2.14}$$

Eggers et al. [12] also used this Busemann correction in the "results" section of their report to compare it to the Newtonian shape. Both reports found that the shape obtained when the length and diameters were given was blunter at the tip than the Newtonian shape, but then experienced more curvature downstream. In Reference [13] this shape is shown to be closely approximated by a two-thirds power law (Equation 2.13 with $n = 2/3$), which is shown in Figure 2.2. As Eggers et al. point out however, the method of characteristics shows that the Newtonian-Busemann equation tends to overestimate these centrifugal effects. However, experimental data [13, p. 103] shows that the power law predicts a minimum drag shape when n is between 1/2 and 3/4. In addition, as can be seen in Figure 1.4, the JLV experiences peak dynamic pressures at Mach numbers in the transonic range, and Equation 2.12 is not accurate in that range.[13]

As pointed out in Reference [3], a comparison between the Von Kármán and the Newtonian bodies was carried out by Jorgenson [14]. He found that the latter had lower calculated drags in all regions including the supersonic region, where it is not theoretically correct. However, the differences were fairly minor.

Though these minimum drag shapes can have a beneficial effect on the performance of the rocket, they must be analyzed to determine if this justifies the increase in manufacturing cost. As a rough outline, Reference [4, p. 16–21] states that a cone has a pressure foredrag about 10% less than that of an ogive with the same

---

[13] Reference [12] states on page 3 that Equation 2.12 is "unacceptably poor" when the hypersonic similarity parameter K is less than 1, and $K = M_\infty 2R/L$.

length. By moving to a minimum drag shape, this drag can be reduced by about another 10%. Eggers, Resnikoff, and Dennis [12, p. 8] present test data which shows that for smaller fineness ratios the reduction in drag obtained by moving from a cone to a 3/4 power body is a little less than 10%.

2.3.3 Computing Drag

In order to determine how different nose cones affect the launch vehicle performance, it is necessary to first compute both the drag of the complete launch vehicle and how different nose cone geometries change this total drag. This was done using a combination of theory and experimental data found in the literature.[14]

The launch vehicle drag can be divided into several categories, as mentioned in Section 2.3.1. These are forebody pressure drag, skin friction drag, and base drag. In order to more easily calculate these values, the drag on the fairing and each booster was calculated separately and then added together. It should be noted however that a body's total drag is not simply the sum of its components. Their proximity to each other causes an "interference drag" in subsonic flow. In order to properly approximate this, windtunnel tests would have to be run on an exact model of the configuration. Because of this, and the assumption that the interference drag does not vary any measurable amount for different nose cone shapes, it was ignored. For supersonic flow however, the proximity of the boosters and the core will actually

---

[14] The methods used ignore the effects of lift by assuming an angle of attack of zero.

be beneficial, since the shock wave off of the fairing will prevent the free-stream from coming into contact with part of the booster nose cones. This effect was accounted for by estimating that only two-thirds of each booster was exposed to the free-stream.[15]

The base drag was assumed to be essentially the same for both the boosters and the core. As mentioned on page 31, predicting the base drag for a thrusting rocket is very difficult. In this case it was assumed that C_{DB} reaches a peak value of .07 at the beginning of the supersonic regime.[16] Using this value as a start, a table of C_{DB} versus Mach number was derived using data like that found on page 16–4 in Reference [4]. This data is plotted in Figure 2.3. It can be seen that C_{DB} is quite small, and even if it were changed by as much as 30%, it would have little affect on the total drag. In addition, it should be pointed out that the base drag is approximated as the same value for each different nose cone. What little difference exists is assumed to be within the error of the calculations.

The skin friction drag and pressure foredrag were both calculated for various Mach numbers by using Reference [15]. Called the *U.S.A.F. Stability and Control Datcom,*[17] it is a tool for estimating drag on a variety of shapes by using data and theories from a large number of references. For subsonic drag the skin friction drag is found by first finding the turbulent flat-plate skin friction coefficient with a series

---

[15] This estimate was provided by C. P. Liu at Hughes Aircraft Company.

[16] The author is also greatful to C. P. Liu for this approximation.

[17] The word Datcom stands for data compendium.

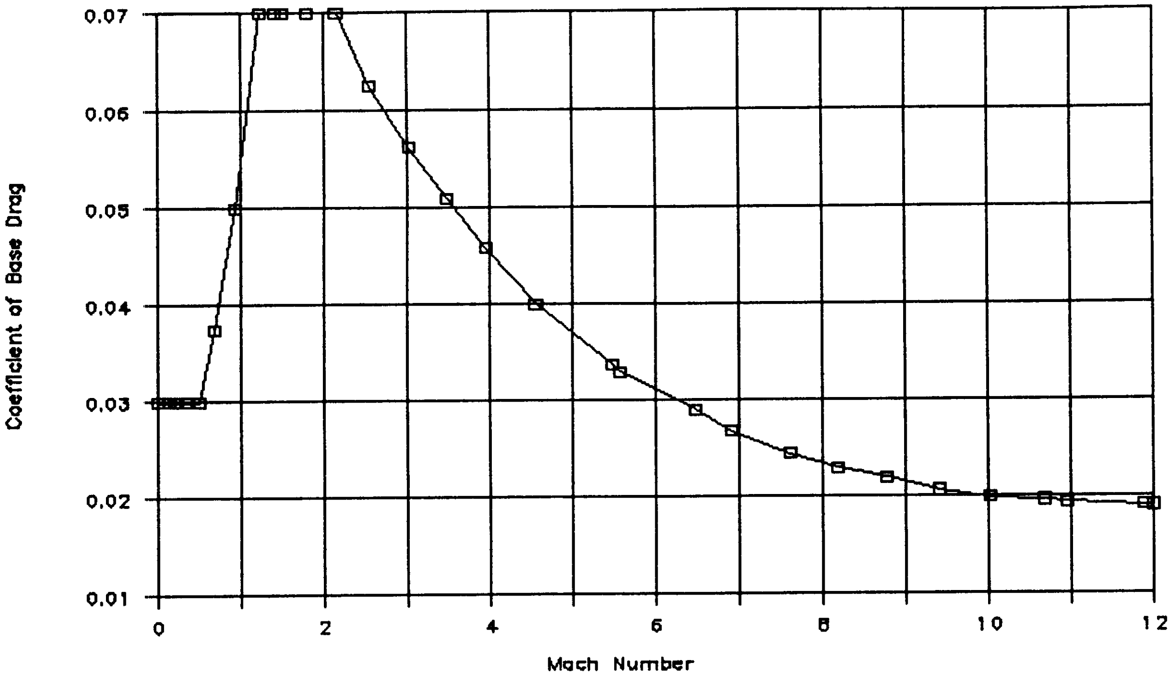

Figure 2.3: **Relationship of Basedrag to Mach Number**

of charts. (Even though laminar flow should be striven for, as previously mentioned, the *Datcom* assumes turbulent flow since the transition Reynolds number is very hard to predict.) These charts were found to very closely follow Equation 2.11, multiplied by the factor $(1 + 0.15M_\infty^2)^{-.58}$ to account for the compressibility of the flow.[18] The formulas were thus used instead of the charts. The values of C_f for a flat plate derived were multiplied by $(1 + \frac{480}{(L/R)^3}) \times S/S_B$ to obtain C_f for the body. Here L/R = the ratio of the length of the body to the base radius and S/S_B = the ratio of the body surface area to the base area. (Section 2.4 explains how the latter was derived.) The pressure drag is estimated as a function of the skin friction

---

[18] This factor is for insulated bodies, and can be found on page 17–4 in Reference [4].

coefficient by the formula

$$C_{DP} = C_f[.00125(L/R)]S/S_B.$$

For supersonic flow, C_f was determined by finding it for a flat plate like in subsonic flow, and then multiplying it by the ratio S/S_B. The pressure drag was broken up into two components, that on the spherically blunted section of the nose and that on the rest of the nose. The former was found as a function of L, R, the diameter of the sphere, and the length of an equivalent nonblunted nose cone by using a series of charts of experimental data for various Mach numbers. The pressure drag of the nose cone without the spherical tip was computed using another series of charts for both conical and parabolic nose cones. These results are dependent on nose cone length, base and tip diameter, and Mach number.

Hypersonic flow is the name for the regime characterized by the Mach wave angle becoming almost equal to that of the body, and is usually defined as beginning at about Mach five. The *Datcom* predicts the corresponding skin friction coefficient by again calculating it for a flat plate and multiplying the result by $1.02 \times S/S_B$. The pressure drag is computed by first dividing the body up into a series of segments. These consist of either a spherical or conical tip and either conical or cylindrical afterbody segments. The coefficient of pressure is computed for each segment using charts obtained from Newtonian theory. These charts are dependent on the geometry of the sections, but not the Mach number.

The pressure and skin friction coefficients were plotted together as a function of

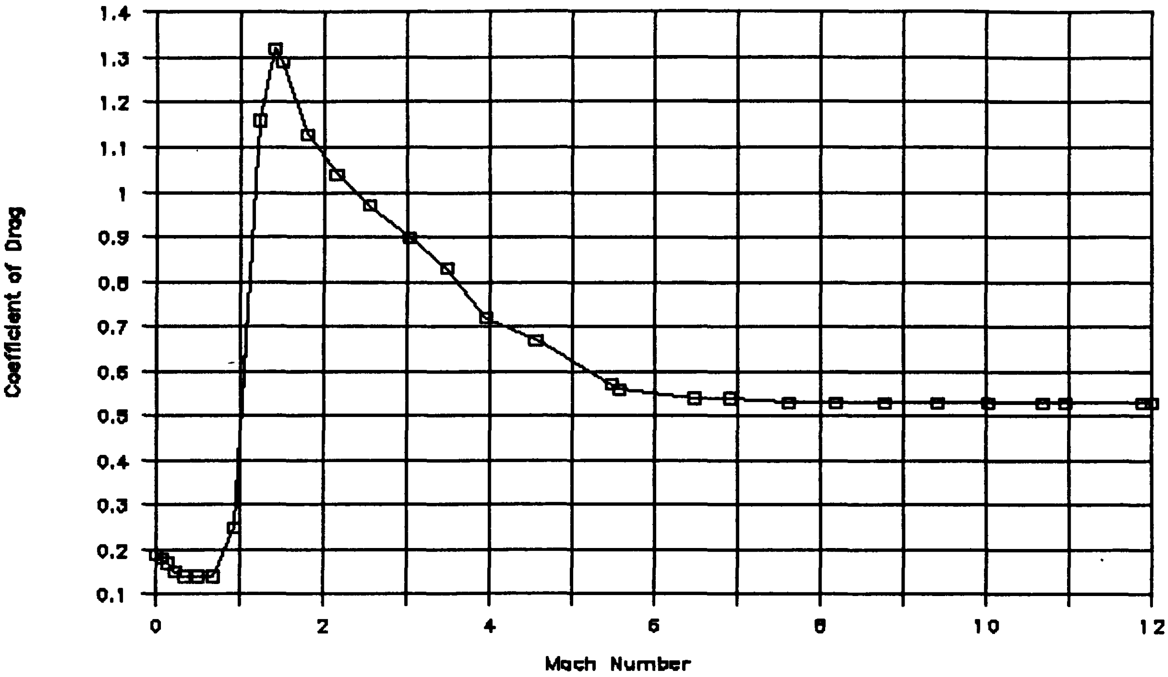

Figure 2.4: C_D **Versus M as Calculated for the Fairing**

Mach number for each regime. Then, using plots of similar data from Reference [4], the results were combined and values of C_D (not including base drag) were read off the plot for a series of Mach numbers. The final plot obtained for the fairing is shown in Figure 2.4. (These results are for a reference area of 594 ft^2.) Following this procedure for each different nose cone, a similar plot can be obtained. Defining $C_{booster}$ = the pressure and skin friction drag of the booster, $C_{fairing}$ = the pressure and skin friction drag of the fairing/core, and C_{DB} = the base drag as defined in Figure 2.3, the total coefficient of drag for the launch vehicle is defined as:

$$C_D = (C_{fairing} + C_{DB}) + 6 \times (\frac{2}{3}C_{booster} + C_{DB}) \tag{2.15}$$

The drag can thus be computed by multiplying the results from this equation times the reference area (594 ft^2) and the dynamic pressure at the corresponding Mach number (see Figure 1.4). When this is done for Mach numbers from zero (launch) to twelve (when the dynamic pressure becomes effectively zero), the total or average drag of the launch vehicle with a particular booster nose cone can be obtained. Comparing this to the baseline average drag and using Equation 2.6, the effect on the payload mass to orbit can be determined.

The calculation procedure just described is valid for bodies which can be divided into conical and cylindrical segments, and with a conical or spherical tip. Though the *Datcom* does provide plots for parabolic profiles too, these are just for a "generic" parabolic type of shape. Thus, in order to compute the coefficient of drag on a minimum drag segment, the equivalent conical section coefficient of drag was computed and then reduced by 10% (see page 38).

2.4 Computing Mass

Computing the mass of the various nose cone geometries can be quite complicated. The structure will most likely consist of an aluminum skin with reinforcement rings. One of the difficulties arises from the fact that the smaller the nose cone angle is, the stronger (at least against axial loads, which will be the dominating force) it is and the less rings are needed. On the other hand, the greater the nose cone angle, the greater the surface area/skin weight will be. In addition, all of the loads acting on the nose cone would need to be modeled and each different shape looked

Angle (degrees)	**Mass (lbm)**
10	3224
15	2580
20	2218
25	2125
30	2274

Table 2.1: **Angle vs. Weight for the Saturn V Fairing (Nose Cone).**

at separately for structural stability. For the purpose of this report, the results of a study done on the Saturn V fairing were adapted to the JRB.

Table 2.1 gives the relationship between cone angle and cone mass assuming an aluminum shroud with a base diameter of 260 in.[19] This is related to the JRB by multiplying it by the ratio of the JRB nose cone surface area to the surface area of a nose cone with the given angle. In order to compute the surface areas of various JRB nose cones, a computer program was written. Given in Appendix B, it allows one to describe the nose cone as either a formula, a set of data points, or a series of geometric shapes. If the latter option is chosen, it allows one to define the tip as either a sphere, cone, or cylinder, and the other sections as either truncated cones or cylinders. With the variables defined in Figure 2.5, the surface area of a spherical segment is calculated by

$$S_{sph} = 2\pi RL,$$

of a cone or truncated cone by

$$S_{cone} = \pi(R_B^2 - R_A^2)/\sin\theta$$

---

[19] This data is from Figure 4 in Reference [1].

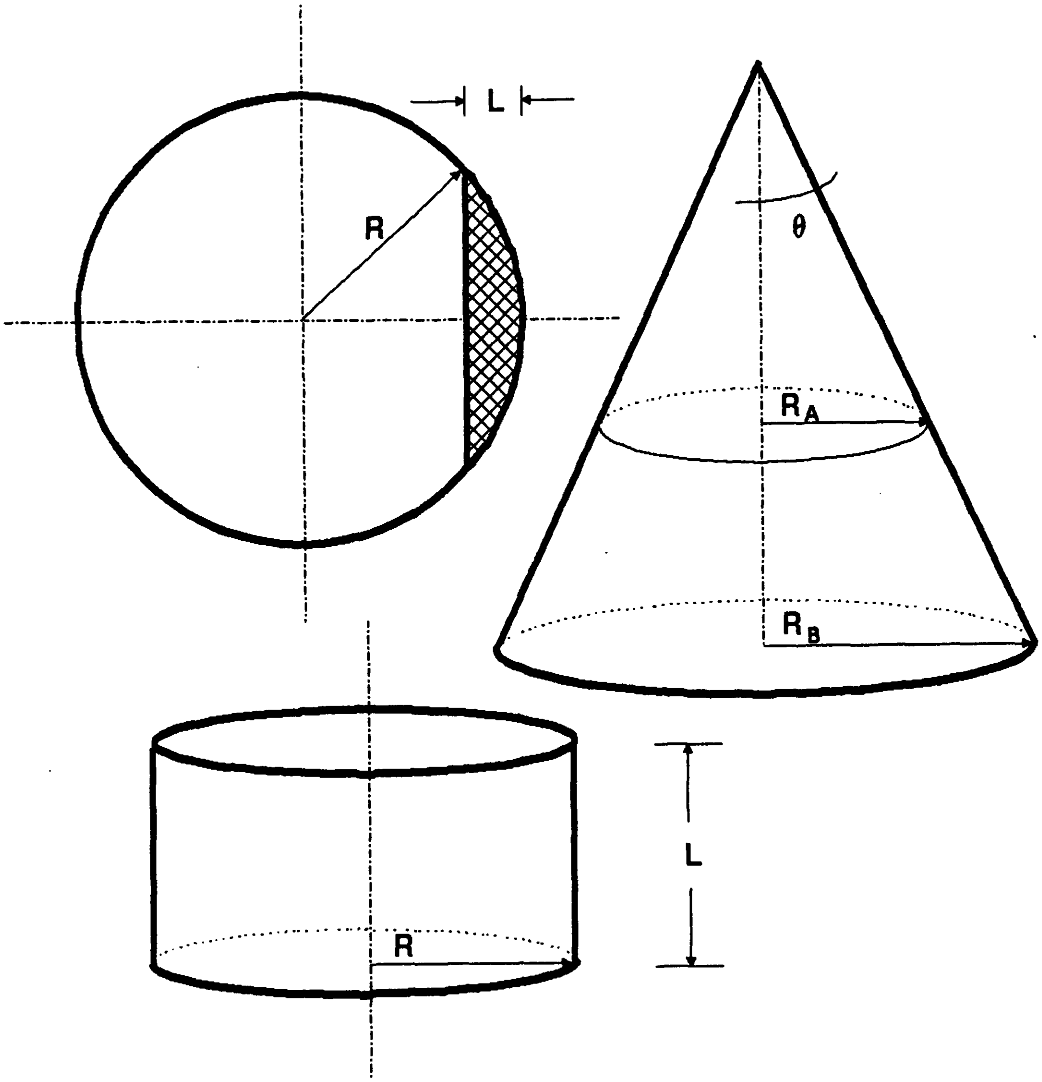

Figure 2.5: **Surface Areas of Various Geometric Shapes**

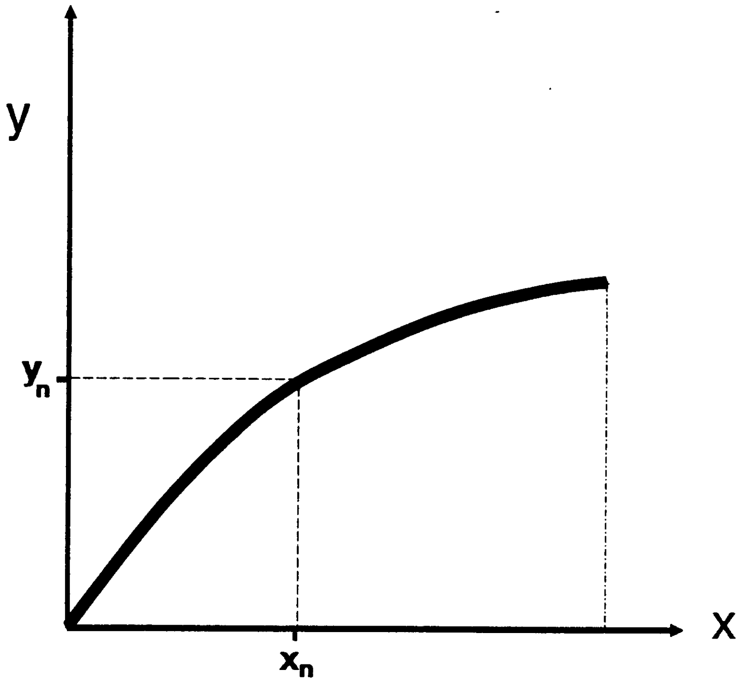

Figure 2.6: **Coordinate System for a Cross-Section of the Nose Cone**

(with $R_A = 0$ for a cone), and of a cylinder by

$$S_{cyl} = 2\pi RL.$$

If an equation is input, it is of the form $y = f(x)$, as defined by Figure 2.6. Given the derivative, it is now solved numerically by integrating the following equation:[20]

$$S = \int_a^b 2\pi y \sqrt{1 + (\frac{dy}{dx})^2}\, dx$$

When a series of data points (x_n, y_n) are entered, they are integrated around the x-axis using

$$S = \sum_{i=1}^{i=n} 2\,\pi\, y_i\, ds$$

---

[20] From Reference [17], page 257.

where ds is the distance between two data points. Thus, given a value of S for the nose cone, the mass can be estimated using

$$M = M_{Sat} S \sin\theta / (\pi r^2) \tag{2.16}$$

where θ = the half angle of the nose cones, M_{Sat} = the mass of the equivalent Saturn V nose cone given in Table 2.1, and $r = (260 \text{ in})/2$.

Chapter 3

Reentry Heating

3.1 Introduction

The JRB is designed to be completely reusable with virtually no refurbishment required. As such, it must be able to withstand a fall from the height of separation with the core to impact with the ocean. It is assumed that a parachute, ballute, or attitude control system will stabilize the body so that it passes through the atmosphere nose-first. Though a deployable decelerator will be used to decelerate it to less than 80 ft/sec at impact, this decelerator cannot be deployed until after peak heating and deceleration loads have occured. This means that the booster, and specifically the nose cone (on which the stagnation-point is located), must be able to withstand the full effects of atmospheric heating. This can only be accomplished with certain geometries of the nose cone.

3.2 The Reentry Scenario

3.2.1 Environment

As the vehicle reenters the atmosphere, it passes through a number of flow regimes as the atmospheric density increases. The first regime is that of free molecular flow. With λ_∞ = mean free path and R = radius of the reentry body, this regime occurs when $\lambda_\infty \gg R$ so that gas phase collisions can be ignored. The near free molecule regime begins at an altitude of about 450 kft[1], and is where molecular collisions begin to have an effect. From just over 400 kft to about 350 kft there is a transitional layer, below which are the continuum regimes. Cox and Crabtree [13] next define the fully merged layer, incipient merged layer, and vorticity interaction regimes, however they can be considered together (as in Martin [18]) as the viscous merged layer. Located from about 350 kft to 250 kft, this layer is characterized by viscous flow and the creation of a shock wave and boundary layer around the body. Below about 250 kft continuum flow is encountered. In this region normal high Reynolds number aerodynamics is valid, and the shock wave and boundary layer can be analyzed as a discontinuity.

In the first two flow regimes heat transfer rates are obtained from kinetic theory, using momentum and energy exchange accomodation coefficients [13, p. 216]. In the near free molecular flow regime the effect of molecules reemitted from the body

---

[1] For a more exact definition of the location of each flow regime, which are dependent on velocity and nose radius, see Chapter 9 in Reference [13].

striking other molecules in the fluid must be taken into account. These effects, however, are minor compared to those that occur in the lower regimes. As stated in [19, p. 12–02], "Almost all the critical heat transfer problems that arise in penetrating a planetary atmosphere occur in the continuum flow regime." Here, if the body is blunt, there is a detached shock wave behind which a layer of dissociated and ionized gas occurs. This gas transfers heat to the vehicle through radiation. There is also a boundary layer formed by fluid viscosity around the surface of the body. Here both conduction and diffusion transfer heat into the body. Heat is also radiated from the vehicle. Each of these heating methods are discussed in the next section.

3.2.2 Heating

Radiative heating is caused by energy emitted as photons. Radiation both transfers heat to the vehicle from the gas behind the shock wave and transfers heat from the vehicle back out to the atmosphere. The former can be approximated at the stagnation-point in Btu/ft^2-sec by using the following equation from Reference [19]:

$$\dot{q}_{rad} \cong r \times 1.33(\frac{\rho_\infty}{\rho_o})^{1.30}(\frac{V_\infty}{10,000})^{12.5} \tag{3.1}$$

where r = nose radius of the reentry body in feet, V_∞ = free-stream velocity in ft/sec, ρ_∞ = free-stream density, and ρ_o = the density behind the normal shock wave at the nose. The heat flux from the body is given by the Stefan-Boltzmann law:

$$\dot{q} = \varepsilon \sigma T^4_{wall},$$

where ε = emissivity of the body, σ = Stefan-Boltzman constant, and T_{wall} = temperature of the body.

Convective heat transfer is caused by the bulk fluid motion in the boundary layer, giving rise to kinetic, rotational, and vibrational energy, much of which becomes heat. Also, heat conduction occurs as atoms and ions diffuse across the boundary layer, due to the large entropy change, and give up their chemical energy [18, p. 94]. In Reference [19] these effects are combined in a formula which is then simplified to yield the following equation for the convective heat transfer at the stagnation point (in English units):

$$\dot{q}_{s_o}\sqrt{r} \cong 21.9\sqrt{\rho_\infty}(\frac{V_\infty}{1000})^3 \tag{3.2}$$

The JRB will reenter at a speed of 13,800 ft/sec at an altitude of 200 kft. According to Allen and Eggers [20, p. 7], the maximum stagnation point heat flux then occurs at an altitude of 117 kft and a velocity of 11,680 ft/sec.[2] Using the *1976 U.S. Standard Atmosphere* [21], at this altitude $\rho_\infty = 1.48 \times 10^{-5}$ slug/ft^3. The stagnation density ratio at this altitude and velocity is found from Figure 2–9 in Reference [18] to be $\rho_\infty/\rho_o = .094$. Using a value of R_o = 6ft,[3] Equation 3.1 gives $\dot{q}_{rad}$ = 2.57 Btu/ft^2-sec and Equation 3.2 gives $\dot{q}_{s_o}$ = 54.9 Btu/ft^2-sec. Since

---

[2] These values come from Equations 3.8 and 3.9, and assume a C_D of .5.

[3] This will be justified later.

$\dot{q}_{rad}/\dot{q}_{s_o} = .047$, the radiation heating can be ignored in favor of the convective heating. This conclusion is further supported by the fact that convective heating is only a function of V_∞^3, whereas radiative heating is a function of $V_\infty^{12.5}$, so as further deceleration occurs the ratio will become much more pronounced. For example, at the point of maximum average heat flux per unit area,[4] $\dot{q}_{rad}/\dot{q}_{s_o} = 9.82 \times 10^{-3}$, and at the point of maximum deceleration and the maximum altitude rate of heat transfer,[5] $\dot{q}_{rad}/\dot{q}_{s_o} = 1.97 \times 10^{-3}$. As shown in References [22] and [19], it is only for high speeds like those of planetary probes that radiative heating needs to be considered.

3.3 Minimum Heating Shapes

Prior to 1951 all rockets and missiles were designed with slender shapes in order to minimize pressure drag [23]. As pointed out by Lees [19], a vehicle returning from orbit has a kinetic energy of motion equivalent to 13,500 Btu's per pound. By the time this vehicle impacts the earth it will have converted almost all of this energy into heat. Since there is no material which can take this much heat, much of it must be used to heat the atmosphere. It was this latter conclusion that H. Allen, working at the NACA Ames Aeronautical Laboratory, came up with in 1951. By making

---

[4] Allen and Eggers [20, p. 6] derive this as occuring at an altitude of $\frac{1}{\lambda}\ln(\frac{3C_D\rho_0 A}{2\lambda M \sin\theta_E})$ and a velocity of $V_E e^{-\frac{1}{3}}$.

[5] Allen and Eggers [20, pp. 4 & 6] state that both these effects occur at an altitude of $\frac{1}{\lambda}\ln(\frac{C_D\rho_0 A}{2\lambda M \sin\theta_E})$ and a velocity of $V_E e^{-\frac{1}{2}}$.

the vehicle blunt, the shock wave stand-off distance increases and there is a greater volume of air behind the shock wave to become heated. These results were formally published in Allen's joint paper with Eggers entitled "A Study of the Motion and Aerodynamic Heating of Ballistic Missiles Entering the Earth's Atmosphere at High Supersonic Speeds" [20].

This paper begins with a trajectory analysis, the results of which are used in the heating equations. These results are also used in Reference [24]. The basic assumptions taken include a constant coefficient of drag, no gravity term,[6] and an exponential relationship between density and altitude. The results of this trajectory analysis are integrated in heating equations to obtain the following equation for total heat input:

$$Q = \frac{1}{4}(\frac{C'_f S}{C_D A}) M V_E^2 (1 - e^{-\frac{C_D \rho_0 A}{\lambda M \sin \theta_E}}) \tag{3.3}$$

Here $\lambda = \frac{1}{22{,}000}\,\mathrm{ft}^{-1}$ and $\rho_0 = .0034\,\mathrm{slugs/ft}^3$. Since for a relatively light vehicle[7]

$$1 - e^{-\frac{C_D \rho_0 A}{\lambda m \sin \theta_E}} \cong 1,$$

the heating is proportional to

$$\frac{C'_f S}{C_D A} \propto \frac{\text{shearforce}}{\text{dragforce}}.$$

Thus Allen and Eggers were the first to show that increasing the pressure drag by

---

[6] The gravity term is commonly neglected in the literature, since with aerodynamic decelerations of 20 to several hundred g's, it has very little effect.

[7] For the JRB, a 10° nose cone ($C_D \approx .1$) gives $e^{-\frac{C_D \rho_0 A}{\lambda M \sin \theta_E}} \cong 1 \times 10^{-6}$, whereas a 30° nose cone ($C_D \approx .5$) gives $e^{-\frac{C_D \rho_0 A}{\lambda M \sin \theta_E}} \cong 1 \times 10^{-30}$.

increasing the tip radius and cone angle will reduce the aerodynamic heating on the vehicle. However, Equation 3.3 cannot be used to obtain a numerical solution because the "equivalent skin friction coefficient" [20, p. 6] is left in the form

$$C_f' = \frac{1}{S}\int_S C_{f_l}(\frac{\rho_l}{\rho})(\frac{V_l}{V})dS. \tag{3.4}$$

Several studies on the exact shape of minimum heat transfer bodies have been done, but Baker and Kramer were the first to compute such a shape for the heating over an entire reentry trajectory environment. Their results are presented in Reference [25]. In this paper they use heat transfer equations they derived in Reference [24] by starting with equations for local heat transfer coefficients for laminar and turbulent flow from Vaglio-Laurin's work (References [26] and [27]).These equations are made non-dimensional, and then, following Allen and Eggers, an equation for dQ/dy is obtained (using the approximation $dy/dt = -V_\infty \sin\theta_E$) where y is the altitude. This equation is integrated over the trajectory using the approximations

$$\rho_\infty = \rho_0 e^{-\lambda y}$$

and

$$V_\infty = V_E e^{-\frac{C_D \rho_0 A}{2\lambda m \sin\theta_E} e^{-\lambda y}} \tag{3.5}$$

from Allen and Eggers. However, in Allen and Egger's analysis they assumed the shock-layer Reynolds number R_{e_o} was constant, and Baker and Kramer used

$$\mu_0 = C_\mu T_0^w \text{ (where } C_\mu \text{ and } w \text{ are constants)}$$

and the two equations just given to relate it to altitude before integrating. Applying calculas of variations to the final series of equations, they obtained minimum heat transfer shapes. The results are given as a function of the fineness ratio (τ). For τ in the region of most nose cones ($\tau \geq .5$), the laminar and turbulent results both give very close to the same shape. It begins with a flat disc with a radius about 80% of the base radius and then angles almost straight back to the base.[8] Though this shape reduces heating by increasing pressure drag, this in turn increases the drag load on ascent, reducing performance.

In designing a nose cone which will also minimize drag, the drag should be reduced to just shy of the point where the heating becomes too great for the material. For the JRB, the goal is minimum refurbishment, thus this heating limit must be before either ablation begins or the structural integrity of the vehicle is compromised. In order to determine if this limit is reached, a method must be found to calculate the heat transfer for a variety of nose cone shapes.

3.4 Calculation of Reentry Heat Transfer

The maximum heating rate which the JRB will experience will take place at the stagnation-point. Assuming the velocity vector falls along the body axis, this is located at the tip of the nose cone. With regard to the shape of this nose cone, as Allen and Eggars pointed out:

---

[8] See figure 3, p. 414 in Reference [25].

> It seems unlikely that a pointed nose will be of practical interest ... since not only is the local heat-transfer rate exceedingly large in this case, but the capacity for heat retention is small. Thus a truly pointed nose would burn away. Body shapes of interest ... would more probably, then, be those with nose shapes having nearly hemispherical tips.[9]

A fairly accurate equation for predicting the stagnation heating rate on a hemispherically tipped nose cone is the Detra, Kemp, and Riddell correlation:

$$\dot{q}_s = \left(\frac{r}{P_s}\right)^{-\frac{1}{2}}(638.8)\left(\frac{V_\infty}{26,000}\right)^{2.15} \tag{3.6}$$

where $\dot{q}_s$ is the stagnation heat flux in Btu/ft^2-sec, r is the nose radius in feet, P_s is the stagnation pressure in atmosphere, and V_∞ is the free-stream velocity in ft/sec. Though this correlation was obtained as far back as 1957, in 1975 L. Perini [28] showed it to still be very accurate. Perini plotted stagnation-point heating rate test data from ten different sources, totalling over 500 data points on various hemispherical noses. They experienced velocities of up to 60 kft/sec and simulated altitudes of 20 kft to 170 kft. He found that Equation 3.6 had a standard deviation of only 17.0% from the data, and for velocities below 25,000 ft/sec the deviation was only 14.1% [28, p. 190].

When designing a non-ablative nose cone, it is obviously necessary that r is made large enough to prevent $\dot{q}_s$ from exceeding the maximum heat flux the material can withstand. If this makes r too large for either drag or water impact reasons, a replaceable ablative tip would be necessary. Because the heat flux decreases as the flow moves down the nose cone, being able to predict where $\dot{q}$ has reached an

---

[9] From Reference [20], pages 6–7.

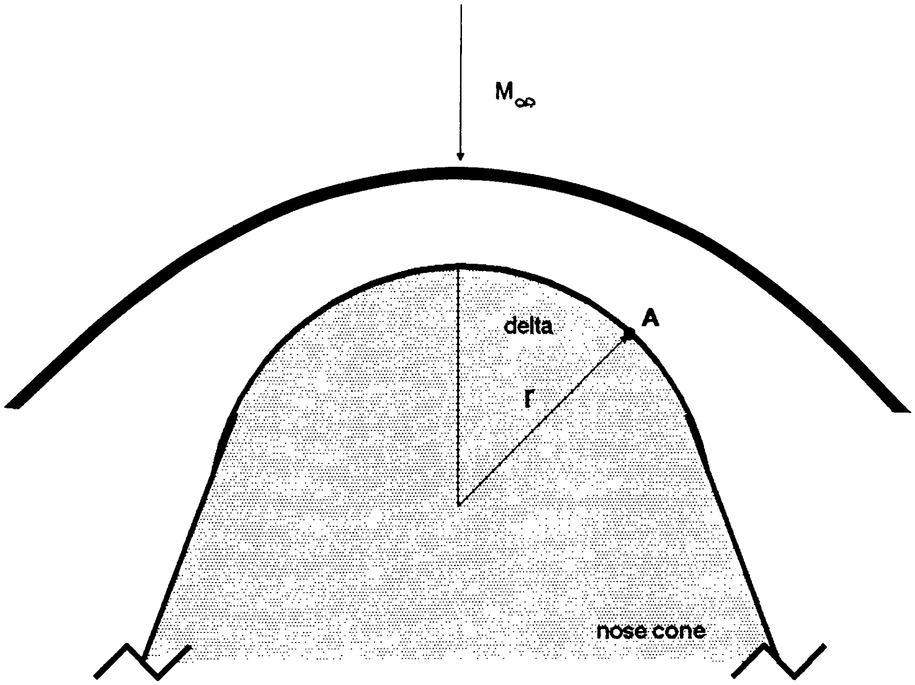

Figure 3.1: **Geometry of the Stagnation Region**

acceptable value for a non-ablative material determines the size of this ablative tip. The corresponding geometry is shown in Figure 3.1, where δ defines the location on the nose cone. Assuming laminar flow in the region close to the stagnation point, the heat flux at point A can be found using an equation attributed to Lees:[10]

$$\dot{q} = \dot{q}_s \frac{2\delta \sin\delta[(1 - \frac{1}{\gamma_\infty M_\infty^2})\cos^2\delta + \frac{1}{\gamma_\infty M_\infty^2}]}{\{(1 - \frac{1}{\gamma_\infty M_\infty^2})[\delta^2 - \frac{\delta}{2}\sin 4\delta + \frac{1}{8}(1 - \cos 4\delta)] + \frac{4}{\gamma_\infty M_\infty^2}[\delta^2 - \delta\sin 2\delta + \frac{1}{2}(1 - \cos 2\delta)]\}^{\frac{1}{2}}} \tag{3.7}$$

where γ_∞ is the free-stream specific heat.

In order to compute a limiting non-ablative or ablative value for r, the point in the trajectory with the maximum heat flux must be found. This was also done

---

[10] From Reference [29], pages A–20 and A–21.

by Allen and Eggers [20]. They modelled the stagnation on the nose cone as if it occured on the surface of a sphere in subsonic flow (which the flow is behind the shock wave). After making several assumptions, including a Prandtl number of unity and incompressible flow, they were able to combine their results with the trajectory equations derived earlier. The maximum heat transfer was found to occur [20, p. 7] at an altitude of

$$y = \frac{1}{\lambda} \ln(\frac{3C_D \rho_0 A}{\lambda M \sin \gamma_E}) \tag{3.8}$$

and a velocity of

$$V = V_E e^{-\frac{1}{6}} \cong .85 V_E \tag{3.9}$$

The maximum heat flux at the blunt tip of the nose cone can thus be computed in the following manner: First, a value for both r and the nose cone half angle θ are chosen. These are used to compute the hypersonic C_D as outlined in Section 2.3.3, and this value of C_D is then inserted into Equation 3.8 to obtain an altitude. Using Reference [21], the free-stream pressure, P_∞, at that altitude is computed. The results from both Equations 3.8 and 3.9 are used to obtain the stagnation pressure ratio, P_s/P_∞, from Figure 2–8 in Reference [18]. This gives P_s, and Equation 3.6 is now solved for $\dot{q}_s$. Finally, using Equation 3.7, the heating in the vicinity of the stagnation region is determined.

Chapter 4

Water Impact

4.1 Introduction

In order to successfully reuse the JRB's, they must be able to survive the impact with the ocean. This impact causes a variety of structural loads in combination with potential water damage to the engines. As stated in References [30,31], these loads are often large enough to have a major impact on the mechanical design. Though the design of the vehicle's recovery system will determine the velocity vector at impact, the shape of the nose cone will have a large effect on how the vehicle reacts and the resultant loads. By approximating the vehicle dynamic response and the structural loads for a variety of impact conditions, an optimal recovery system/nose cone combination can be designed.

The water entry problem is very complicated. Theory can help bound it, but the problem is much too complicated to solve with sufficient accuracy using a mathematical model. As the object impacts the water a cavity of air forms around it. The exact shape of this cavity over time and its properties are dependent on both the properties of the air and water, and the speed, angle, geometry, and mass properties of the object. It is knowledge about this "unknown change in the shape of the boundaries" [32, p. 1] which makes this problem so difficult. Though theory and data from past tests can be used to help bound the problem, a drop test eventually has to be done for each configuration. As stated in Reference [32, p. 3], no accurate scaling laws have been derived for use when a parameter has changed.

This section will now describe the basic events that occur during water impact/entry. Next, past studies, all of which rely heavily on scale model testing, will be discussed and the JRB impact problem will then be compared to these past studies. A theory for predicting impact loads is presented, and finally, model theory will be discussed, followed by a description of the model of the JRB built and its testing.

4.2 The Water-Entry Problem

Madden, Wright, and Kross [30] categorized the motion caused by water impact on the SRB's into three stages. The first is the "initial impact stage," which lasts from the initial impact until a cavity begins to form around the object. The "submergence stage" then lasts from the beginning of this cavity formation until maximum submergence is reached. Lastly, the "rebound stage" covers the time period from maximum submergence to resurfacing and settling in the water. This final stage is also defined to include slapdown, which is the second impact which occurs after resurfacing.[1]

At the start of the initial impact stage, a large acoustic pressure equal to $\rho_w V_o a_w$ (where a_w is the speed of sound in water) acts on the booster, and compressibility effects of the water are important. However, because $V_o / \sin\alpha < C_w$ [33, p. 17] for the JRB (C_w is the shock wave speed in water, which propagates faster than the local speed of sound and α is the entry angle of the booster), no shock wave is produced. The acoustic pressure thus acts for such a short period of time and on such a small area that its effect on the booster's motion and the force it produces can both be ignored. (This conclusion was obtained for the SRB's [34, p. 155], and for missiles with a low value of V_o [35, p. 2].) Madden et al. then went on to describe the process of the SRB nozzle filling with water. Because the JRB enters nose first, the submergence stage will be looked at next.

As the nose cone enters the water, a cavity begins to form around it. A large axial pressure force acts on the vehicle, and can be computed from the deceleration which occurs. The forces acting on the body are approximated in Figure 4.1. First of all, as the vehicle is entering the water, it decelerates with a force Ma at an angle $\beta+\alpha$ from the normal to the water's surface with $\beta =$ the angle between the booster

---

[1] This discussion assumes a highly buoyant, axisymmetric object.

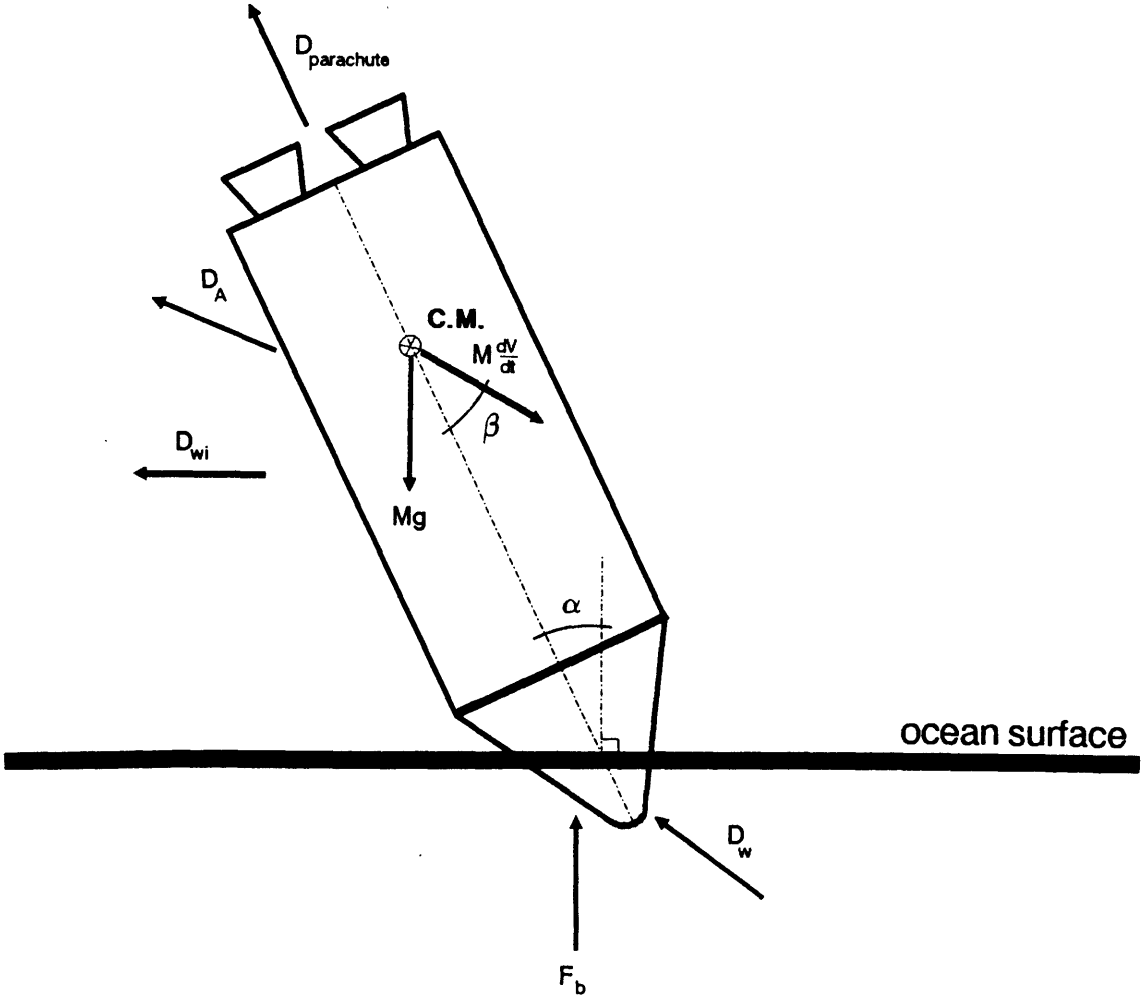

Figure 4.1: **Forces at Water Entry**

axis and the velocity vector. At the same time much of the vehicle's momentum is being transfered to the water. (In the literature the mass of this water is called the "added mass," m.) There will also be a force caused by any wind (F_{wi}) and acting on the center of pressure of the portion of the booster above the water's surface and in the direction of the wind. Gravity will be acting with a force Mg through the center of gravity, which is located in the rear of the booster due to the heavy engine weight. There will be a buoyancy force

$$F_b = V'_A \gamma_A + V'_w \gamma_w \simeq V'_w \gamma_w$$

where $V' =$ volume of air or water displaced and $\gamma = \rho g =$ specific gravity. This force acts through the centroid of the volume of fluid which the nose cone has displaced. Lastly, there is a drag on the booster. Neglecting the remaining air drag, this leaves the water drag equal to

$$D_w = \frac{1}{2} \rho_w V^2 C_x A.$$

where C_x is defined as the axial force coefficient. Computing C_x as the nose cone enters the water would be complicated enough, but, as described before, a cavity forms around the nose cone. Some experimental results can be found in Reference [36] however. This drag operates through the center of pressure of the submerged portion of the booster. Now, as the booster enters the water, not only do Ma, ma, F_{wi}, F_b, and D_w all change, but the point of application of the last three forces also changes, changing both α and β. It is easy to see why this problem has long avoided an accurate theoretical solution. (Section 4.3.2 discusses those theories that have been proposed.)

In order to make this problem easier to deal with, it has usually been divided into several different "separate" phenomenon. As the nose cone enters the water at an angle, the buoyancy force acts like a lifting force, causing a phenomenon known as whip. (Madden et al. were covering the case of vertical entry, so they did not discuss it.) Whip can be defined as "the change in angular velocity about an axis perpendicular to the plane of motion of a missile during the submergence of the nose"[35, p. 1]. As described by Waugh and Stubstad [37, p. 69], whip is caused by two different things. The first is the fact that just the lower part of the nose experiences the initial forces. These include both the pressure forces and something called underpressure. The latter occurs when a section of the cavity which forms around the nose becomes sealed and then expands. This causes the pressure in this section to be reduced below that of the top part of the nose, and has actually caused missiles to dive. The second cause of whip is the moment about the center of gravity created by the underwater drag. Both the pressure forces and the drag moment cause a whip during the submergence stage which greatly increases the slapdown that occurs during the rebound stage. Another effect which usually occurs at either the end of the submergence or the beginning of the rebound stage is cavity collapse. This occurs when the walls of the cavity which has formed collapse inward. Because recovery vehicles are large and buoyant, this occurs against their sides, rather than behind them, and produces a large axial force [31,38].

The water impact problem can thus be thought of as follows: Right after the initial impact a cavity begins to form around the booster and drag and buoyancy forces combine to create large axial loads. These fall off as velocity decreases, yet for entry angles other than zero, whip has started. The booster then reaches its maximum depth and the buoyancy force begins to push it back up out of the water. Around this time the cavity has collapsed, causing large axial loads. Now, as the booster rebounds, gravity pulls the engine end down, and this combines with the whip already present to cause a "slapdown," which adds a further set of radial forces to the structure.

4.3 Past Studies

4.3.1 Introduction

The analysis which has been done on water impact can be divided into several categories. The first includes variations of a study done by Von Kármán on the impact of seaplane floats back in 1929 [39]. His analysis assumed conservation of momentum during impact. The water is accelerated from rest with a momentum equal to the added mass times the missile's speed. It is this acceleration which gives the impact force. Though variations of this method have been the main ones used over the last 60 years, it has been described as "at best a rough approximation"

[32, p. 1]. The impact of manned capsules is another area which generated a lot of analysis. In addition, the SRB's (which reenter nozzle-first) have stimulated several studies, and, finally, a lot of experimental and theoretical work has been done studying missiles and torpedos.

4.3.2 Theory

Von Kármán's paper derives an approximate equation for the pressure at impact of seaplane floats. He approximated the float as a "cylindrical body with a wedge-shaped under surface," and then derived a momentum conservation equation between this float and the water. The mass of the accelerated water, or the "added mass," was approximated using a simple equation from potential flow theory. The effect of buoyancy, which would decrease the momentum, was neglected. The equation he derived was

$$P = \frac{\rho_w V_0^2}{2} \frac{\pi \cot(90 - \theta)}{(1 + \frac{\rho_w g \pi y^2}{2W})^3}$$

with W = weight of the float per unit length, y = submerged radius of the float, and θ = half angle of the float. Assuming that maximum pressure occurs in the middle of the float at impact,

$$P_{max} = \frac{\rho_w V_0^2}{2} \pi \cot(90 - \theta) \tag{4.1}$$

In the decades following Von Kármán's paper, several others have looked at impact and the virtual mass concept with regard to different shapes. Shiffman and Spencer studied cone [40] and sphere impact, and Trilling [41] came up with a solution for non vertical entry.[2] A problem with these earlier studies was the fact that for flat surfaces the equations gave an infinite pressure. (In Equation 4.1, as θ approaches zero, $P_{max} \rightarrow \infty$.) In 1961, Chu and Abramson suggested solving the problem by considering the compressibility of water, yet Moran came out with a paper in 1965 in which he stated that this compressibility was not very important for blunt-nosed objects, and instead the problem could be explained by analyzing the density in the air layer between the vehicle and water.[3] Since that time furthur attempts have been made to take these effects into consideration, yet the conditions at impact are still unknown. In 1972, Kettleborough [43] developed a mathematical model using the Navier-Stokes equations for the incompressible air layer and fluid, and the Marker-and-Cell method for fluid flow, yet his "solution" has several gaps, including a velocity singularity at impact. In his conclusion he points out the still current need to fully understand what happens at impact before it can be modeled with any accuracy.

4.3.3 Manned Capsules — Apollo

The water landing of manned spacecraft, beginning with the Mercury program in the late 1950's, focused a lot of attention on the impact problem. Though each spacecraft was of the same general conical shape (in order to minimize reentry

---

[2] Szebehely's paper [42] provides a good summary of work done through the late 1950's.

[3] Kettleborough [43] summarizes some of the literature through 1972.

heating by "backing" into the atmosphere), several different solutions to the impact problem were used. The Mercury spacecraft extended an airbag below the capsule in order to attenuate impact loads. The Gemini spacecraft did not use such a bag, but rather entered the ocean positioned like a wedge. The Apollo Command Module (CM) was constructed so that it could either enter as a wedge or a large flat body. The Apollo water entry problem will now be discussed in more detail as an example of this kind of problem.

The Apollo Command Module landing conditions consisted of the following: a vertical impact velocity of 30 to 35 ft/sec (for two and three parachutes, respectively), a horizontal velocity of 0 to 51 ft/sec, and a suspension angle for the center of mass of 27.5°. The parachute system caused a swing of ±4 to ±8° (for two and three parachutes), and 8.5 ft waves with a slope of 8.5° were assumed. Depending on the vehicle's velocity vector and pitch angle upon impact, it could either roll counter clockwise or clockwise, usually overturning, or submerge to a depth of up to 18 ft. Orienting the vehicle after impact was accomplished by inflating gas bags in the parachute compartment.

In order to analyze the above scenario, it was assumed that there was no horizontal velocity, no change in attitude, and no deflections in the structure. This allowed a modified Von Kármán analysis[4] to give an approximation of axial loads. In addition, model tests and full-scale tests were run. As stated by Benson, it was

---

[4] This was developed by Langley Research Center and also used for the Mercury program

because the Von Kármán analysis was "limited" that it was "necessary to determine experimentally most of the water impact load information on the Apollo CM" [44, p. 1282].

Model tests were conducted at NASA's Langley Research Center, North American Aviation Company (NAA), and Southwest Research Institute. In addition, NAA conducted a series of tests on a full-scale prototype. Each of the models tested was about 1/4 scale and utilized Froude scaling. (A detailed description of the scaling used and its justification occurs in Section 4.4.3.) Baker and Westine compared scale model tests with the full-scale prototype tests and concluded that modeling was "feasible, providing that Froude scaling was employed, with rate or viscous effects and the compressibility of the water ignored" [45, p. 201]. Later they stated that "the correlations substantiate that Froude modeling is proper for scaling, permitting use of dissimilar materials in the model and prototype" [45, p. 207]. An example of this is pointed out by Abramson [46, p. 218] in that for both model and prototype, damage occured at vertical velocities between 32.0 and 32.4 ft/sec.

4.3.4 Solid Rocket Boosters

The Space Shuttle Solid Rocket Boosters are the first (and only) reusable American launch vehicle boosters, and as such are a primary source of information on water impact. They impact the water at about 85 ft/sec with an attitude of up to 10°. In addition, they enter nozzle first since this configuration provides a higher drag, thus minimizing penetration depth and corresponding hydrostatic forces.

The basic sequence of SRB water entry proceeds as follows: The booster impacts the water and experiences the quick "unimportant" acoustic shock previously mentioned. Next axial forces begin to grow as both the nozzle and the area between the nozzle and the aft skirt begin to fill with water. The water entering the nozzle flows into the motor case chamber causing steady-state values of nozzle pressure. At the same time, the water entering the cavity between the nozzle and aft skirt becomes trapped and stagnates, eventually causing the predominant axial loads to become negative due to the pressure difference between the cavity and the nozzle. This negative load not only helps to reduce the initial impact deceleration, but it also helps reduce the rebounding of the booster. The booster continues to penetrate the water and this negative load reduces to zero. Next the cavity collapses, causing large radial loads. Maximum penetration depth is then reached, following which the booster rebounds and experiences slapdown.

In order to compute axial loads on the SRB's, some extremely simplified analytical techniques were used to provide initial data. After that a series of scale model drop tests were run at the Naval Surface Weapons Center's Hydroballistics Facility. In the mid-seventies models with diameters of 6 in and 12 in [30] and 12.5 in (8.56%) [31,34] were all tested. In addition, another 12 in diameter model was tested in 1983 in order to study loads on a filament-wound case [38]. These models were scaled with Froude scaling like the Apollo models, yet also used pressure scaling. The reason for the latter was to account for the gas compression which occurs in the chamber of the SRB as water is forced through the nozzle upon impact.

Reference [31] compares actual SRB flight data to the 12.5 in diameter model tests. Specifically, the cavity collapse loads are compared, and it was found that the model provided accurate load predictions. The penetration depth reached was greater than that predicted however. This was explained as caused by the fact that the hot ullage gases in the actual SRB chambers were cooled by water spraying through the nozzle, thus reducing the internal case pressure and consequently the buoyancy.

Some of the interesting results that these SRB model tests provided are listed below. For a given impact velocity, the peak axial acceleration is virtually the same whether a rigid or flexible model is used [30, p. 170]. Maximum penetration depth also appears to be independent of flexibility [30, p. 171], and it is reached earlier by higher velocity models, which then resurface earlier [30, p. 172]. The peak cavity collapse pressure is also highly dependent on impact velocity, for reducing the latter by 20% can reduce the collapse pressure by up to 40% [38, p. 66]. Stiffener rings can reduce displacement from these cavity collapse loads by about 15% [38, p. 64]. The pitch acceleration appears to be independent of impact velocity for rigid models, yet flexible models do appear to have a large reduction in pitch acceleration [30, p. 172–173]. Nonvertical entry was also studied, and it was found that increasing the impact angle causes a linear decrease in the penetration depth. In addition, for angles above 10° a pressure pulse moves up the vehicle during slapdown. Finally, the maximum slapdown pressure is seen to be strongly tied to the pitch angle and almost independent of impact velocity [30, p. 174].

4.3.5 Missiles

A final area of research involving water impact is that with missiles and torpedos. They are designed to enter the water and travel beneath it, and thus experience cavity collapse loads when fully submerged, and do not experience either rebound or slapdown. In addition, their entry velcity is usually much higher than that of a reusable booster. Nevertheless, this is another source of literature in a field which lacks a substantial amount.

References [33,47] each provide approximate analytical solutions to impact forces on missiles. Reference [33] computes the dynamic response of the missile to impact shock by neglecting gravity, buoyancy, and drag forces. As was previously explained, this impact shock can be ignored for the booster because of its slow speed. Reference [47] computes the forces and dynamics of a torpedo (with or without a parachute) as it impacts the ocean surface and penetrates below it. However, it is for impact velocities in the 20 to 40 m/sec range and is not as accurate for low Froude numbers.

A study of cone-nosed missiles was conducted at the Naval Surface Weapons Center in the mid 1970's [36]. This study derives a theoretical equation for the axial force coefficient C_x during water impact, where

$$C_x = D_w/(q_w A).$$

Using data from tests on models with nose cones with half angles of $22.5°, 30°$, and $45°$ tested at entry angles measured from the horizontal of $45°, 55°$, and $70°$ and speeds of 5.2 to 64 m/sec, several plots were obtained. They show things like entry angle versus $C_{x_{max}}$ for various nose cones, and entry angle versus penetration (to the location of $C_{x_{max}}$) for various nose cones. Conclusions reached include the fact that the maximum force occured before the nose cone was fully submerged, blunt cones both have much larger values of C_x and larger loading rates than fine cones, and, for a given cone angle, $C_{x_{max}}$ occurs during vertical reentry and the maximum loading rate occurs when the entry angle is smallest. In addition, the loading rate and $C_{x_{max}}$ are dependent on entry angle for large cone angles, and are almost independent of entry angle for small cone angles [36, p. 170].

4.4 Jarvis Recoverable Booster

4.4.1 Introduction

The JRB water impact problem has several similarities to past programs, yet is unique. The booster will impact the ocean at a speed ranging from that of the Apollo CM (30 ft/sec — about the slowest speed a deployable deceleration system could reasonably reduce it to) to that of the SRB's (85 ft/sec). The reason for the upper limit is that is the highest speed it was determined the SRB's could withstand and still be reusable. The JRB would be the first space vehicle to impact the ocean nose cone first, thus an understanding of some of the tests done on missiles is important. The basic vehicle dynamics will be similar to those of the SRB. Though the negative axial loads and corresponding effects caused by the pressure differential in the region of the SRB nozzle are unique to it, both vehicles should experience whip, cavity collapse loads, rebound, and slapdown. The dynamics and load estimating used for both the Apollo and SRB programs, coupled with their comparisons to actual flight data, provide a helpful outline for understanding the JRB water impact.

The JRB is a very buoyant structure. Though it is just two-thirds the length of the SRB, it has a diameter twice as large and weighs just one third as much. In addition, the JRB is a liquid booster, and has tanks which must maintain their integrity. Thus no water can penetrate the booster like with the SRB's. The primary forces which will act on the JRB structure are axial deceleration loads and radial loads from cavity collapse and slapdown. The axial loads reach a peak shortly (.01 sec for Apollo [44, p.1284]) after impact and then begin to taper off. These loads are obviously highly dependent on impact velocity, and may have a linear relationship above 15 ft/sec [30, Figure 4a]. Cavity collapse loads, as was mentioned previously, are also highly dependent on impact velocity. In addition, the point of application of these loads is a function of penetration depth, which in turn is related to both impact velocity and nose cone shape. Slapdown loads were reported in [30] to be independent of impact velocity, yet this was for vertical entry. Nonvertical entry causes whip, which is a function of impact velocity, nose cone shape, and entry angle, and has a direct effect on the slapdown loads.

The best way to determine the vehicle dynamics and loads on the JRB during impact would be to do a theoretical analysis based on an advanced version of Von Kármán's analysis and then follow this up with a model test. The model should be scaled both geometrically and by mass, and also using materials which allow the structure to have a stress-strain curve modeled on the original. Both of the above requirements are however quite expensive, as the computer code would have to be purchased for the advanced Von Kármán analysis, and a model can cost $50,000–$100,000. Instead a simpler adapted version of Von Kármán's analysis was used to obtain rough axial load numbers. A model was then constructed, scaling by geometry and mass, and a series of drop tests were performed with a variety of nose cones. The results were then used to determine how different nose cone shapes affected the overall vehicle dynamics. Specific items looked at included penetration depth, cavity formation, rebound, and whip and slapdown.

4.4.2 Theory

As mentioned in Section 4.3.1, variations of the Von Kármán analysis have been used to compute impact pressures. Shiffman and Spencer's analysis of cone impact

[40] assumes a vertical entry and neglects gravity and bouyancy forces. Defining V = downward velocity of the cone, V_0 = velocity at water impact, m = virtual mass of the displaced water, and M = weight of the vehicle, the upward force on the cone is defined as

$$F = \frac{d}{dt}(mV) = -\frac{d}{dt}(MV).$$

Integrating this equation, rearranging terms, and differentiating with respect to time eventually leads to

$$F = \frac{dm/dX}{[1+(m/M)]^3}V_0^2$$

where X = penetration depth and $dX = V\,dt$. An equation for the virtual mass is next derived. By approximating the flow around the cone as an ellipsoid with radius r, this virtual mass is approximated as

$$m = k\rho_w r^3.$$

The radius is equal to $X\tan\theta$ and k is found from classical flow theory about an ellipsoid. This k is then "adjusted" both to account for an earlier approximation made in the flow theory and to include the effect of water rising around the cone and increasing its effective penetration depth. The final equation is thus:

$$F = \frac{3m}{X[1+(m/M)]^3}V_0^2 \tag{4.2}$$

with the virtual mass defined as:

$$m = k\rho_w X^3 \tan^3\theta \tag{4.3}$$

θ	k
0	0
5	.42
10	.62
15	.77
20	.90
25	1.00
30	1.10
35	1.19
40	1.29
45	1.38
50	1.50
55	1.62
60	1.73
65	1.84
70	1.97
75	2.09
80	2.27
85	2.47
90	2.70

Table 4.1: **The Value of k for Various Nose Cone Half Angles**

The coefficient k is given for various cone angles in Table 4.1.[5] The maximum impact force occurs when the penetration depth is:

$$X_{max} = (\frac{2M}{7k\rho_w})^{\frac{1}{3}} \cot\theta \tag{4.4}$$

At the end of their paper, Shiffman and Spencer compare their theory with experimental results. Values for "k" were backsolved from experimental data obtained by S. Watanabe and found to closely approximate the theoretically derived values. The flow theory does have the weakness that often during the calculations for k the velocity was approximated as constant, and thus "strictly speaking ...should be

---

[5] **This data is from Graph 1 on page 403 of Reference [40].**

Nose Cone	$C_{x_{max}}$	
Half Angle	**Experimental**	**Computed**
22.5°	.31	.34
30.0°	.47	.57
45.0°	1.17	1.24

Table 4.2: **Comparison of Values of** $C_{x_{max}}$

used only when M is large compared to the amound of water displaced".[6] Despite this, the authors go on to state that the approximation is good until the maximum impact force has been reached.

In order to further verify these equations for the JRB's, they were used to calculate a maximum axial force coefficient $C_{x_{max}}$, where

$$C_{x_{max}} = \frac{X_{max}}{\frac{1}{2}\rho_w V^2 A_w}.$$

Here A_w is the cross-sectional surface area of the nose cone at the surface of the water when it is at a depth of X_{max}. These results can then be compared to those of Baldwin [36]. He obtained measurements of $C_{x_{max}}$ using accelerometers in models with nose cone half angles of $22.5^o, 30.0^o$, and 45.0^o. Though his models only weighed around 4 lbs and had diameters of 3 in, the nondimensional parameters $C_{x_{max}}$ would ideally be the same as those of the JRB's, and dependent only on nose cone angle. The results from Baldwin's research are compared to those calculated for the JRB's using Shiffman and Spencer's method in Table 4.2. It can be seen that the correlation is quite good.

---

[6] From Reference [40], page 402.

Finally, it should be pointed out that Shiffman and Spencer's method is just for vertical entry, and adapting it to an oblique entry would be too difficult. (Trilling [41] was able to use a slightly different method to determine the impact force for the nonvertical entry problem.) However, as Baldwin's data shows, the peak impact force occurs during a vertical entry. Thus, the vertical entry will be used to determine the maximum axial load the nose cone must withstand on impact.

4.4.3 Model

Dimensional Analysis

When constructing a model who's reactions approximate those of the full-scale version, the field of dimensional analysis is used. The latter discipline is based on Buckingham's "pi" theorem, which states that "a complete equation"[7] can be reduced to a functional relationship between a complete set of independent dimensionless products" [48, p. 68]. Thus, the first step is to set up an equation which includes all of the important variables, and then arrange these variables in a series of dimensionless products.

Using information from Section 4.2, the water entry problem is dependent on F, F_{wi}, Mg, F_b, and D_w. However, F_{wi} can be considered negligable, and $M = \mathcal{F}(F, V), F_b = \mathcal{F}(\rho, g, L, V)$, and $D_w = \mathcal{F}(\rho_w, V, L, C_x)$ with $C_x = \mathcal{F}(L)$. Thus the

---

[7] A complete, or dimensionally homogeneous, equation is one in which every quantity is defined by units in the same self-consistent system.

problem can be represented as $\mathcal{F}(V, L, F, \rho, \mu, g) = 0$. Following the method given in Reference [49], by using the Buckingham Pi Theorem and expressing each of these variables in the same system of units one can obtain a complete set of dimensionless products. Using M for mass, L for length, and T for time, V has units of LT^{-1}, L has units of L, F has units of MLT^{-2}, etc. Expressing this in matrix form gives:

$$\begin{array}{c|cccccc} & V & L & F & \rho & \mu & g \\ \hline M & 0 & 0 & 1 & 1 & 1 & 0 \\ L & 1 & 1 & 1 & -3 & -1 & 1 \\ T & -1 & 0 & -2 & 0 & -1 & -2 \end{array}$$

This is called the dimensional matrix. Subtracting its rank from the total number of variables will give the number of dimensionless products.[8] Because there are 6 variables, and the rank of the above matrix is computed to be 3, there are 3 dimensionless products in the complete set. The next step is to solve for those products.

First of all, in order to have the greatest ability to match these dimensionless products between the model and the prototype, Buckingham pointed out that the variables which can be easily varied should ideally exist in only one dimensionless product. This allows one to match dimensionless products between the model and prototype by varying a different variable in each one. This can be done by first rearranging the rows of the dimensional matrix so that the first variable is

---

[8] For a proof of this theorem, see pages 52-53 in [49].

the dependent variable, and the following variables become progressively harder to regulate [49, p. 39]. Doing this with the given matrix gives:

$$\begin{array}{c|cccccc} & F & V & L & \mu & \rho & g \\ \hline M & 1 & 0 & 0 & 1 & 1 & 0 \\ L & 1 & 1 & 1 & -1 & -3 & 1 \\ T & -2 & -1 & 0 & -1 & 0 & -2 \end{array}$$

Now, the dimensionless products will be of the form

$$\pi = F^{k1} V^{k2} L^{k3} \mu^{k4} \rho^{k5} g^{k6},$$

and the values of these unknowns are determined by the equation

$$[DM_{m,n}][k_n] = [0_m]$$

where $[DM_{m,n}]$ is the dimensional matrix given above.[9] Performing row operations on $[DM_{m,n}]$, one obtains:

$$\begin{bmatrix} 1 & 0 & 0 & 1 & 1 & 0 \\ 0 & 1 & 0 & -1 & -2 & 2 \\ 0 & 0 & 1 & -1 & -2 & -1 \end{bmatrix} \begin{bmatrix} k_1 \\ k_2 \\ k_3 \\ k_4 \\ k_5 \\ k_6 \end{bmatrix} = \begin{bmatrix} 0 \\ 0 \\ 0 \end{bmatrix}$$

---

[9] This is proven on pages 32-33 of [49]

Since this is an undetermined set of equations, by setting the values of k_4, k_5, and k_6 to $(1,0,0), (0,1,0)$, and $(0,0,1)$, and solving for k_1, k_2, and k_3 in each case, the following "solution" is obtained:

	F	V	L	μ	ρ	g
π'_1	-1	1	1	1	0	0
π'_2	-1	2	2	0	1	0
π'_3	0	-2	1	0	0	1

Thus a complete set of dimensionless products is

$$\pi'_1 = F^{-1}V^1L^1\mu^1 = \frac{VL\mu}{F}$$

$$\pi'_2 = F^{-1}V^2L^2\rho^1 = \frac{V^2L^2\rho}{F}$$

$$\pi'_3 = V^{-2}L^1g^1 = \frac{LG}{V^2}$$

Inverting the latter two still maintains their nondimensionality, and makes each product more easily recognizable:

$$\pi_2 = \frac{1}{\pi'_2} = \frac{F}{\rho V^2 L^2} \equiv \text{the pressure coefficient}$$

$$\pi_3 = \frac{1}{\pi'_3} = \frac{V^2}{Lg} \equiv \text{the Froude number}$$

If the first product is also inverted, and then multiplied by π'_2, its nondimensionality is maintained:

$$\pi_1 = \frac{F}{VL\mu} \times \frac{V^2L^2\rho}{f} = \frac{VL\rho}{\mu} \equiv \text{the Reynolds number}$$

The problem can now be expressed as an equation of the form

$$\mathcal{F}(\frac{VL\rho}{\mu}, \frac{F}{\rho V^2 L^2}, \frac{V^2}{Lg}) = 0 \tag{4.5}$$

If a model test can be run where all three products are the same as for the prototype, it will react the same, within the limits of the original equation. However, equating all three products is not possible, and a closer look needs to be taken at the problem to determine which can be safely disregarded. If the Reynolds number is reasonably large, the viscosity effect can be ignored because turbulent agitation is proportional to the Reynolds number, and "the shearing stresses due to viscosity are small compared to the shearing stresses due to momentum transport by turbulence" [49, p. 73]. Because for the Froude number the length is inversely proportional to the square of the velocity, and for the Reynolds number the length and velocity are directly proportional to each other, scaling can only be done by one of the two [10] and the Reynolds number is eliminated. (This is further justified in the next paragraph.) This leaves the Froude number and the pressure coefficient, however the booster is sealed so the latter can also be disregarded.

The Froude number is thus the only parameter which needs to be considered for scaling. This conclusion was also reached by others. For the Apollo CM, Reference [45, p. 201] stated that "a complete similtude (sic) analysis indicated that modeling was feasible, providing that Froude scaling was employed, with rate or vis-

---

[10] Reference [37] states that although there is currently no known liquid for scaling both parameters, an aqueous polymer solution might work.

cous effects and the compressibility of the water ignored." This was later explained in that "the duration of significant changes in the pressure due to compressibility is of the order of 10^{-5} sec, compared to a positive impulse duration of 10^{-2} sec." In addition, "fluid viscosity differences affect the Reynolds number in the 8th significant figure" [45, p. 202]. Reference [37, p. 2] explains that Froude number scaling can be used because "Reynolds forces become essentially constant once turbulent flow has been established." With regard to the SRB's, Reference [34, p. 155] states that in order to simulate full scale SRB dynamics with models, it was necessary to to use "Froude scaling for momentum conservation and pressure scaling for buoyancy simulation." The reason pressure scaling was necessary was because of the importance of the air inside both the nozzle and the skirt when the SRB first hits the water. (This necessitated a closed room for the drop test where the atmospheric pressure could be lowered.) Because the JRB is sealed on impact, this extra modeling is not necessary.[11] Another point should be mentioned before the Froude number is excepted as the "solution." That is the effect of influences called scale effects, which are caused by forces which can affect the model, but have almost no effect on the prototype. In this case the one that should be mentioned is surface tension. Present in the Weber Number,

$$W = (\rho_w V^2 L)/\sigma$$

where σ = surface tension, it can be neglected if the waves are a significantly larger

---

[11] Pressure scaling, or cavitation-number scaling, is necessary for highly accurate results, and is discussed in Section 6.3.

than 1 in in length [49, p. 64].

Model Construction

The preceding analysis showed that in order to come up with a model which closely approximates the response of the prototype in drop tests, it must be scaled using the Froude number. This number can be thought of as the ratio between hydrodynamic forces (frictional drag) and static forces (gravity and weight), as shown in Equation 4.6.[12]

$$\frac{\text{dynamic forces}}{\text{static forces}} = \frac{\text{dynamic pressures}}{\text{buoyant pressures}} = \frac{L^2 \rho V^2}{\gamma L^3} = \frac{V^2}{gL} = Fr^2 \tag{4.6}$$

Thus, the larger the Froude number, the less the effect of gravitational forces as compared to hydrodynamic forces, and the larger waves become [48, p. 91]. As stated by Hoerner [4, p. 11–2], "At one and the same Froude number, the wave pattern produced by a model or full-scale ship has the same shape and the same dimensions in relation to those of the hull."

Equating the Froude numbers for the model and full-sized versions (using a subscript m for model and f for full-size), one obtains

$$\frac{V_m}{\sqrt{gL_m}} = \frac{V_f}{\sqrt{gL_f}} \longrightarrow \frac{V_m}{V_f} = \sqrt{\frac{L_m}{L_f}}$$

Using scale factors, K, which are simply the ratio of model to full-scale values for the various parameters,

$$K_V = K_L^{\frac{1}{2}} \tag{4.7}$$

---

[12] This equation comes from Hoerner [4], page 11–2.

Since mass $M = L^3\rho$, $K_L = K_M^{\frac{1}{3}}$, and

$$K_M = K_L^3 \tag{4.8}$$

Assuming values of $M_{f-structural} = 45,000$ lb and $L_f = D_f = 27.5$ ft, an appropriate model size and material were computed. Scaling geometrically, with a model radius r and a cylindrical length of $l = 4.64r$, the corresponding surface area is

$$S_{cyl} = 2\pi rl = 9.28\pi r^2.$$

With a base area of

$$S_B = \pi r^2$$

and a nose cone area of

$$S_{nose} = (\pi r^2)/(\sin\theta)$$

with $\theta = 30.5°$, the total area is

$$S = \pi r^2(12.25).$$

With ρ_{mat} = density of the construction material,

$$S\rho_{mat} = M_{m-structural}.$$

Using Equation 4.8,

$$M_{m-structural} = M_{f-structural}K_L^3 = M_{f-structural}r^3(13.75\,\text{ft})^{-3},$$

and

$$S\rho_{mat} = M_{f-structural}r^3(13.75\,\text{ft})^{-3}.$$

Rearranging terms,

$$r = \frac{(31,818)\pi\rho_{mat}}{M_{f-structural}} \tag{4.9}$$

Now, the radius of the model necessary for various thicknesses of materials can be computed. Plexiglas is available in as small as $\frac{1}{16}$ inch sheets, weighing .35 lb/ft^2. Using Equation 4.9, this corresponds to a model of radius 9.33 in, which is much to large to build a relatively inflexible structure with walls $\frac{1}{16}$ inch thick. The lightest metal feasible is aluminum, which comes in sheets as thin as .025 in, yet it also has a density of .35 lb/ft^2 and would thus bend much to easily. Finally, corrugated cardboard was looked at because of its high strength to weight ratio. Weighing a sheet of corrugated cardboard, a density of .132 lb/ft^2 was computed. This gives a value of $r = 3.52$ in, which is acceptable for the material. The model was thus constructed out of corrugated cardboard, and a radius of 3.81 in was used in order to account for the additional weight of simulated engine modules and a plastic waterproof coating for the vehicle. The model's central cylinder height was thus 17.68 in high, and engine modules 1.43 in high were added to the base. The entire model was coated with Ultracote, a heat-shrink plastic coating used on model remote control airplanes. The total structural weight came to .55 lb. With a total required weight of $M_f = 60,000$ lb, $M_m = .74$ lb from Equation 4.8. The extra weight was added in the form of fishing weights placed in the engine modules in order to properly orient the center of mass.

Quantity	Corresponding Scale Factor Relationship
Length	$K_L = K_L$
Velocity	$K_V = K_L^{\frac{1}{2}}$
Mass	$K_M = K_L^3$
Mass Moment of Inertia	$K_I = K_L^2 K_M = K_L^5$
Density	$K_D = K_M / K_L^3 = 1.0$
Pressure	$K_P = K_M / (K_t^2 K_L) = K_L$
Angle	1.0
Time	$K_t = K_L / K_V = K_L^{\frac{1}{2}}$
Linear Acceleration	$K_{LA} = K_L / K_t^2 = 1.0$
Angular Acceleration	$K_{AA} = 1.0 / K_t^2 = K_L^{-1}$

Table 4.3: **Booster and Model Relationships**

Model Testing

In order to properly evaluate the results of testing this model, a table of scale factors like those in Equations 4.8 and 4.7 must be derived and used. These are presented in Table 4.3. Using these relationships the behavior of the model can be related to that of the actual booster.

The model was tested in a swimming pool. By dropping it from various heights above the water, different impact velocities were simulated. For example, to simulate a booster impact of 40 ft/sec, the model has to be going

$$V_m = V_f K_L^{\frac{1}{2}} = (40\ \text{ft/sec})(7.62\ \text{in}/330\ \text{in})^{\frac{1}{2}} = 6.08\ \text{ft/sec}$$

at impact. This is accomplished by dropping it from a height of

$$h = V_m^2/(2g) = 6.88\ \text{in.}$$

Results for various full-scale velocities are shown in Figure 4.2. The model was

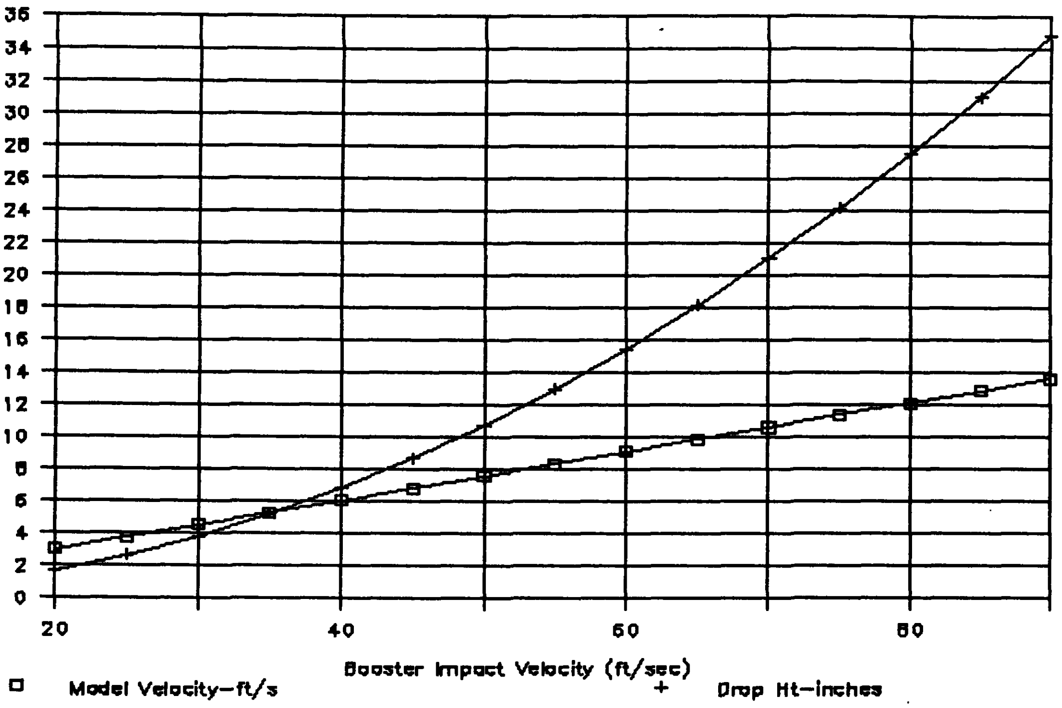

Figure 4.2: **Model Drop Height and Velocity for Various Booster Velocities**

suspended the proper distance above the water by a thread attached to the center of the aft end of the booster. A videocamera was aimed at the model, and the thread was cut. This was done for a range of velocities and several different nose cones. A background grid and a series of hash marks on each nose cone and the booster allowed measurements to later be taken off of the videotape. The experimental set-up is shown in Figure 4.3.

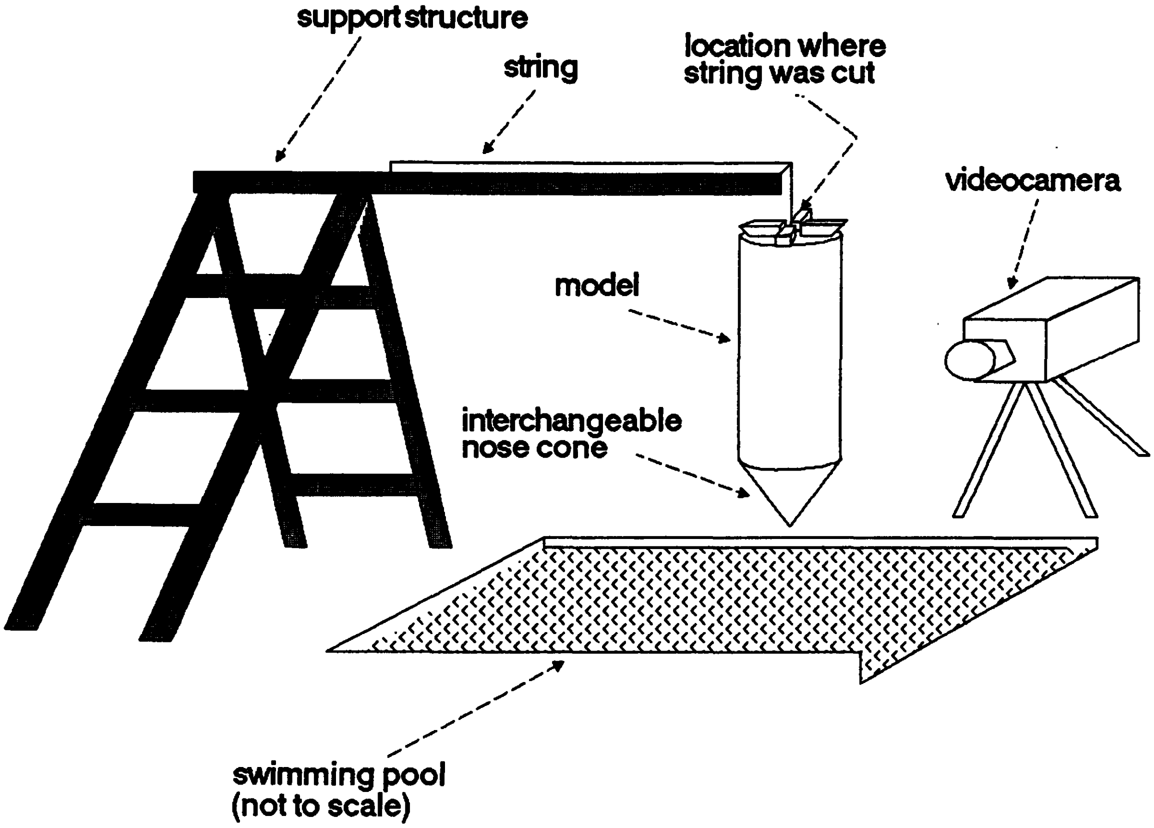

Figure 4.3: **Experimental Set-Up**

Chapter 5

Results

5.1 Heating Calculations

In determining a nose cone shape, the reentry heating results provide boundary conditions if restrictions like no or minimal ablation are imposed. In determining these boundary shapes there are several different parameters one can manipulate. In this study, the nose cone was considered to consist of a hemispherical nose tip[1] and a conical afterbody. As such, both the nose radius and the cone angle can be changed in order to vary the heating on the nose cone. Increasing either one will increase the drag, and thus decrease the (convective) heating. In order to determine the impact of each, the heating limitations of the nose cone thermal protection system must first be determined.

---

[1] This "tip" becomes quite large under certain constraints.

In recent years there have been several advances in the construction of ceramic thermal protection materials. Specifically, flexible ceramic blankets have been developed which offer the advantages of light weight, simple installation, and very good thermal shock resistance [50]. Though the initial costs of the blankets are high, they save money by taking less time to mount on the nose cone, by not requiring many custom made pieces (like the Space Shuttle tiles), and by their relative thermal protection per pound. The Space Shuttle Orbiter currently uses these blankets on several parts of its upper surface. Experiments were performed on several configurations of these blankets by using the reentry-simulating arcjet at the NASA Ames Research Center [50]. The configuration that withstood the greatest heat flux consisted of a Nicalon[2] facesheet over half an inch of Nextel[3] AB312 felt. The backsheet and thread used to hold the cloths to the felt were also made of Nextel AB312. Weighing just 2.004×10^{-3} lbm/in^2, this cloth survived a heat flux of over 28 Btu/ft^2-sec with just a slight oxidation. Allowing a cooling gas to pass through it increased the survived heat flux to over 34 Btu/ft^2-sec. For the purpose of this report it will be assumed that this fabric will be used on the nose cone, and that there is a limiting stagnation heat flux of 30 Btu/ft^2-sec after which ablation begins.

The method outlined in Section 3.4 was used to compute the maximum stagnation region heat flux for various nose cone geometries. Values of the hemispherical

---

[2] Nicalon is a registered trademark of Nippon Carbon Co., Ltd., and consists of silicon carbide fibers.

[3] A registered trademark of DuPont Corporation, Nextel is an aluminoborosilicate.

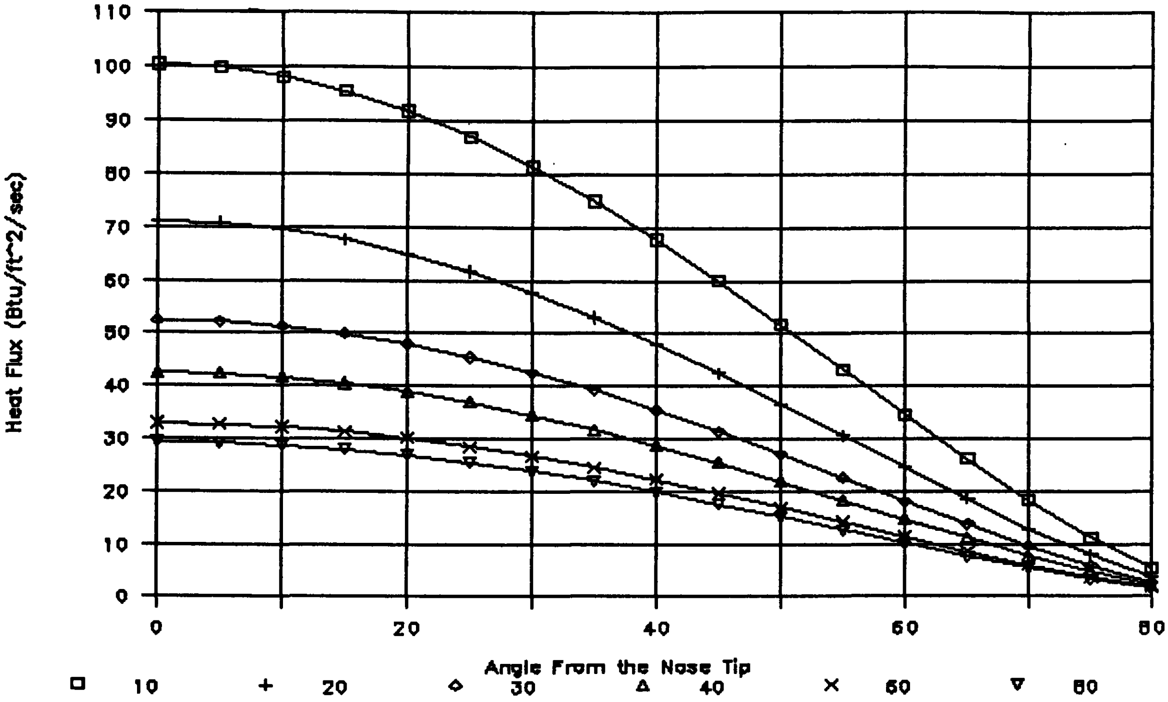

Figure 5.1: **Maximum Stagnation Region Heat Fluxes with r=4 ft.**

nose tip radius r were chosen and a range of cone angles calculated for each one. The size of the conical afterbody was determined by its half angle and the condition that it "attach" to the hemisphere at lines tangent to the latter. The results for hemispherical radii of 4, 6, 8, 10, and 12 feet are presented in Figures 5.1, 5.2, 5.3, 5.4, and 5.5, respectively. Similar results were also obtained for hemispherical radii of 3, 5, 7, 9, and 11 feet, and combined with the previous results to produce Figure 5.6. This Figure shows the minimum cone angle necessary to keep the value of $\dot{q}_s$ less than 30 Btu/ft^2-sec for a range of hemispherical radii. Figure 5.7 shows the geometries of several of these "minimum cone angle" configurations. Figures 5.6 and 5.7 show that in order to prevent ablation, either a very large hemispherical tip or else a very large cone angle is required. For example, using the nominal cone

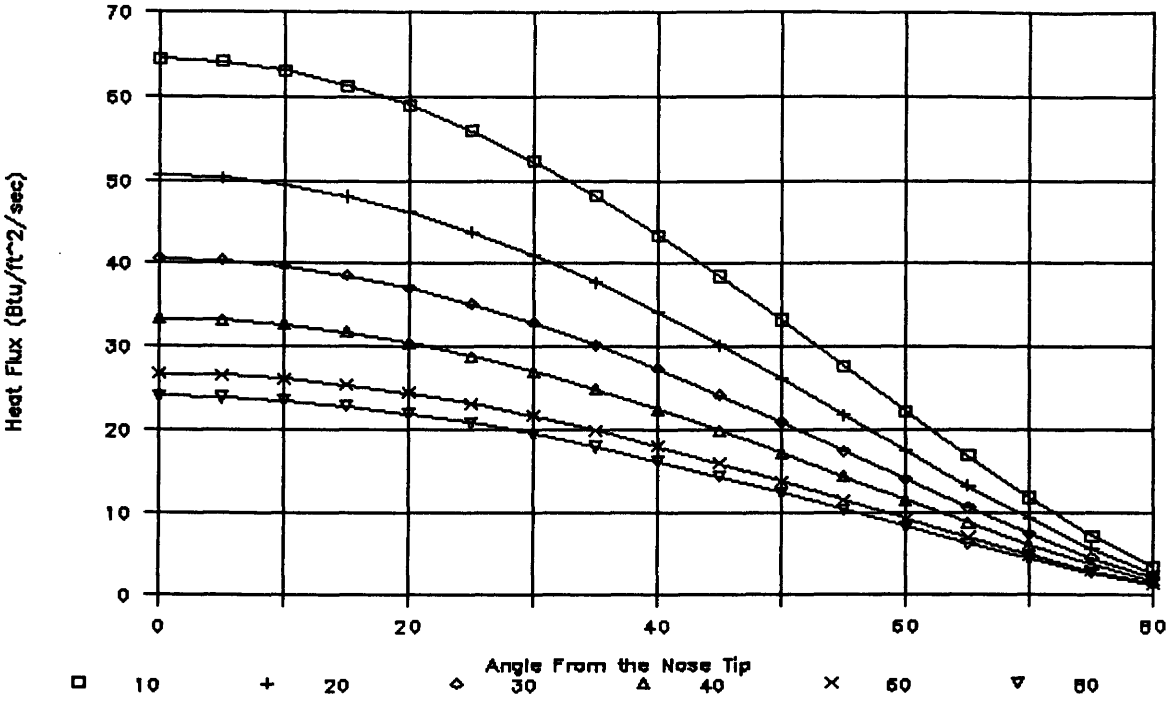

Figure 5.2: **Maximum Stagnation Region Heat Fluxes with r=6 ft.**

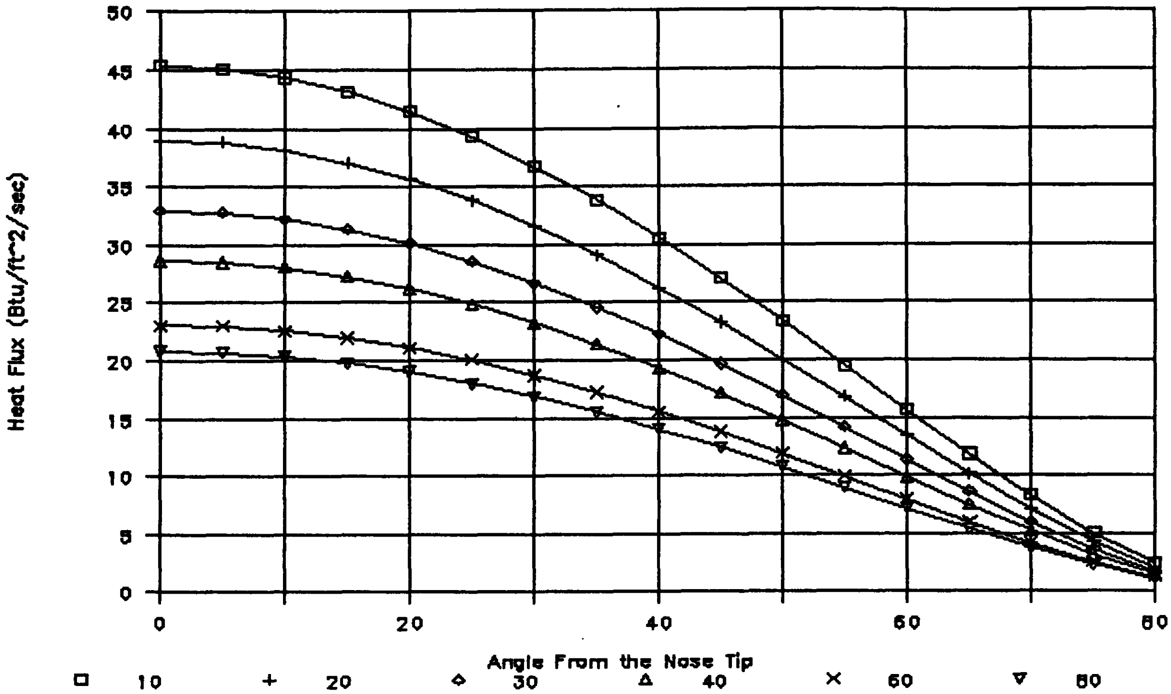

Figure 5.3: **Maximum Stagnation Region Heat Fluxes with r=8 ft.**

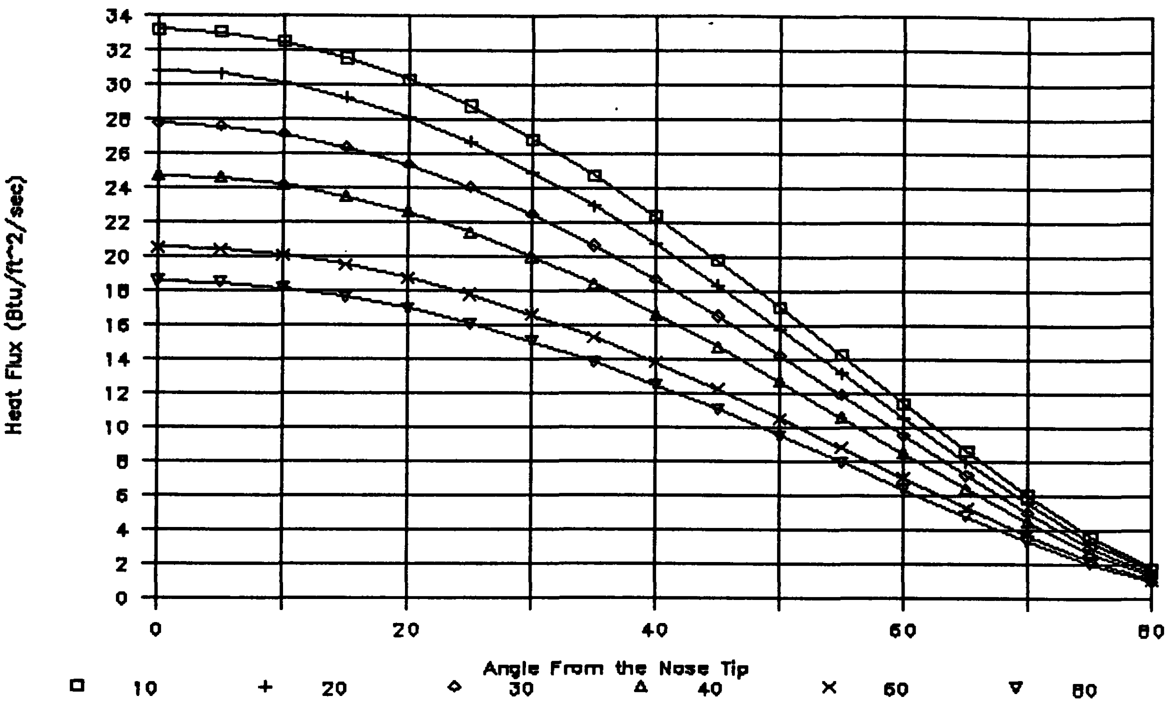

Figure 5.4: **Maximum Stagnation Region Heat Fluxes with r=10 ft.**

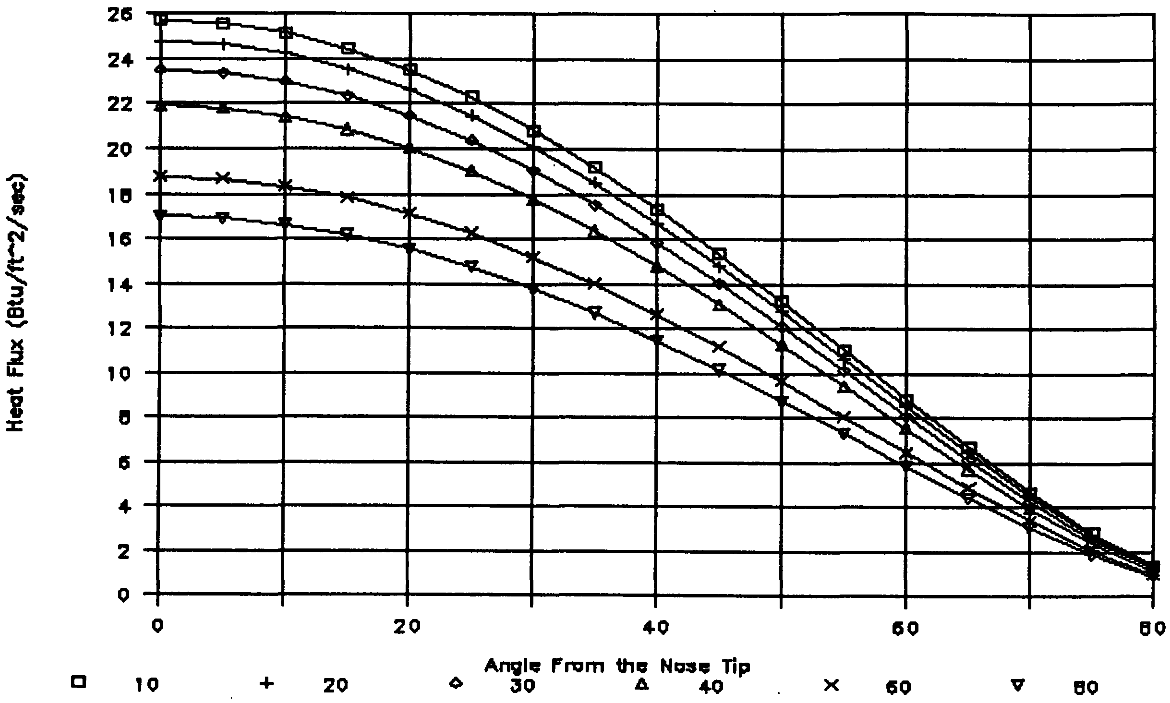

Figure 5.5: **Maximum Stagnation Region Heat Fluxes with r=12 ft.**

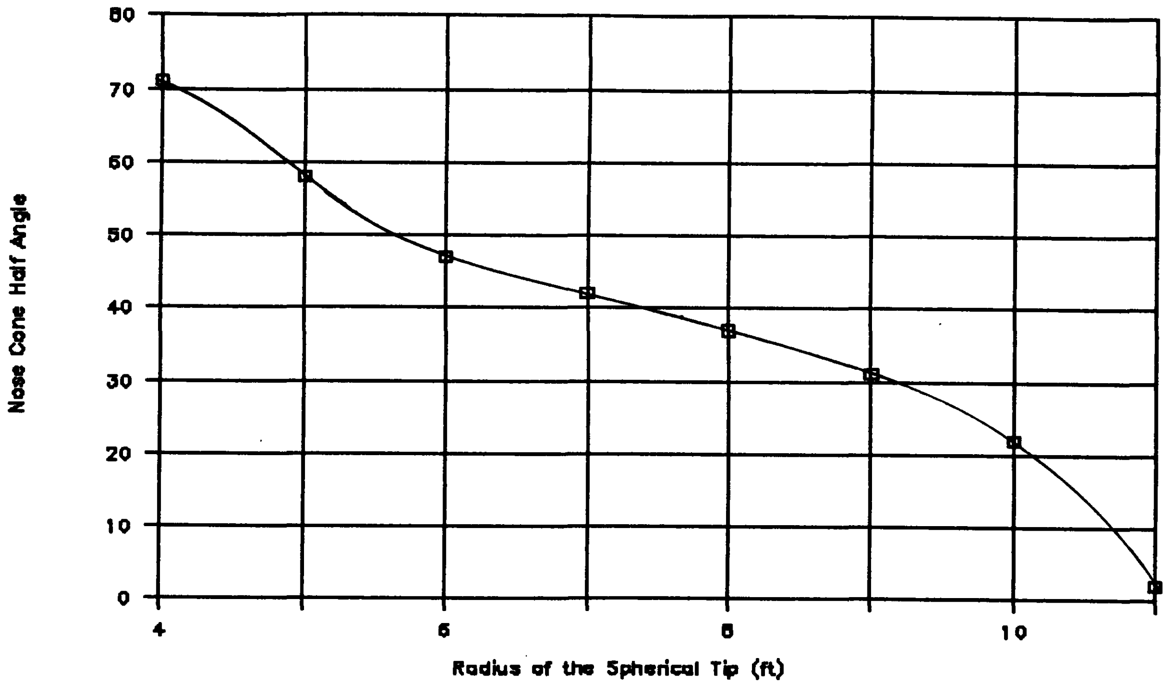

Figure 5.6: **Half Angle versus r for** $\dot{q}_s = 30$ Btu/ft^2-sec

angle of 30°, a "tip" radius of 9.2 ft is required. This is 67% of the base radius. On the other hand, if the end of the nose cone is allowed to ablate, Figures 5.1-5.5 show that the heat flux drops rapidly away from the stagnation point, and a small ablative tip would allow a geometry with much less drag. For example, according to Figure 5.2, a nose cone half angle of 30° and a tip radius of 6 ft only require an "ablation region" down to 36° from the stagnation point. (See Figure 3.1.)

A. Theta = 71° and r = 4 ft

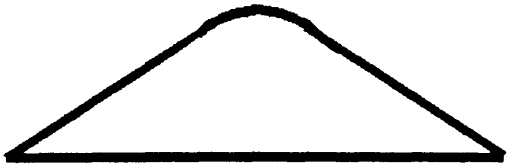

B. Theta = 58° and r = 5 ft

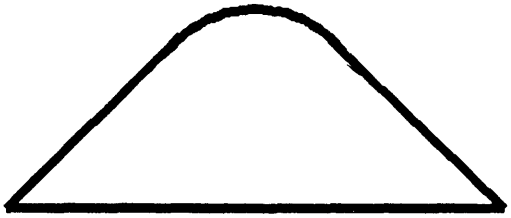

C. Theta = 47° and r = 6 ft

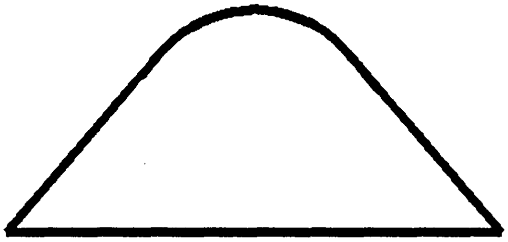

D. Theta = 42° and r = 7 ft

Figure 5.7: **Geometries of Various Limiting Non-Ablating Nose Cones**

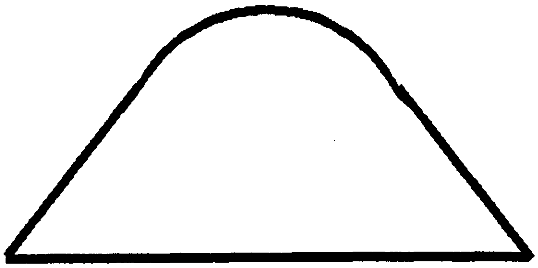

E. Theta = 37° and r = 8 ft

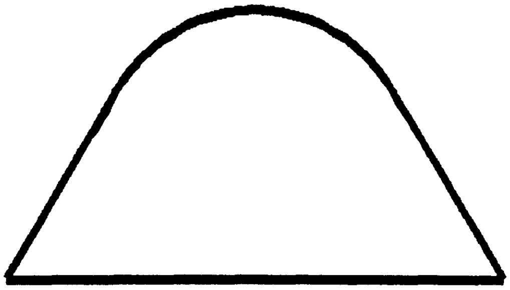

F. Theta = 31° and r = 9 ft

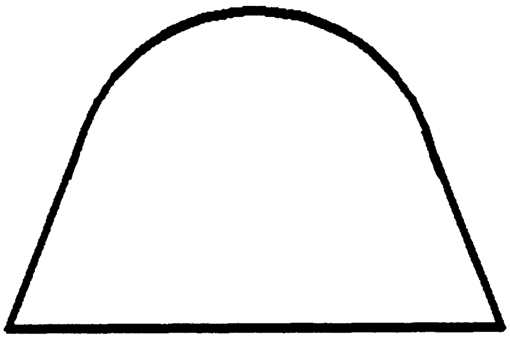

G. Theta = 22° and r = 10 ft

Figure 5.7: (Continued)

5.2 Water Impact Calculations

5.2.1 Theory

Like with reentry heating, the water impact loads provide a series of boundary conditions on the nose cone geometry. In order to determine these effects, the critical loads must be computed for the different geometries. This proves to be a very complicated task, since this critical load is not only dependent on the nose cone's geometry, but also on factors such as its internal pressure, how it is stiffened and supported, and the bending and extensional stiffness of each of its parts [52, p. 1]. The determination of each of these parameters is part of a complicated iterative process dependent on the various loads (and temperatures) the nose cone will see. In order to gain a very rough idea of the various critical loads, an equation from Reference [52] can be used. Assuming the nose cone is an isotropic conical shell (in reality it will consist of a shell with a series of support rings inside), the maximum membrane compressive stress can be estimated as:

$$\sigma_{max} = \frac{\gamma E t' \cos\theta}{\sqrt{3(1-\mu^2)}r} \tag{5.1}$$

where $\gamma \approx .33$ for $10^o < \theta < 75^o$ (this provides a "lower bound to the experimental data" [52, p. 4]), E is Young's modulus, μ is Poisson's ratio, t' is the skin thickness, θ is the cone half angle, and r is the radius of the tip of the cone. The critical impact force can thus be approximated as

$$F_{crit} = \sigma_{max} S_w$$

where S_w is the area of the submerged portion of the cone (the wetted area). Since the surface area of a cone is

$$S = \pi R^2 / \sin\theta,$$

defining x = submerged depth and assuming the tip is conical for this calculation,[4]

$$S_w = \pi x^2 \tan\theta \sec\theta.$$

Assuming the nose cone primarily consists of an aluminum alloy, $E \approx 10.5 \times 10^6$ psi and $\mu \approx .31$. Equation 5.1 thus becomes:

$$F_{max} = (9.519 \times 10^8 \,\mathrm{lb/ft^2}) \frac{t' x^2}{r} \tan\theta \qquad (5.2)$$

Using Equation 4.4 to compute X_{max} for a variety of nose cone angles, F_{max} can be computed as a function of nose cone angle. The results are shown in Figure 5.8, where $F_{max} \times r$ is plotted for various nose cone half angles and a skin thickness of .1 inches. This figure shows that the critical impact force decreases with increasing cone angle in a tangential relationship. This is because as the nose cone increases, X_{max} decreases faster that the corresponding increase in the conical area, and the wetted area is reduced. Thus the maximum impact load operates on a much smaller area.

Because of all the estimations made, Figure 5.8 cannot be used to obtain numerical results, but just as a conceptual guide. In reality, the tubing and engines in the JRB would be the most susceptable items to axial g loads and will probably

---

[4] Any error this assumption causes is well within limits for the equations used.

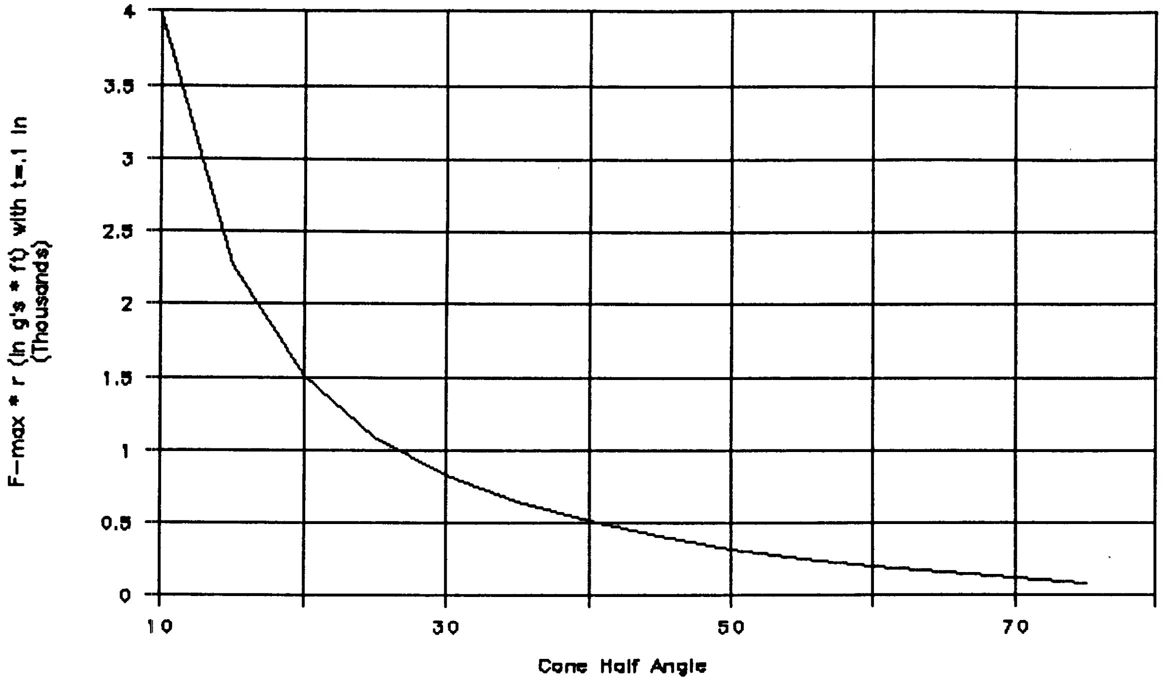

Figure 5.8: **Calculated Values for** F_{max}

drive the design. Given that the parachute deployment loads will provide around 15 g's of axial loading and Reference [44] predicted Apollo axial g loading at impact in the mid 20's, the critical JRB axial load will be considered somewhere between the two.

Calculations of the impact forces on the booster were made using Equations 4.2 and 4.3. The results for different impact speeds are shown in Figures 5.9, 5.10, 5.11, 5.12, and 5.13 for nose cone half angles of 10°, 20°, 30°, 40°, and 50°, respectively. It should be remembered that these approximations rapidly lose their validity past the point of maximum force, and they do not include the effect of buoyancy. Because of this latter point, the buoyancy force was calculated as if it was acting independently,

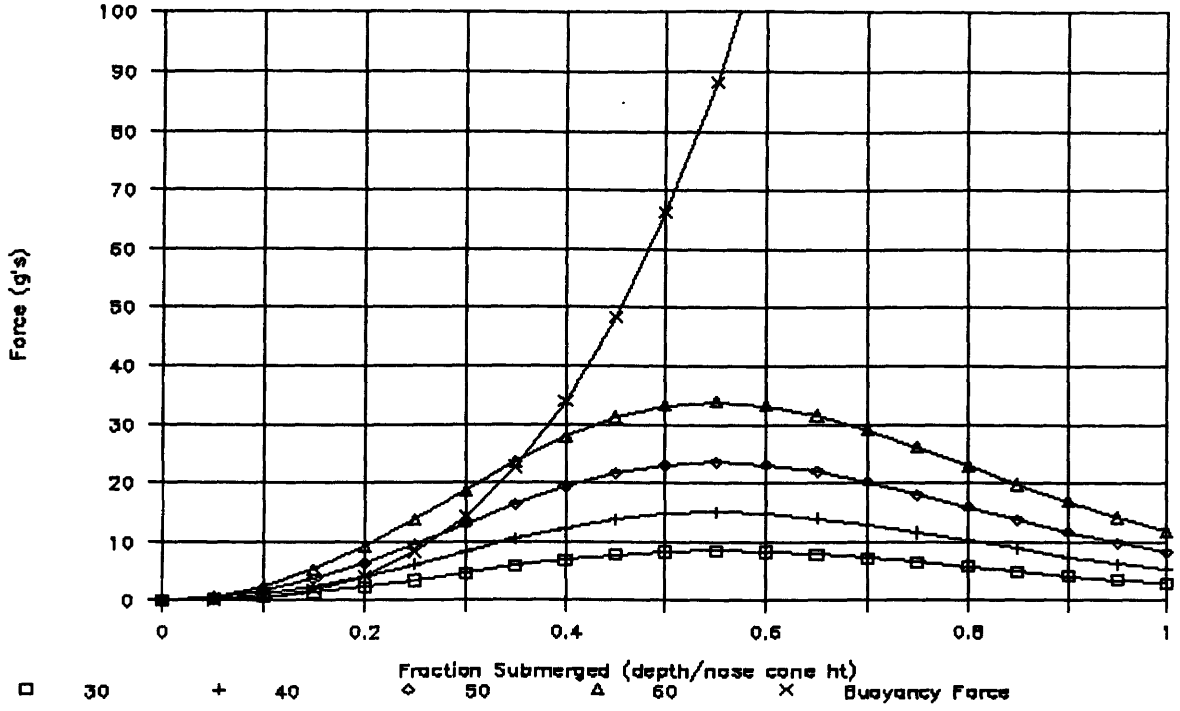

Figure 5.9: **Impact Force with a Half Angle of 10°**

using the equation

$$F_B = V'\rho g = \frac{1}{3}\pi r^2 x \rho g = \frac{\pi}{3} x^3 \rho g \tan^2\theta,$$

and plotted on these figures for comparison. Figure 5.14 shows how the maximum impact force is influenced by the cone angle at different impact velocities. A lot of information can be obtained from Figure 5.14. It shows that both an increase in cone angle and an increase in impact velocity have a large effect on the impact force. For smaller nose cone angles an increase in velocity has less of an effect, and likewise for slower impact velocities an increase in nose cone angle causes less of an increase in impact force. This means that a smaller nose cone angle is advantageous not only because it reduces the impact force, but because it allows for a comparatively

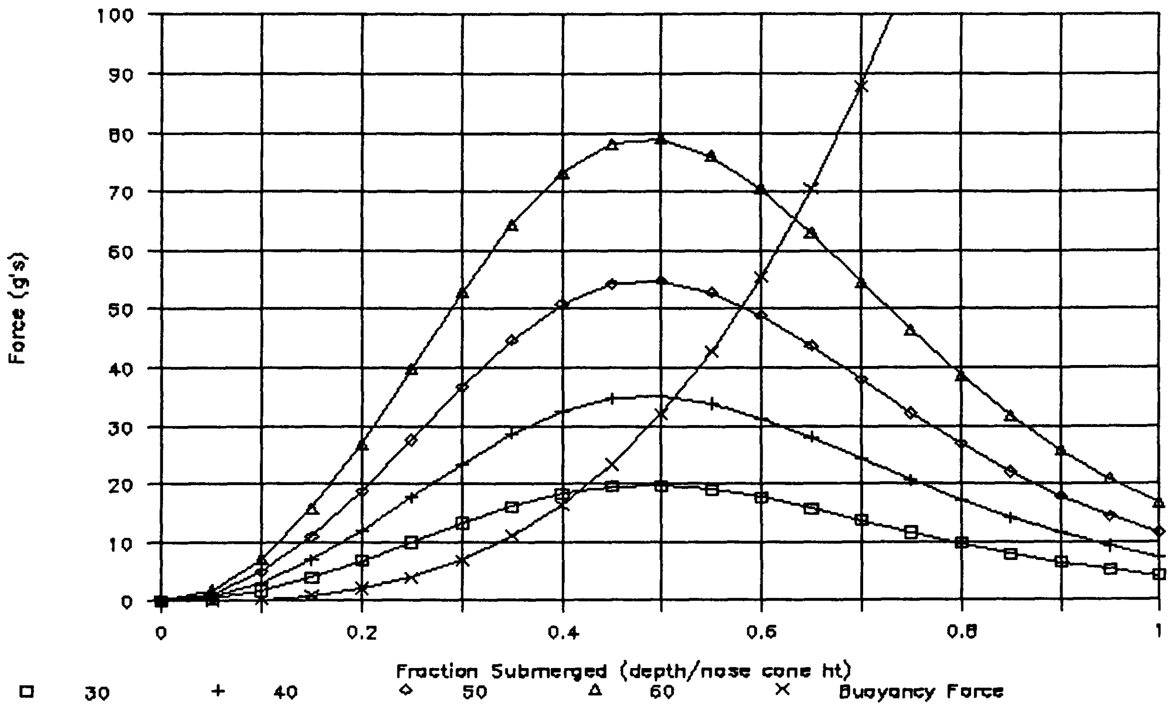

Figure 5.10: **Impact Force with a Half Angle of** 20^o

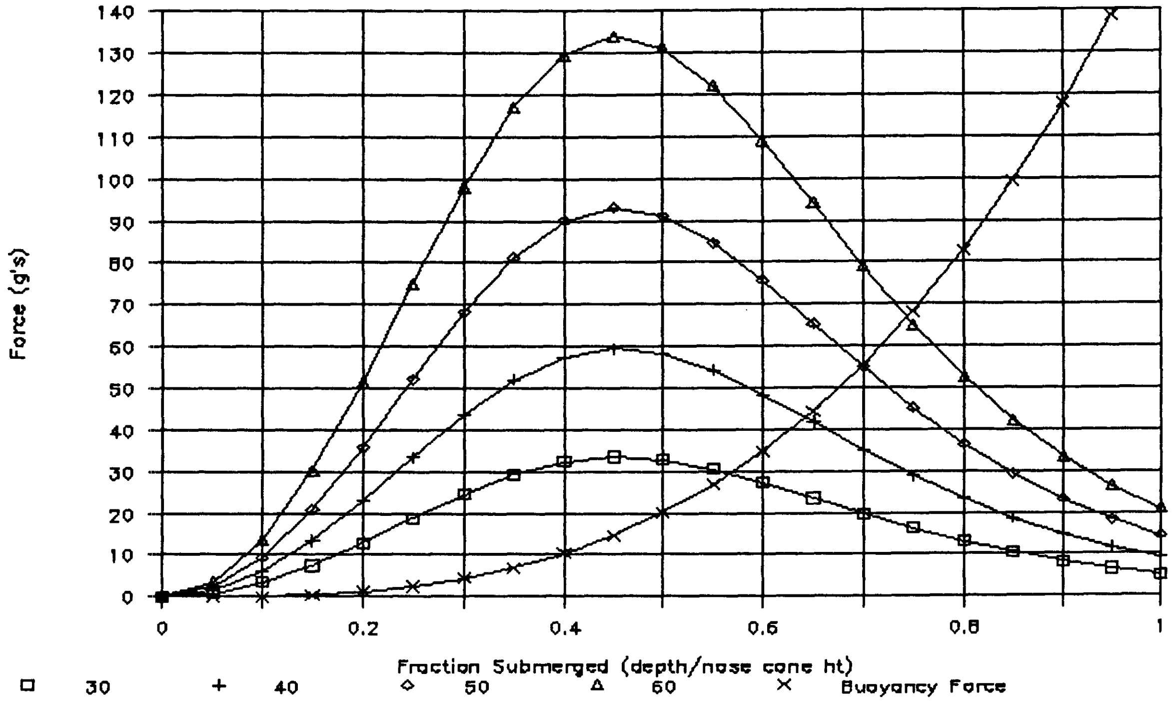

Figure 5.11: **Impact Force with a Half Angle of** 30^o

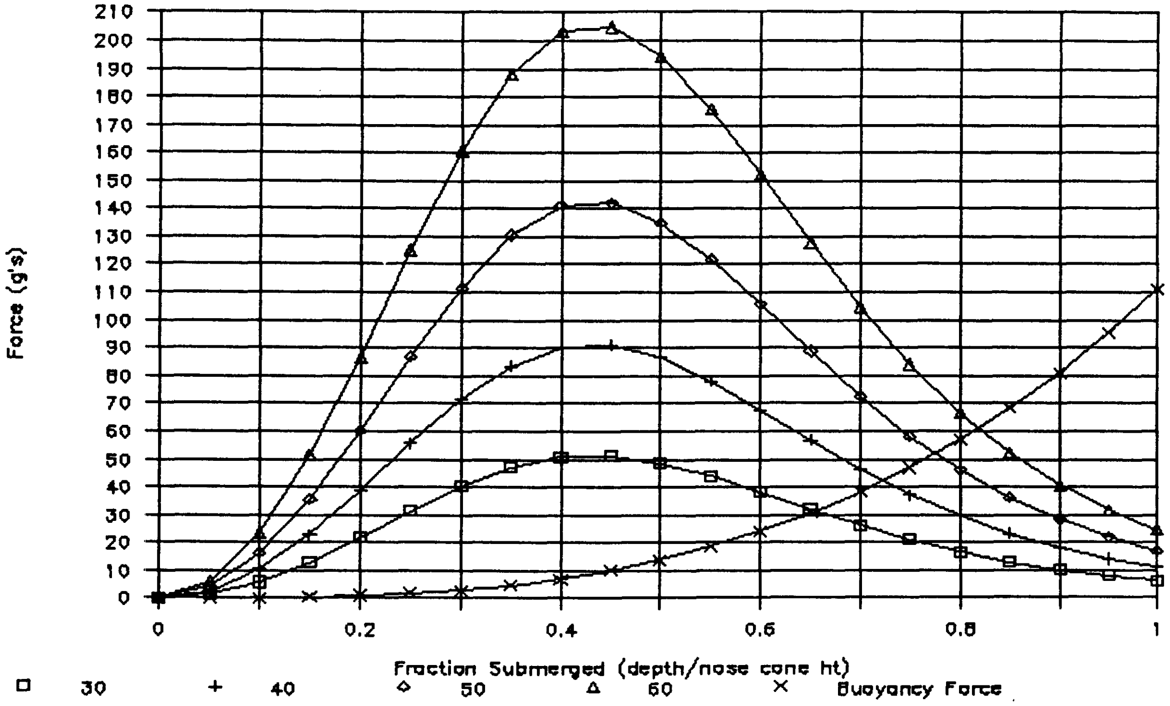

Figure 5.12: **Impact Force with a Half Angle of** 40°

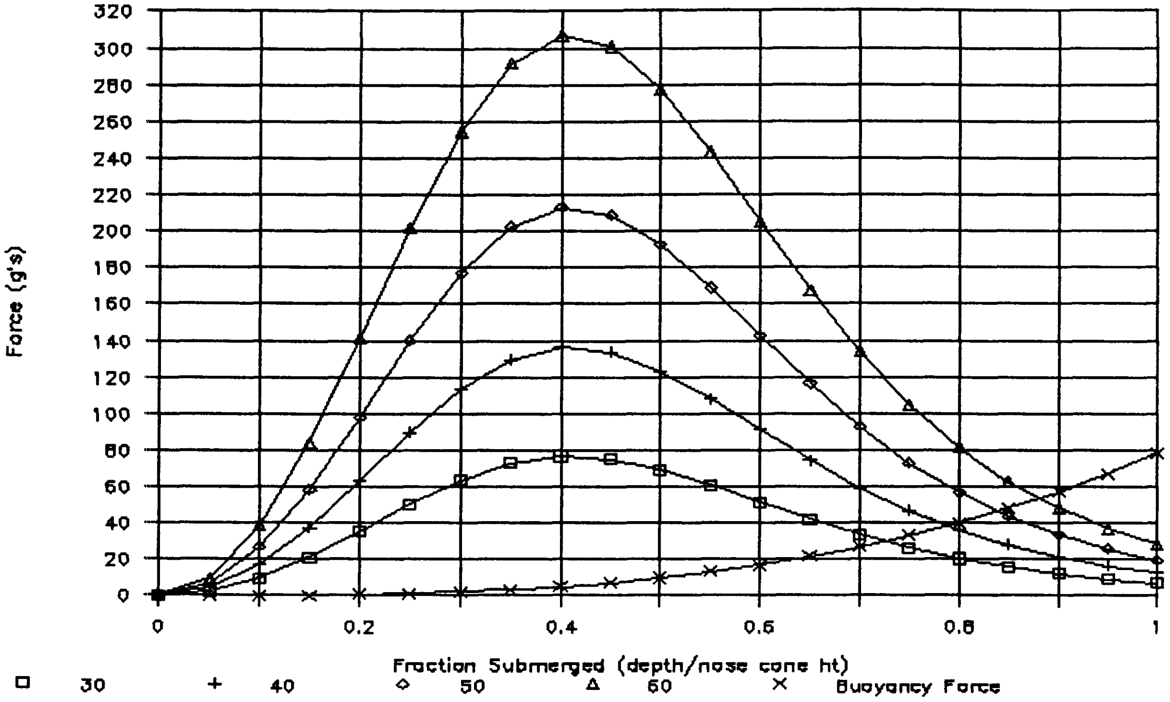

Figure 5.13: **Impact Force with a Half Angle of** 50°

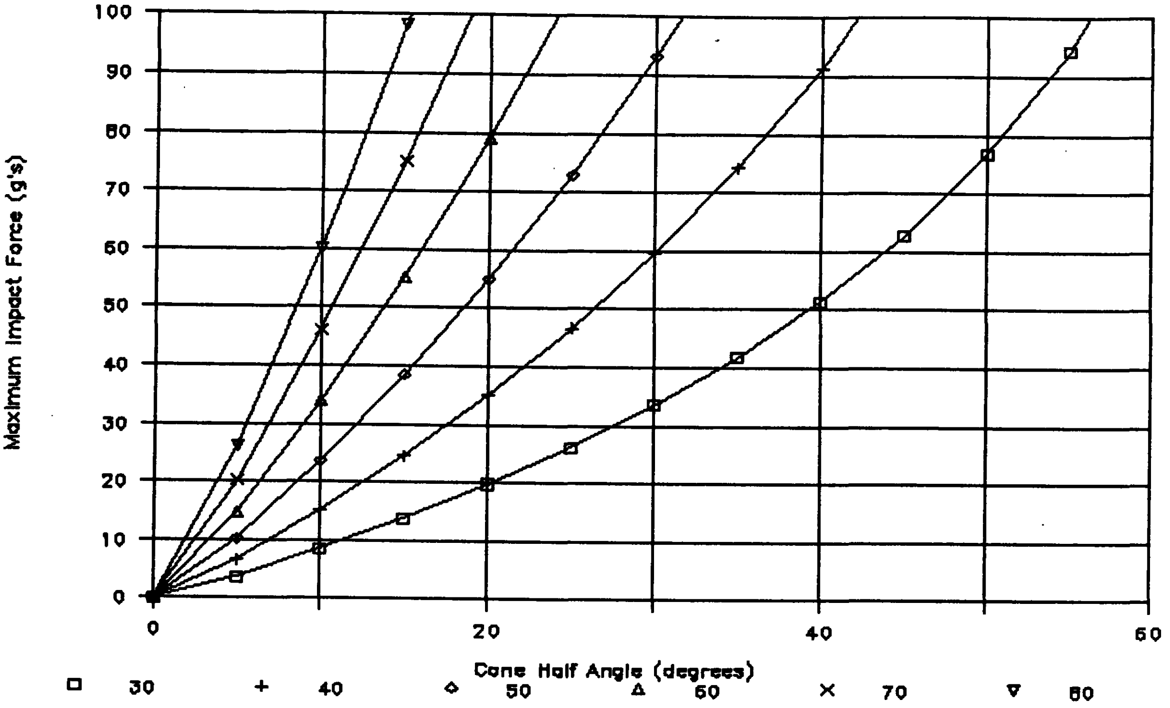

Figure 5.14: F_{max} **versus** θ **for Different Values of** V_o **(in ft/sec)**

greater increase in impact velocity. This in turn allows the recovery system to be designed so that if a chute were to fail to open, the JRB could take the comparatively small extra force. The range of geometries and impact speeds open is quite small however. Even if a generous 30 g's was allowed at impact, and an impact velocity of 30 ft/sec was obtained, the nose cone half angle would have to be less than 30°. Another point to be considered is that of the buoyancy force, which was left out of Equation 4.2.

Figures 5.9 to 5.13 show that for an object with properties similar to those of the JRB and with a small nose cone angle, the buoyancy force can be a large part of the total load. (Weight still has not been included, but obviously a downward force of only 1 g will have comparatively little effect.) For a half angle of 10° and impact velocities greater than 60 ft/sec the buoyancy force is greater than the impact force when the latter reaches its maximum. It is not until a little over 20^o that the buoyancy force remains less than the impact force for impact velocities of 30 ft/sec. This buoyancy force will thus substantially increase the total deceleration forces acting on the booster during impact, and thus further decrease the "window" of available angles and speeds in Figure 5.14. In addition, as the drop test showed (see Section 5.2.2), the buoyancy force causes an exagerated rebound effect.

5.2.2 Testing

The model described in Section 4.4.3 was tested according to the procedure described on pages 88 to 89. Four different nose cones were modeled. Shown in Figure 5.15, they consisted of a "baseline" nosecone with $\theta = 30.5^o$ and $r = 30$ in, one with $\theta = 30^o$ and $r = 6$ ft, one with $\theta = 20^o$ and $r = 6$ ft, and a "minimum heating" shape. The latter, which was nearly a flat surface, was calculated for a fineness ratio of $\tau = 1.5$ using the results of Baker and Kramer described in Section 3.3. Each of these nose cones was subjected to simulated impacts of 40 ft/sec, 50 ft/sec, 60 ft/sec, and 70 ft/sec. As mentioned previously, they were filmed with a videotape camera advancing at 30 frames per second. Since the average time from the first contact with the water to the maximum depth was only about .3 sec, there were an insufficient number of frames to obtain deceleration (and thus force) measurements. In addition, except for places where the booster changed directions

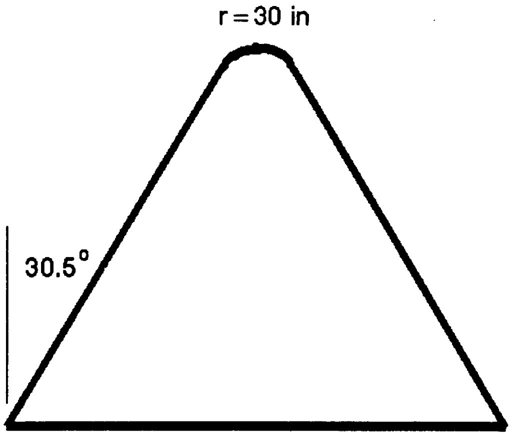

A. First Nose Cone Tested (Nominal)

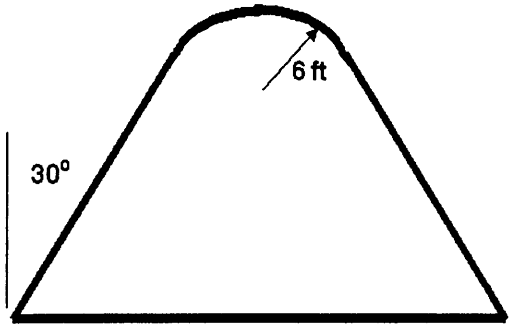

B. Second Nose Cone Tested

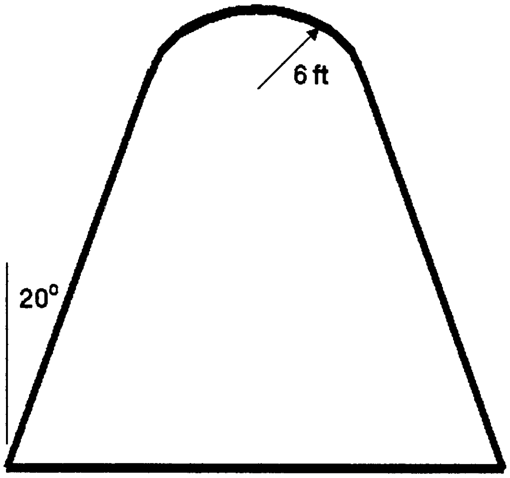

C. Third Nose Cone Tested

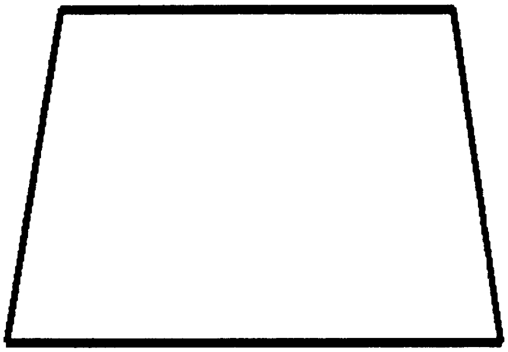

D. Fourth Nose Cone Tested
(Minimum Heating)

Figure 5.15: **Shapes of the Nose Cones Tested**

(like at maximum depth and height), most of the frames were too blurry to allow for a measurement more accurate than 1/2 a grid mark (.44 in) to be taken. (The maximum depths of impact were only 6 to 8 in.) A high speed camera or videotape is thus recommended for future studies.[5] Despite these limitations, a lot can be gained by studying the vehicle dynamics of each configuration.

The first nose cone tested was the nominal case with a simulated impact velocity of 40 ft/sec. As shown in Figure 5.16, its maximum depth of impact was just greater than the length of the nose cone. At this point buoyancy forces took over and the model rebounded to the position shown in Figure 5.17. Here it can be seen that the nose cone is just barely submerged and that the weight of the engines has begun to pull the rear portion of the booster down. The outer ring visible on the water is the wave from the initial impact. At this point the booster begins to reenter the water, while at the same time whip and the center of mass pull the aft end down. This causes the model to literally slide diagonally back into the water along one side with the nose cone eventually tipping up out of the water as shown in Figure 5.18. Here it is seen that the aft end impacts the wave caused by the initial impact and becomes partially submerged. The nose cone then rocks back down, followed by the aft end, and after a couple of times this motion damps out and the booster floats almost completely out of the water. In this test, cavity collapse was not observed as the vehicle rebounded very quickly and the waves radiated outward. However, in

---

[5] They were unavailable for this project due to cost.

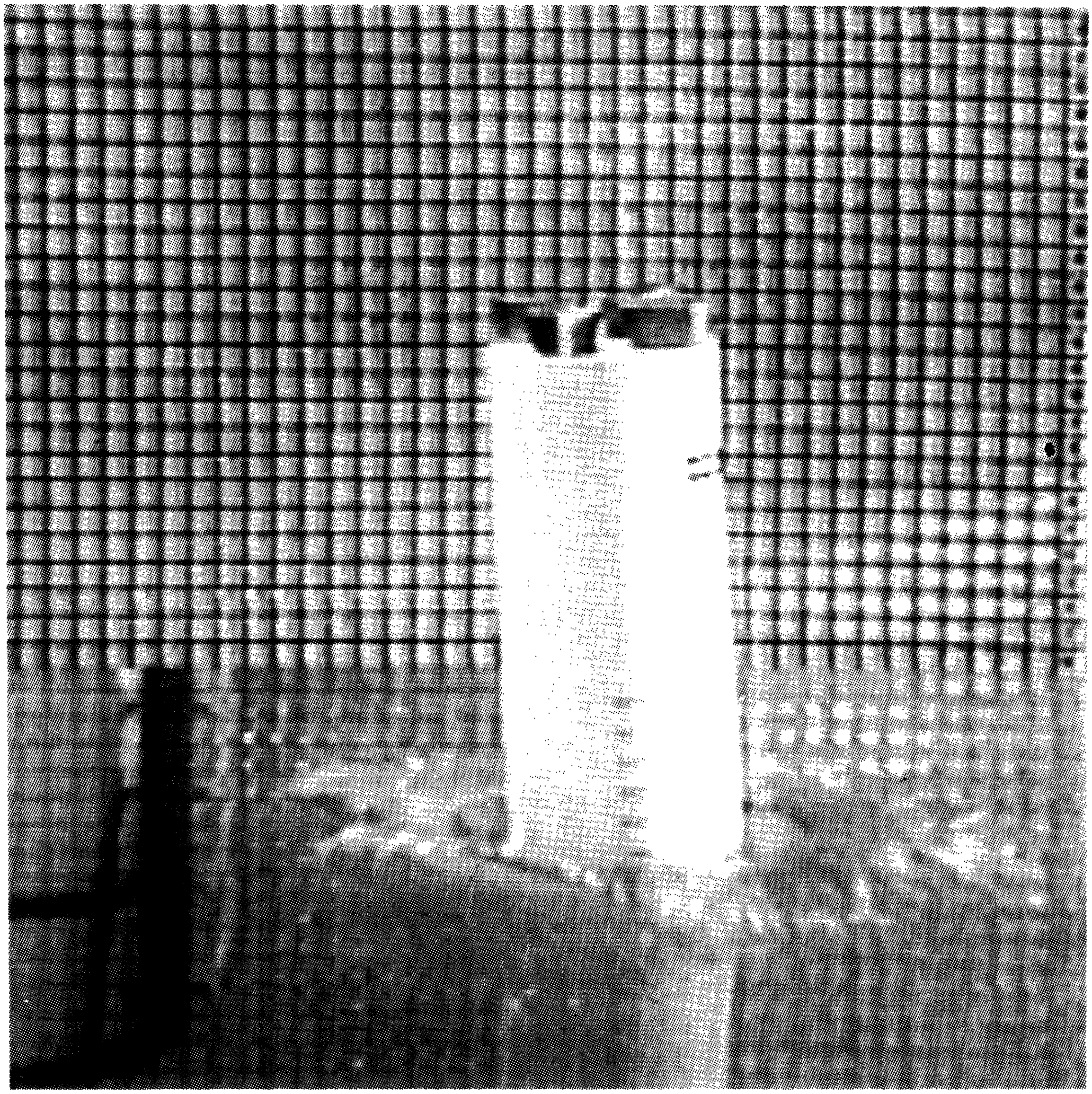

Figure 5.16: **Nominal Nose Cone at 40 ft/sec — Maximum Depth**

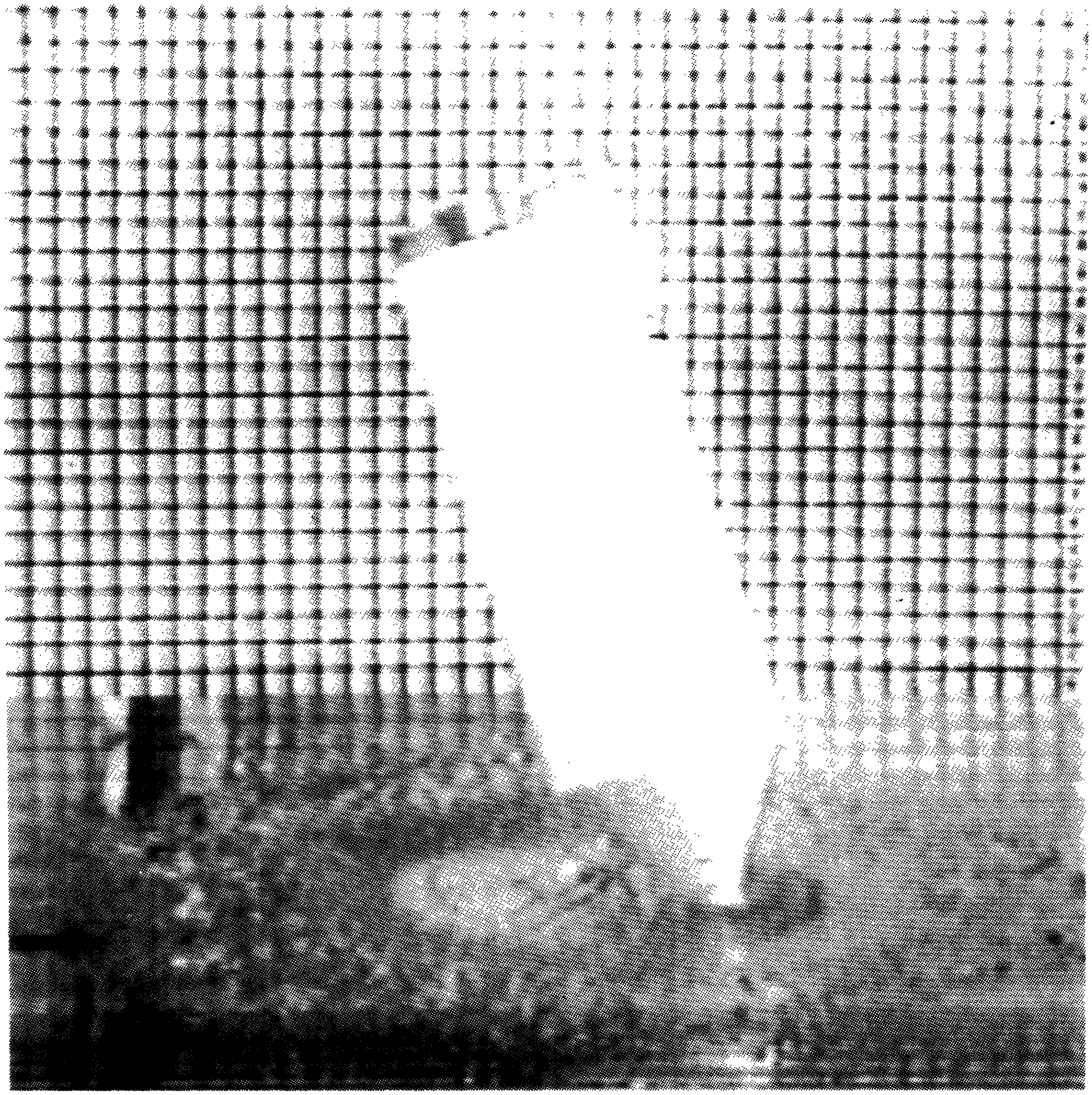

Figure 5.17: **Nominal Nose Cone at 40 ft/sec — Rebound Height**

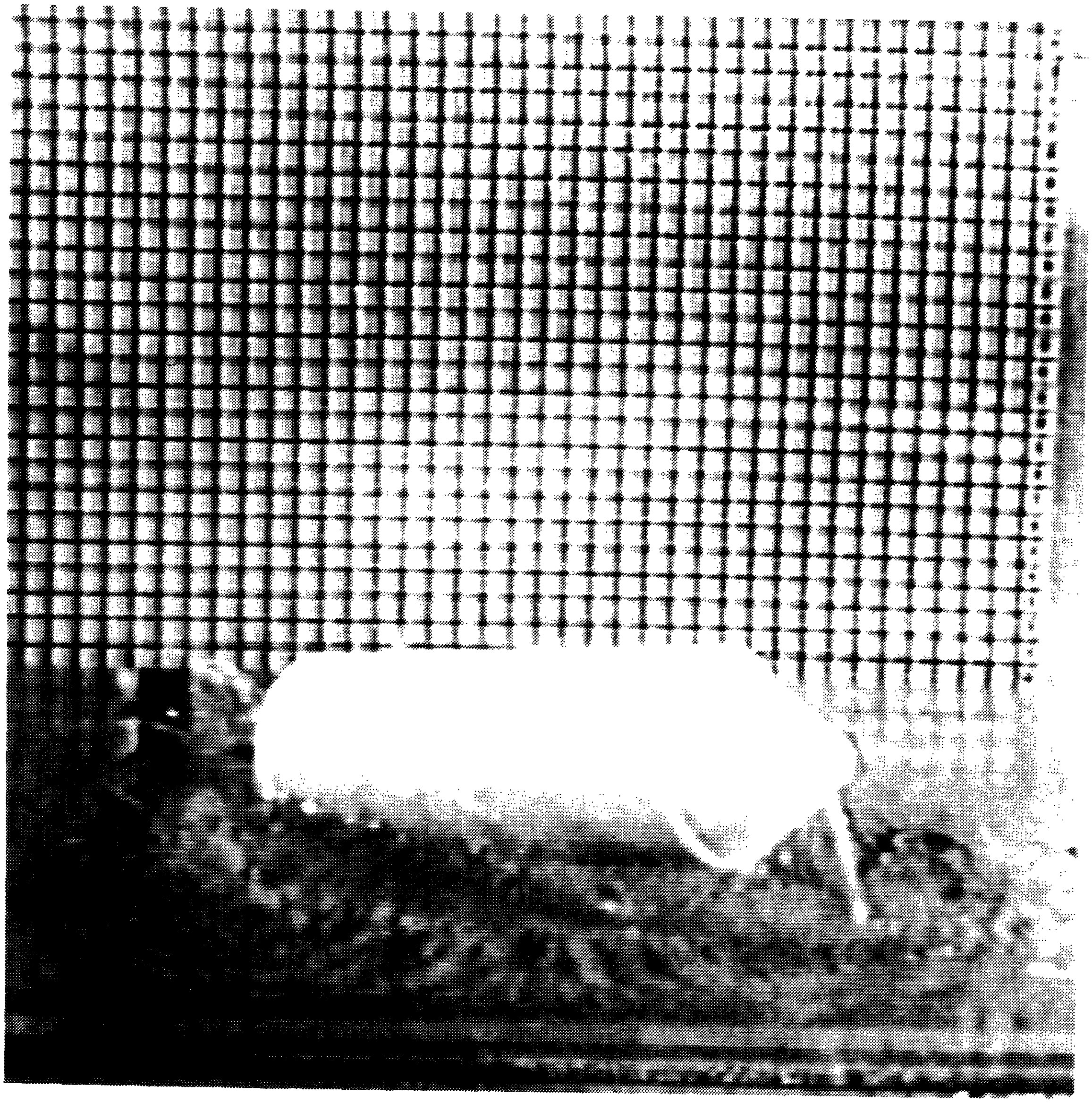

Figure 5.18: **Nominal Nose Cone at 40 ft/sec — Second Impact**

Figure 5.17, water is visible clinging to the bottom of the nose cone, so there may have been at least a small scale cavity collapse in the region of the tip of the nose cone.

When this nominal configuration was tested at a simulated 50 and 60 ft/sec, the results were very similar. In both cases the nose actually cleared the surface of the water on rebound, however water still clung to its surface. This had the probable effect of slightly reducing the rebound height, and thus showed that the effects of surface tension should be more closely examined in future studies. In both cases the aft end also impacted on the initial wave, submerging up to 1/2 of this end in the water. When tested at 70 ft/sec however, the nominal configuration behaved slightly differently. After the initial rebound the booster nose cone (above the water's surface, but with water still clinging to it) reentered at a very small angle, and before whip could act the buoyancy force took over. This pushed it back out of the water, at which point it "slid" back in like the previous cases. The engines were submerged more than half way after the aft end impact, and the rocking was slightly more pronounced.

The 30° nose cone with a simulated 6 ft nose radius behaved very similarly to the nominal case at the slowest velocity. As shown in Figure 5.19, it did rebound to a slightly greater height, but the water still clung to the tip. During the second impact the booster also slid along its side before the aft end hit and the nose rose above the water. Figure 5.20 shows the aft end at its maximum submergence. The

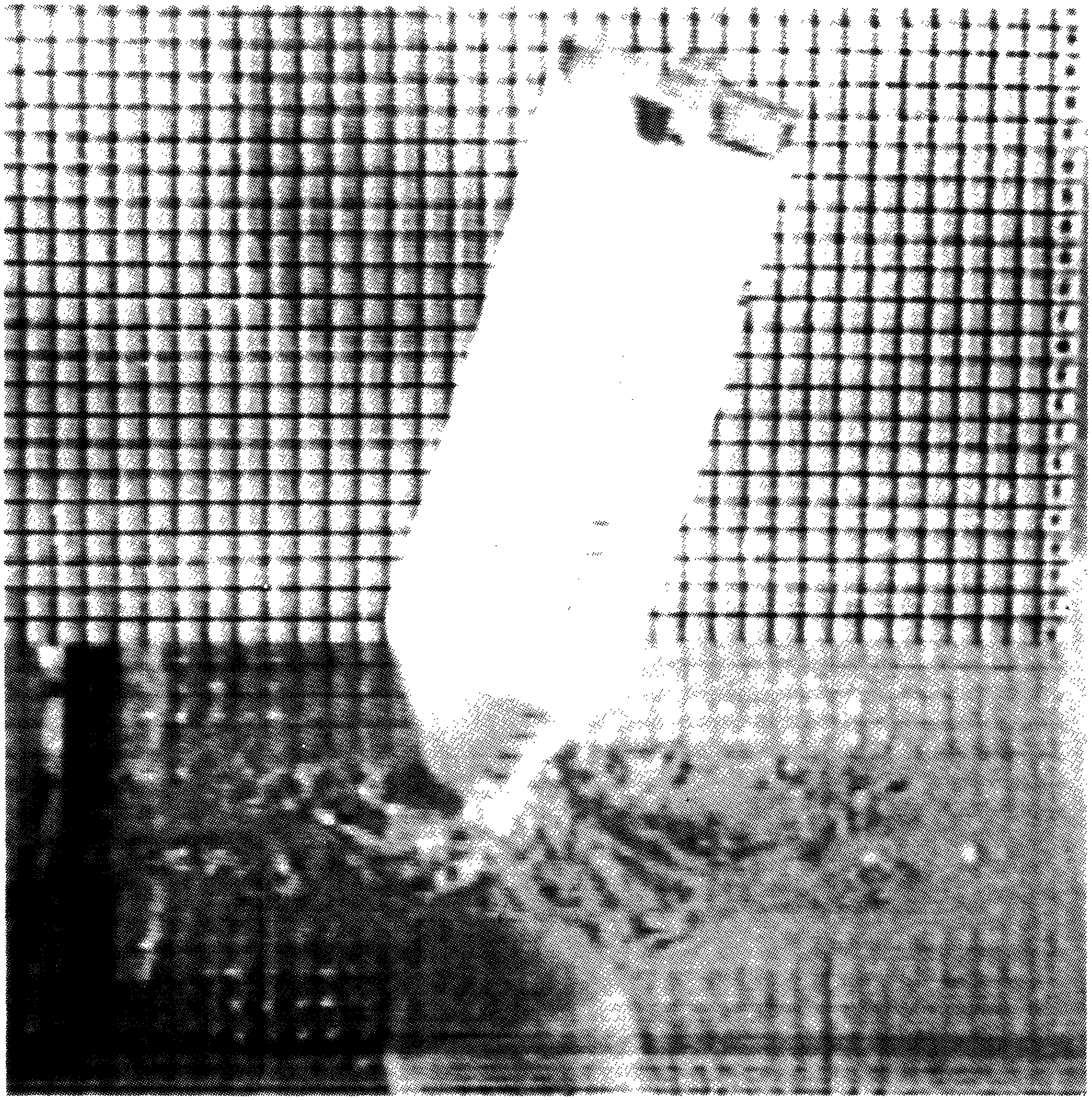

Figure 5.19: **Thirty Degree Nose Cone at 40 ft/sec — Rebound Height**

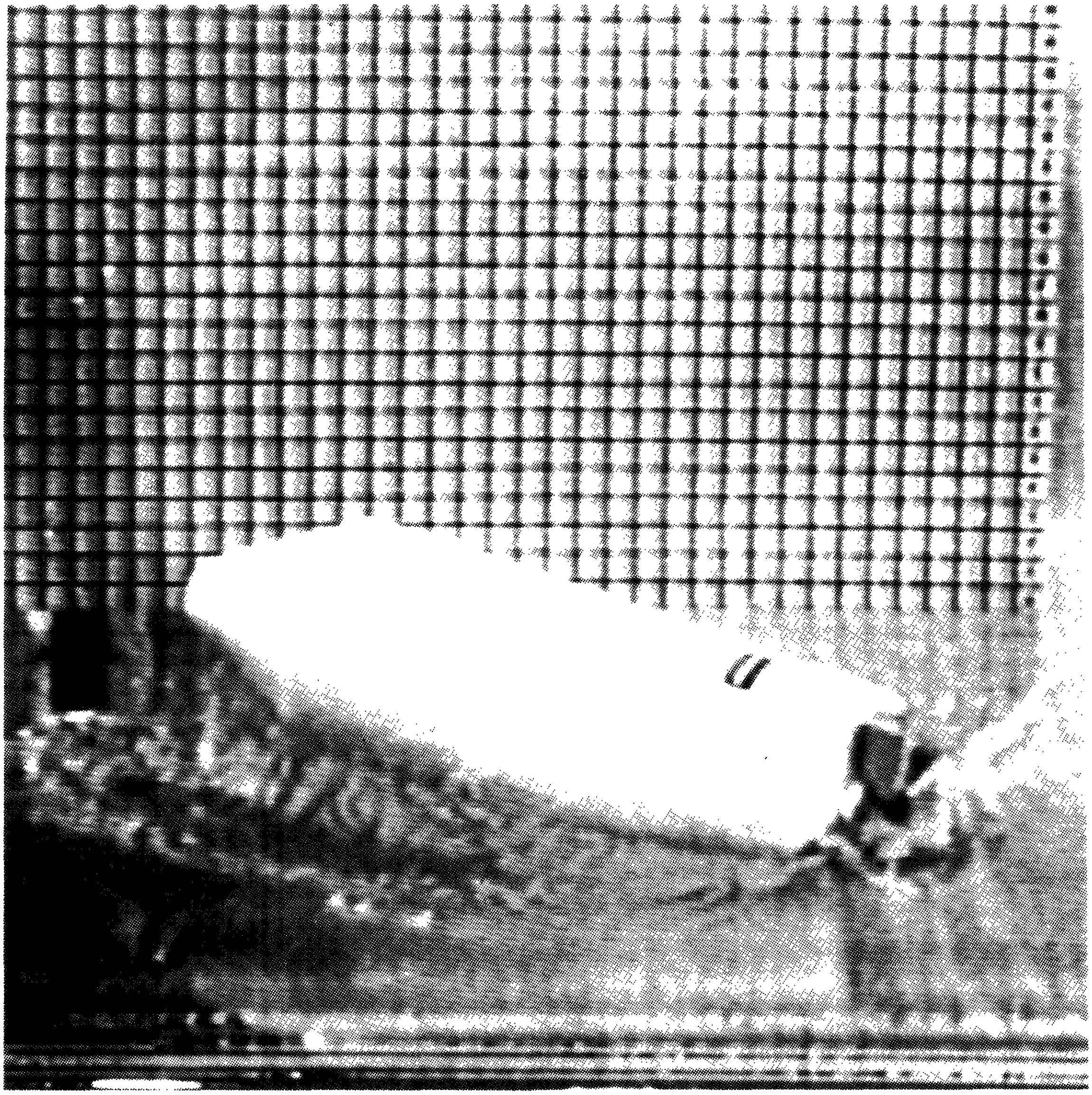

Figure 5.20: **Thirty Degree Nose Cone at 40 ft/sec — Second Impact**

surface tension effects along the side of the booster, which help to keep the nose cone from rising any further, are also visible. When this nose cone was tested at "50 ft/sec" it rebounded to the highest point yet, and reentered by first impacting the beginning of the cylinder and then the rear of the booster. At "60 ft/sec" after the rebound only a small amount of spray still clung to the booster, and it tipped around so that the edge of the aft end first hit the water on the second impact. At "70 ft/sec" the vertical drop was apparently straighter (there was no visible difference from the previous drops) since the booster reacted like the nominal case and "slid" back in the water nose cone first with the aft end submerging about half way before the booster "rocked" to a floating position on its side.

The 20° nose cone with a simulated 6 ft nose radius behaved like the other configurations at "40 ft/sec" except for a higher rebound height as shown in Figure 5.21. At "50 ft/sec," following the rebound the corner between the nose cone and the booster cylinder hit first, then the side and aft end impacted. At "60 ft/sec," though the rebound was obviously higher, the second impact began on the side of the nose cone as the side of the booster slid into the water. However, at "70 ft/sec" the large height of the rebound (see Figure 5.22) allowed the center of mass more time to swing the aft end down. This in turn caused the second impact to occur on the side of the booster with the aft end pointed slightly down. This fall was from a sufficient height that the impact velocity was equivalent to about 55 ft/sec. As shown in Figure 5.23, the resulting submergence was quite large.

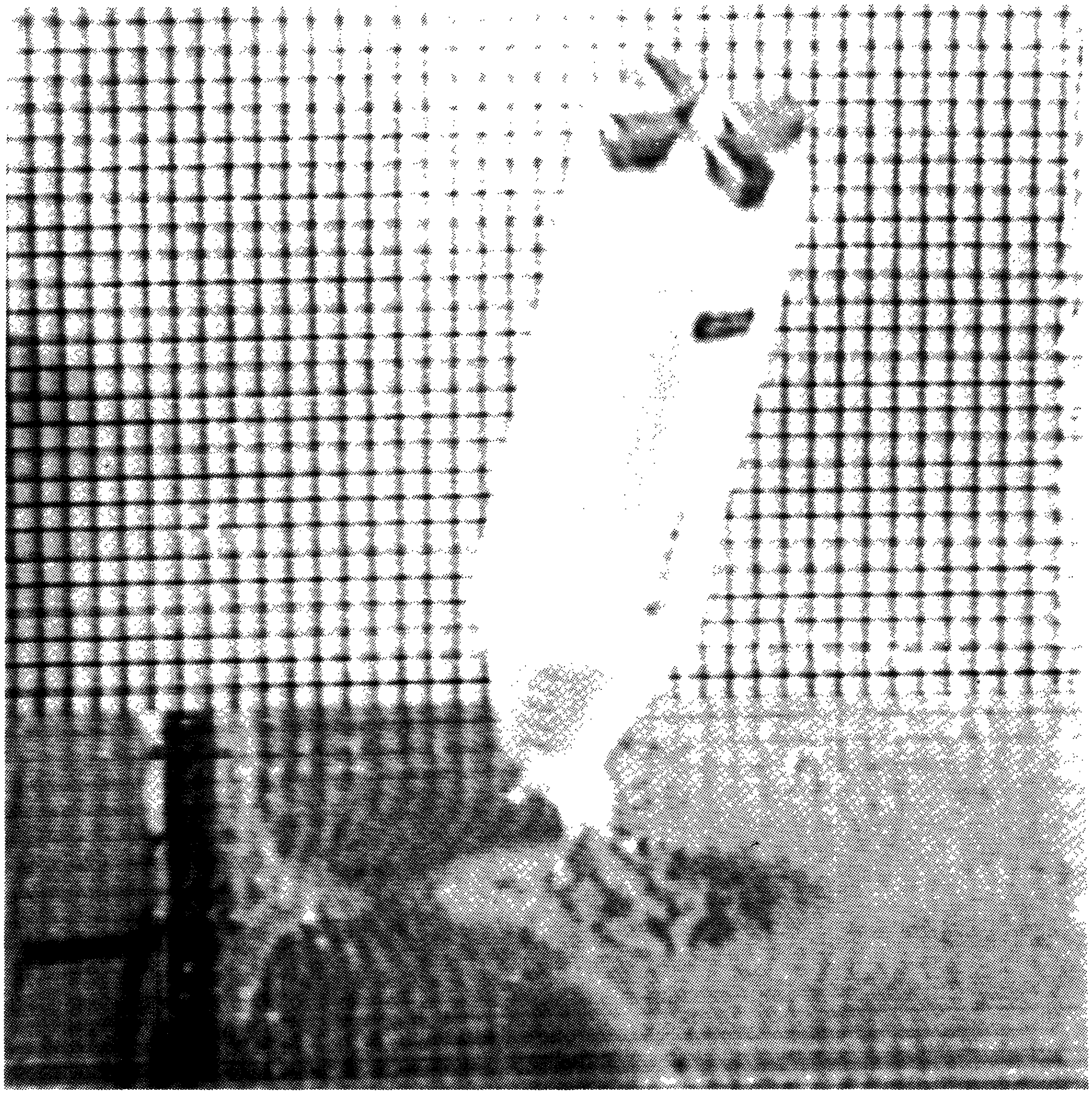

Figure 5.21: **Twenty Degree Nose Cone at 40 ft/sec — Rebound Height**

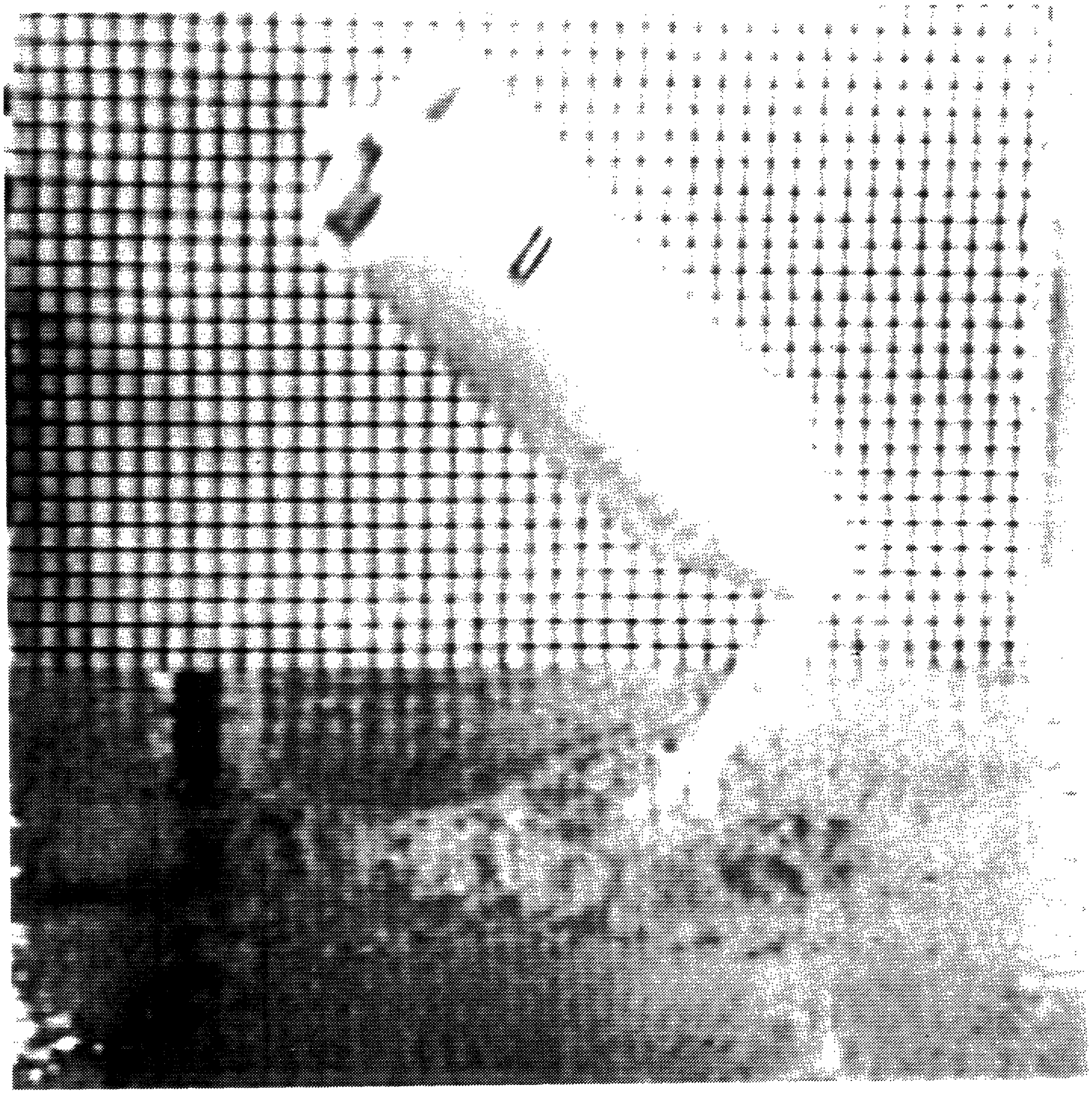

Figure 5.22: **Twenty Degree Nose Cone at 70 ft/sec — Rebound Height**

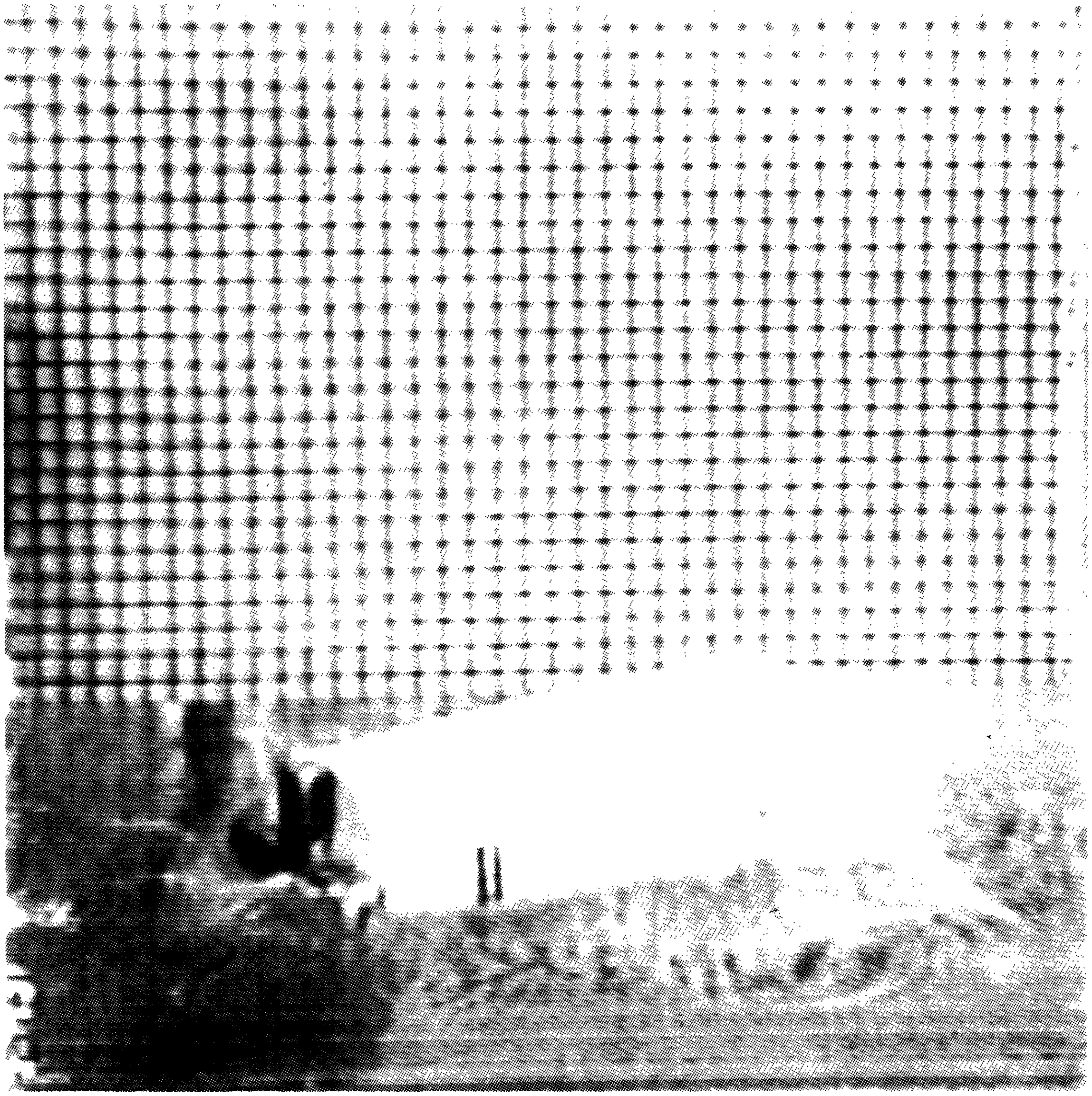

Figure 5.23: **Twenty Degree Nose Cone at 70 ft/sec — Second Impact**

The minimum heating nose cone hit the water at "40 ft/sec," rebounded to the surface, then simply fell over on its side. At "50 ft/sec" the booster rebounded to just above the surface (though water still clung to it), then settled back down and fell over. At "60 ft/sec" the first rebound was followed by a smaller second one which returned it to the surface of the water, after which the booster tipped over. Finally, at an impact speed of "70 ft/sec" the booster also had two rebounds, but the second one cleared the surface and the booster reentered at a slight angle, slipping down along its side. The highest point of the first rebound for the drop is shown in Figure 5.24. This figure illustrates how the nose cone's shape caused water to in effect "cling" to its whole flat surface, thus limiting the rebound height.[6]

Finally, a drop was done using the nominal nose cone and entering the water at an angle of about 20° and a speed of "40 ft/sec." This was accomplished by swinging the booster from the thread and then cutting this thread at the proper angle. Because achieving an exact impact angle and speed with this method is very difficult, a series of tests were not run. It is felt that on angled track on which the booster can "slide" into the water would provide the best method for testing impact at an angle.[7] This drop did show the powerful effect of whip however, as the nose cone first entered the water at an angle, then popped up and out as the aft end pivoted down and into the water with a lot of force. The nose cone then came back

---

[6] This effect is actually a form of the base drag discussed on page 29.

[7] This is the method used in the Apollo CM impact tests.

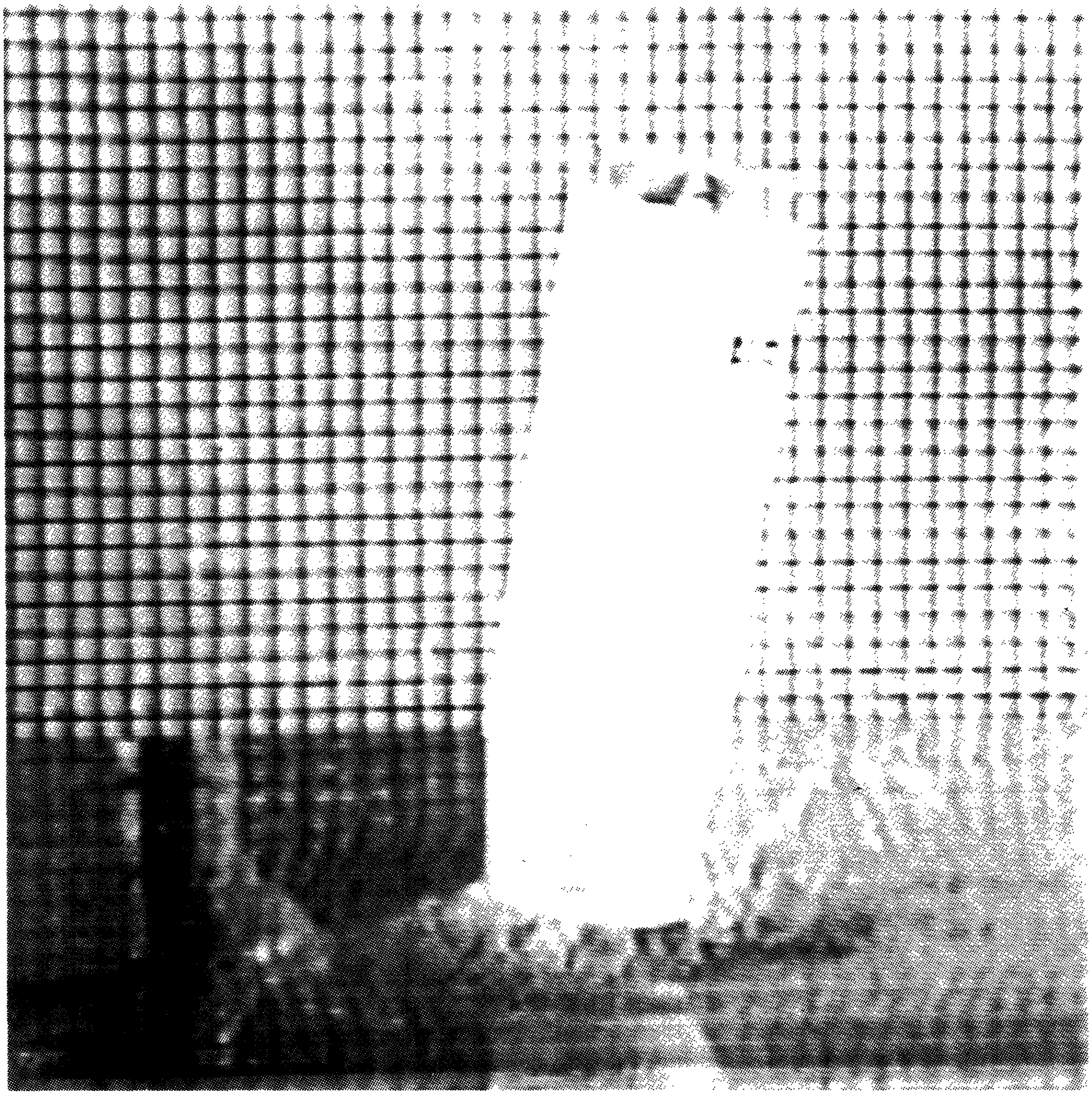

Figure 5.24: **Min. Heating Nose Cone at 70 ft/sec — Rebound Height**

down and the booster rocked back and forth for a little over a second.

In summary, the results of the water impact tests on this booster showed that its buoyancy caused vehicle dynamics unlike those which have occured for any previous vehicle. The booster actually experienced two impacts in most cases as the initial rebound pushed it almost, if not entirely, clear of the surface of the water. Increasing the impact velocity was found to increase the rebound height, which allowed more time for the aft-positioned center of mass to begin pulling this aft end down. On the other hand, the angular position of the body at impact had a much greater effect on how much of a moment was applied to the booster during rebound. For example, if the booster impacted the water in a perfectly vertical orientation it would rebound up and come straight back in, rebound again to a slightly lower height, and continue this cycle until some force, such as wind or ocean current, caused it to tip slightly. (In the tests there was a maximum of three impacts.) If it entered at just a slight angle, after the first rebound it would reenter the water nose cone first, but sliding along one side as discussed previously. However, a greater entry angle (or a correspondingly greater amount of time in the air after rebound) would allow this moment to have a larger effect and the second impact would occur further down the booster. The shape of the nose cones has two major effects. First of all, the smaller the cone angle the larger the buoyancy force and corresponding rebound height. Secondly, a smaller cone angle is more susceptable to whip during the first (and later) impact(s), and thus will usually cause the booster to rebound at a greater angle. Finally, except for the minimum heating nose cone, which hardly entered the water at all, on the first impact the different nose cones each submerged to about the same point on the booster, about 1/2 in from the edge of the cylinder. This was almost independent of velocity.

5.3 Drag and Mass Calculations

As explained in Section 2.2, it was expected that changes in nose cone drag and mass with geometry will have little effect on the performance of the booster. However, it is important to understand their effects for two reasons. First, by knowing how they affect performance the penalty of going with a reusable geometry can be assessed. Secondly, these results can be used to "fine tune" those obtained in the rest of this chapter.

Drag was computed as outlined in Section 2.3.3. First the nominal nose cone with $\theta = 30.5^o$ and $r = 30$ in was analyzed to obtain a reference value. The values of $C_{booster}$ obtained for it are shown in Figure 5.25. When these were combined with the fairing and base drag coefficients (see Figures 2.4 and 2.3) according to Equation 2.15, the total vehicle drag coefficient shown in Figure 5.26 was obtained. The baseline average drag computed from Figures 5.26 and 1.4 is 262,800 lb. This value was divided into that computed for other nose cones to give K_D, which was then used in Equation 2.6.

Mass was computed as outlined in Section 2.4 for various configurations at the

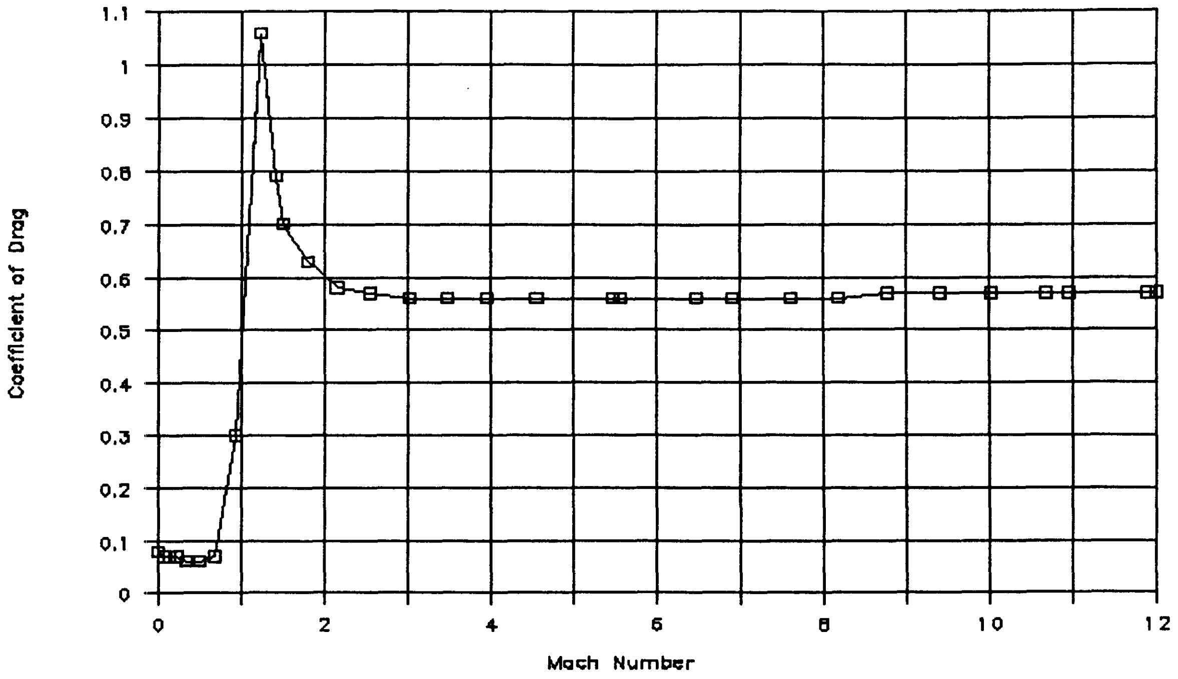

Figure 5.25: C_D **Versus M as Calculated for the Nominal N/C**

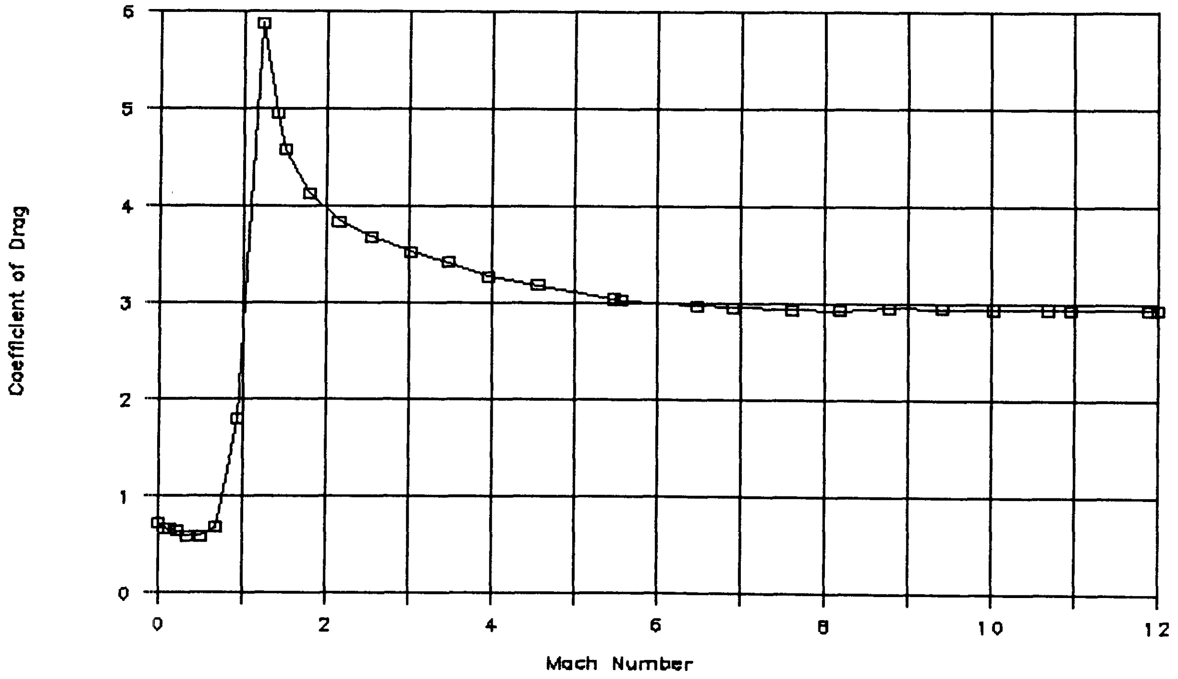

Figure 5.26: C_D **Versus M as Calculated for the Nominal Vehicle**

nose cone half angles given in Table 2.1. In addition to the aluminum mass obtained from Equation 2.16, an additional amount was added to account for the thermal insulation material. For example, for the nominal nose cone the mass was calculated as:

$$M = \frac{(2305\ \mathrm{lbm})(167,292\ \mathrm{in}^2)\sin 30.5^o}{\pi(130\ \mathrm{in})^2} + (2.004\times 10^{-3}\ \mathrm{lbm/in}^2)(167,292\ \mathrm{in}^2) \approx 4021\ \mathrm{lbm} \qquad (5.3)$$

This value of M was subtracted from that obtained for various different nose cones and the difference multiplied by 1.8 (see page 25) to get a change in payload mass to orbit.

In order to obtain an initial feel for the effects of drag and mass, computations were run on nose cones with half angles of 10^o, 20^o, 30^o, 40^o, 60^o, and 80^o and with tip radii of 0, 4 ft, and 8 ft. The results are shown in Figures 5.27, 5.28, and 5.29. These figures show that there is a fairly substantial variance in vehicle performance for large changes in the nose cone angle. In addition, the effect of a change in nose cone angle is much greater than that obtained when the tip radius is changed. The maximum possible performance improvement occurs with a nose cone drag of zero, and is about 12,000 lb. This however is for a zero degree nose cone angle, corresponding to an infinite mass. The optimum angle for minimizing mass is about 25^o in each case, and the corresponding increase in mass on either side of this angle is greater the smaller the tip radius. The difference between the nose cone drag and mass effects on payload to orbit is also shown in these figures under the

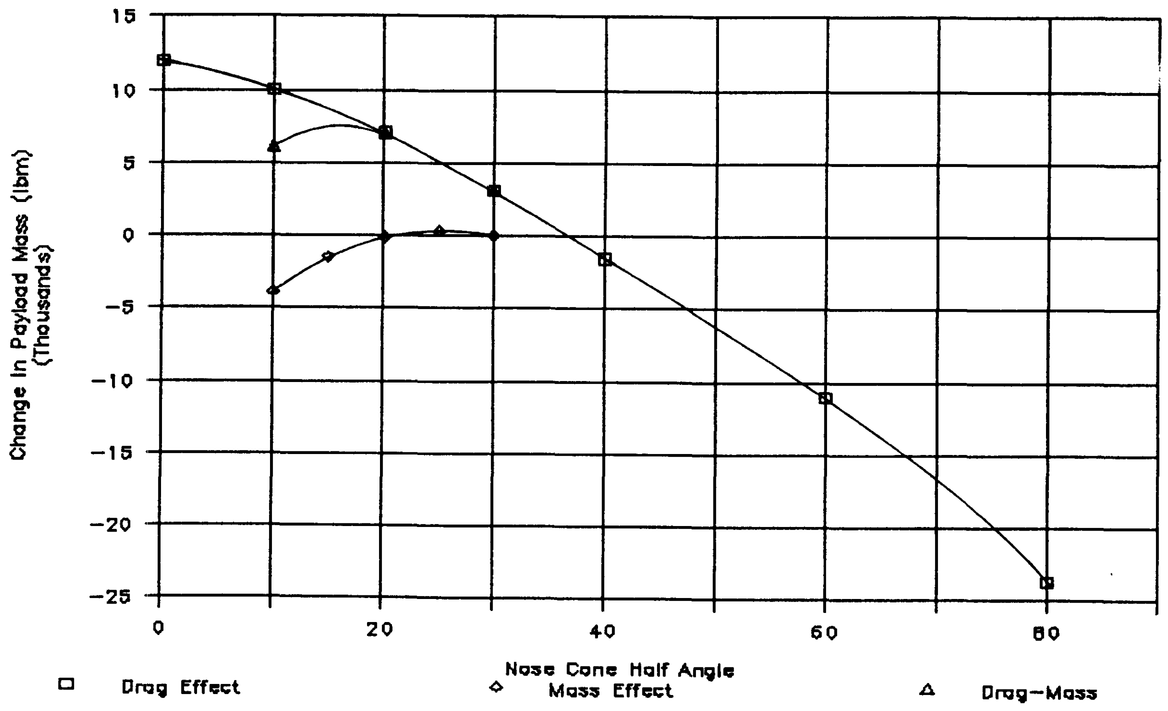

Figure 5.27: **The Effects of Drag and Mass when r=0**

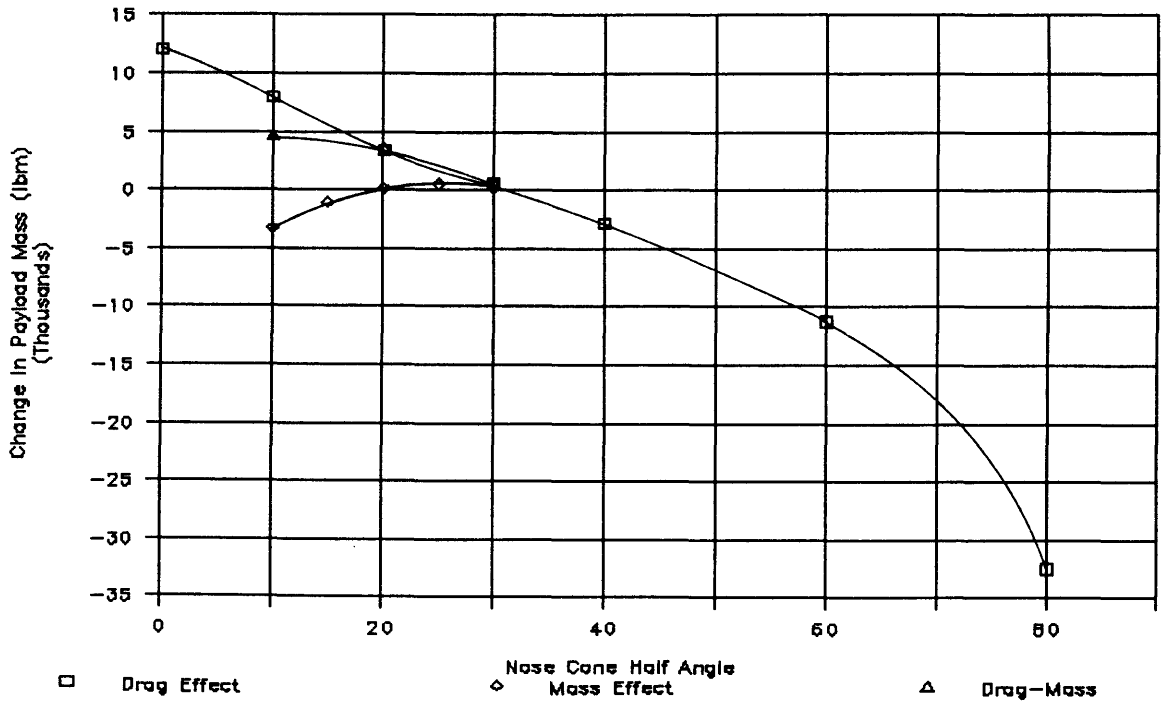

Figure 5.28: **The Effects of Drag and Mass when r=4**

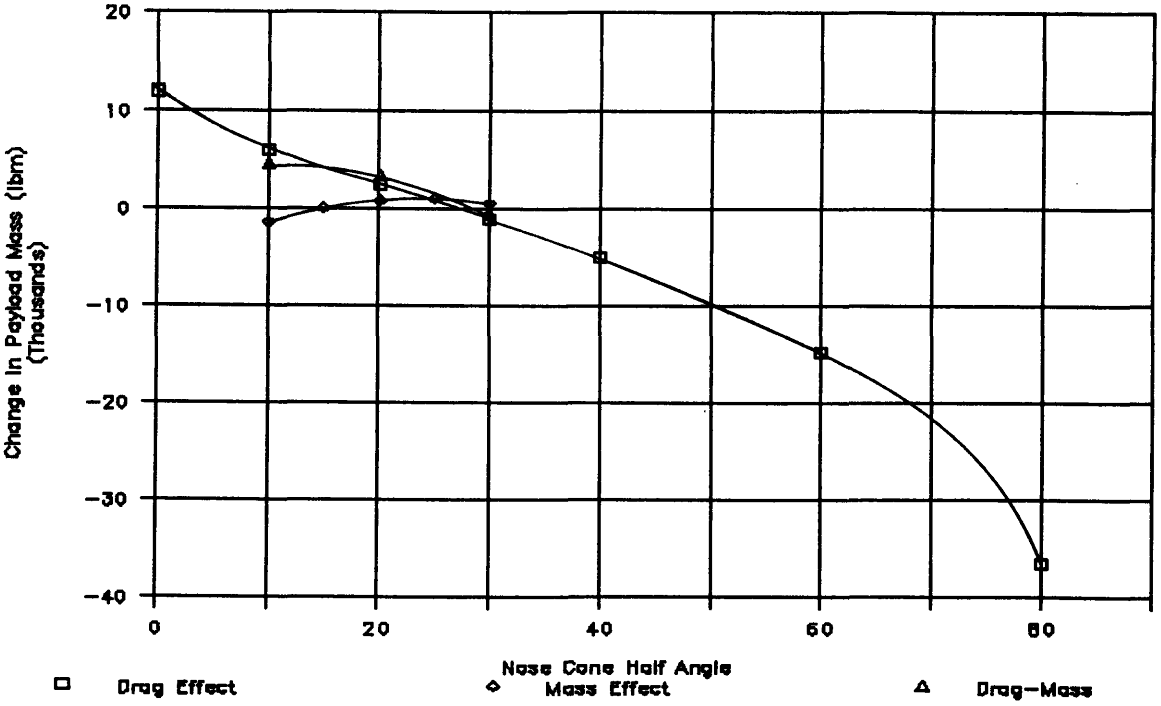

Figure 5.29: **The Effects of Drag and Mass when r=8**

heading "Drag-Mass." Though Table 2.1 only allows this difference to be computed for angles from 10° to 30°, the optimum *ascent* nose cone half angle is shown to occur when $r = 0$ and $\theta = 18^o$. This provides an improvement of about 7000 lb in the payload capability. Increasing the value of the tip radius gradually reduces this optimum ascent angle to under 10° (see Figure 5.28) and the corresponding improvement to under 5000 lb. However, eventually the reductions in mass with increasing tip radius move this optimum angle back towards the optimum mass angle, as shown in Figure 5.29. The corresponding increase in drag serves to keep the improvement in payload mass under 5000 lb above the nominal.

Drag results for minimum drag nose cones were obtained by reducing the average drags obtained for nose cones with $r = 0$ by 10%. The surface areas were

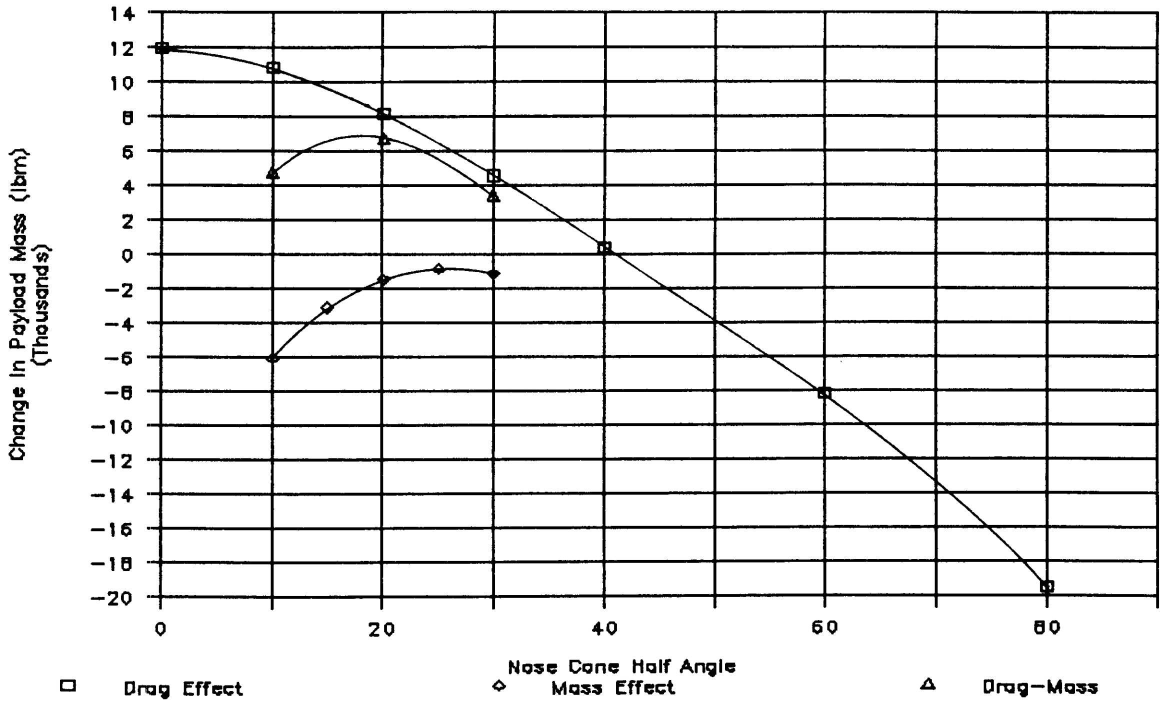

Figure 5.30: **The Effects of Drag and Mass for 2/3 Power Bodies**

computed for a two-thirds power body by iterating with the surface area program (Appendix B). These results are plotted in Figure 5.30. When compared to Figure 5.27, it shows that although the reduced drag in itself allows a slightly greater payload to orbit (this difference increases with cone angle), the corresponding increase in mass counteracts it. Comparing the "Drag-Mass" curves, it is shown that the minimum drag body has an optimum cone angle just slightly less than that of a cone, but with virtually the same performance improvement. However, on either side of this optimum angle the performance of the minimum drag body actually becomes less than that of an equivalent cone. Though these plots are admitedly very rough, it is felt that even if more detailed computations were to show a slight benefit from using minimum drag shapes, this would be counterbalanced by the

r (ft)	Θ	$\Delta(M_{PL})$ (lbm)
4	71	-20,600
5	58	-12,100
6	47	-11,900
7	42	-4900
8	37	-4100
9	31	-1300
10	22	1400
11	2	5000

Table 5.1: **The Effects of Drag on M_{PL} for Non-Ablating N/C's**

greatly increased manufacturing cost.

Finally, the drag effects of the non-ablating nose cones shown in Figure 5.7 were computed. The results are given in Table 5.1.

5.4 Ablation

As discussed in Section 5.1, using an ablative nose cone can provide substantial benefits in drag-reducing shapes. However, ablative materials are much heavier than non-ablative ones, and the corresponding increase in weight must be traded off with this reduction in drag. This section presents some preliminary results on mass increases due to ablation.

The calculation of the ablation rate is very complicated, as an ablating surface usually consists of a three-phase system of the original solid composite material and its liquid and gaseous forms. Now not only the reentry environment must be determined, but also details on the continuously changing shape and properties of the ablative material. A detailed calculation of ablation is beyond the scope of this work, but some approximate calculations for a conical shape were made using the Air Force Materials Laboratory Publication *Ablation Handbook, Entry Materials Data and Design* [51]. First of all, the change in velocity over time during the reentry was calculated using Equation 3.5 and the following equation for the terminal velocity:

$$V_{term} = (\frac{2Mg_o}{\rho_o C_D A} e^{\lambda y})^{\frac{1}{2}} .$$

In addition, the following equation was used to calculate the equivalent change in time:

$$\Delta t = \Delta y \, V \sin \gamma_E$$

where γ_E is the entry angle. Reference [51] was then used to calculate the stagnation enthalpy (H_s) at various altitudes as a function of velocity squared and the corresponding free-stream enthalpy (H_∞). Figure 1.6-5 in Reference [51] was next used to calculate the wall enthalpy as a function of the wall temperature of the ablating material, which was estimated as 4000^o R. A combination of figures and a formula gave the cold-wall heat flux ($\dot{q}_{cw}$) at various altitudes as a function of the ballistic coefficient, velocity, entry angle, the cone angle, and the distance (ξ) down the nose from the tip. The thermochemical heat of ablation (q^*) was estimated as a function of the stagnation enthalpy using Figure 1.7-2 in Reference [51], which was plotted from test data.[8] An approximate "hot wall" heat flux ($\dot{q}_{hw}$) for the ablative

---

[8] This data is for an ablative material with a phenolic resin and a refracil reinforcer.

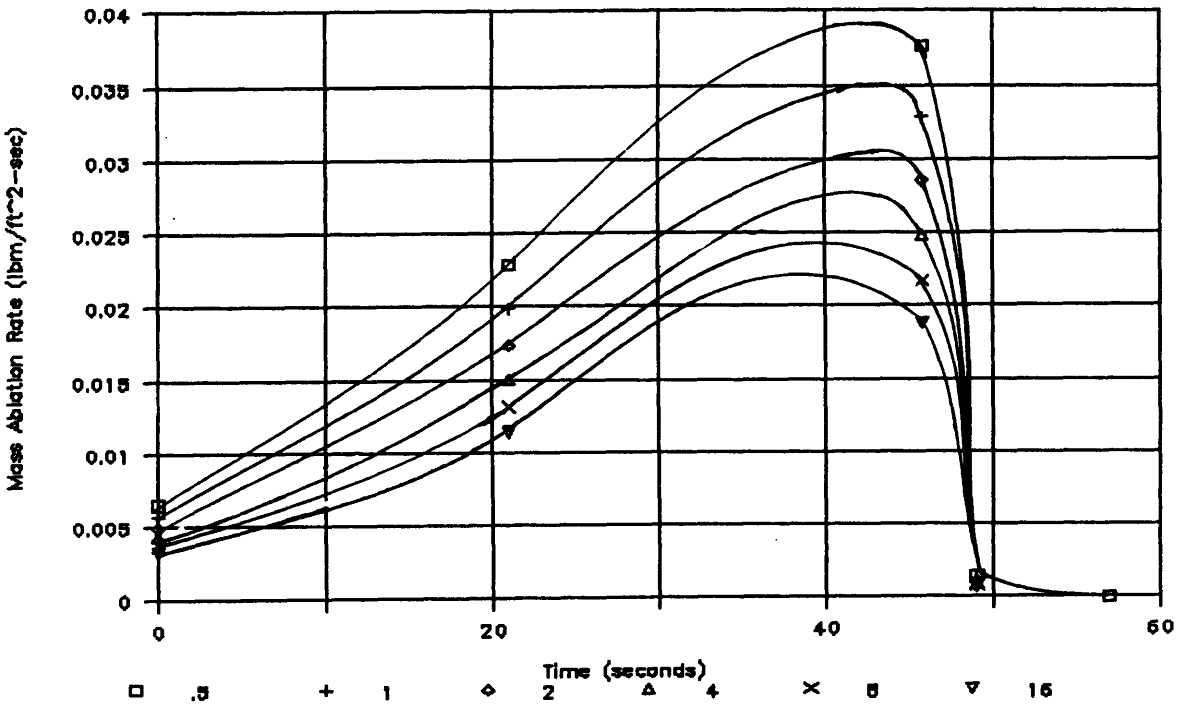

Figure 5.31: **Mass Flow Rate vs. Time for $\theta = 30.5^o$**

material was found with

$$\dot{q}_{hw} = \dot{q}_{cw}(1 - \frac{H_w}{H_s}),$$

and the final ablation rate was calculated using

$$\dot{m} = \dot{q}_{hw}/q^* \tag{5.4}$$

where $\dot{m}$ is the mass flow rate of the ablative material (Refracil Phenolic). The results for the 'nominal' nose cone (the half angle used was 30.5^o, but the source did not allow the small spherical tip to be figured in) at a variety of distances ξ from the nose tip are shown in Figure 5.31. The same calculations were made in Reference [51] on a reentering missile, and a peak rate of $\dot{m} = .75$ lbm/ft^2-sec was computed at $\xi = 1$ ft. A higher ablation rate is expected for the missile since it has a much larger ballistic coefficient ($W/(C_D A) = 3000$ lbs/ft^2 versus 180 lbs/ft^2 for the nominal JRB), a much faster entry speed at 23,600 ft/sec at an altitude of 300 kft, and a smaller cone half angle of 10°. The peak ablation rate for the JRB at a distance of $\xi = 1$ ft is less than $\dot{m} = .04$ lbm/ft^2-sec, a factor of 20 less than for the missile. This seems a bit excessive, and possible sources of error are discussed in Chapter 6.3.

The mass ablation rates given in Figure 5.31 were multiplied by their corresponding $\Delta t'$s, and the results summed to get a total volume of mass per unit area ablated at each point on the cone. When these results are integrated over the length of the cone the mass of the cone from the tip to each location is obtained. Equivalent results were calculated for a Nicalon-Nextel blanket (at .2886 lbm/ft^2) and used to obtain Figure 5.32. This figure shows the increase in mass of a partially ablative nose cone over a completely non-ablative nose cone which occurs if the ablative material starts at the tip of the nose cone and ends at a particular running distance down the side of the nose cone. For example, if the first eight feet of the nose cone are ablative, the nose cone will weigh about 45 lbs more than if it was totally non-ablative. A completely ablative noise cone is seen to have a weight increase of about 320 lbs.

Similar calculations were run on a cone with a half angle of 15°. The results are shown in Figure 5.33. This figure is very similar to Figure 5.32 for the 30.5° nose cone, with the completely ablative 15° nose cone having an increase in mass

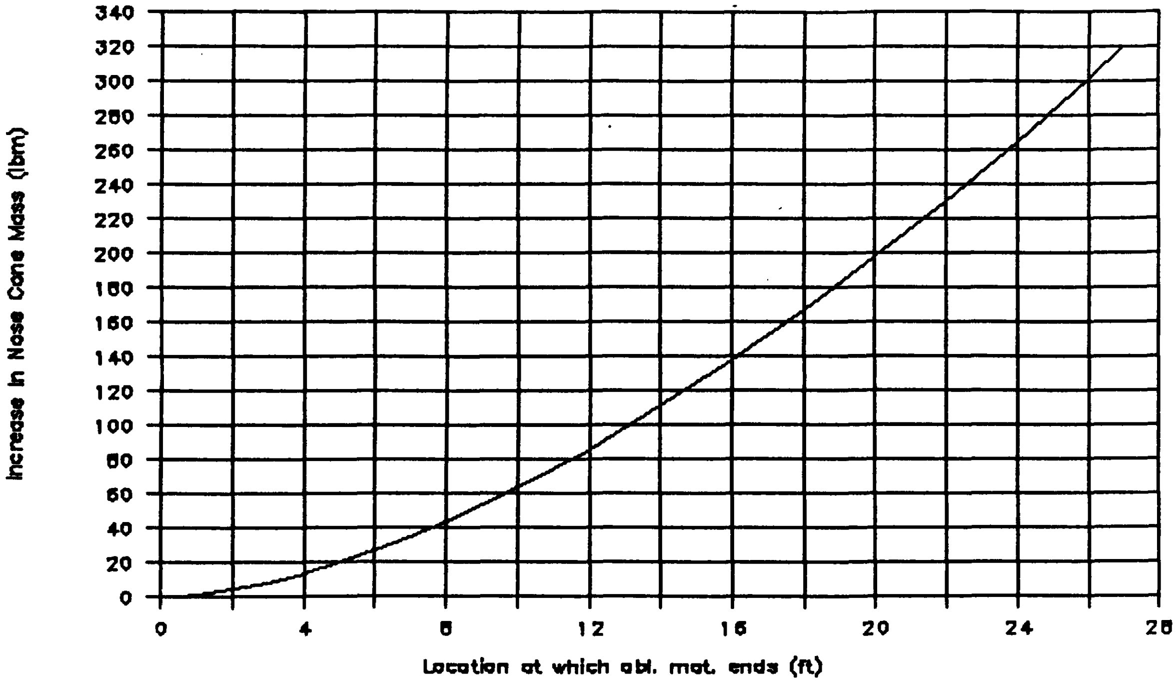

Figure 5.32: **Increase in N/C Mass Due to Ablative Materials** ($\theta = 30.5^o$)

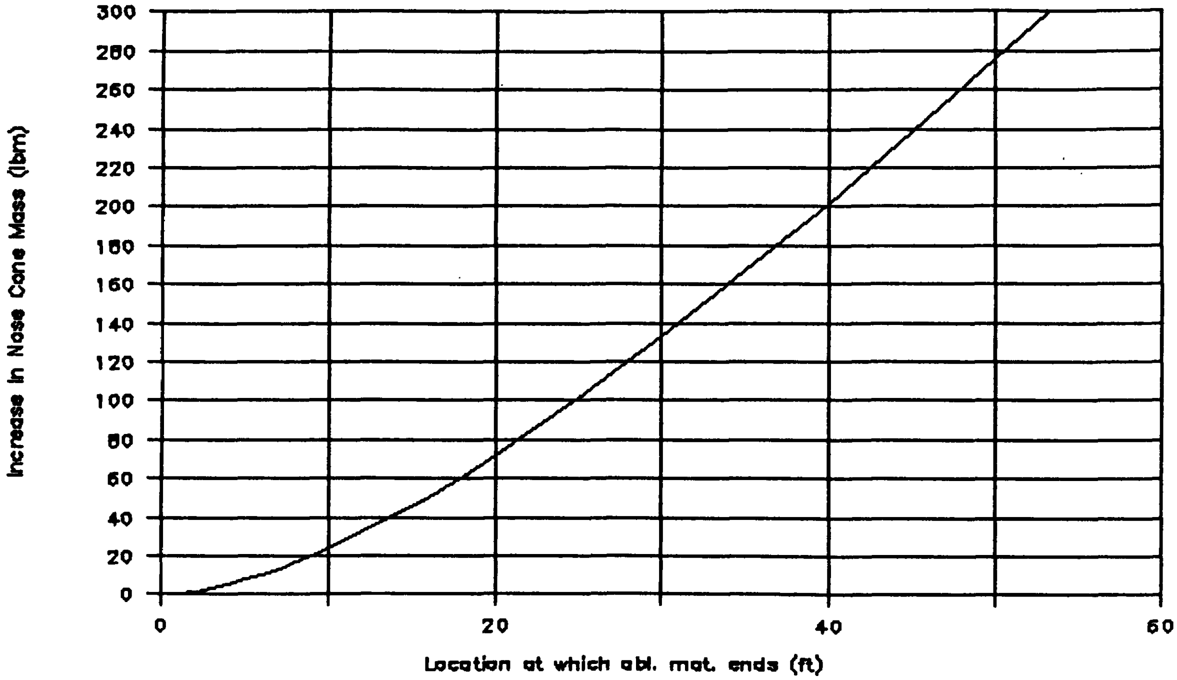

Figure 5.33: **Increase in N/C Mass Due to Ablative Materials** ($\theta = 15^o$)

of 300 lbs over the non-ablative case. The similarities between the ablative nose cones is caused by several factors. First of all, the 15° nose cone has a smaller coefficient of drag (it was approximated at $C_D \approx .19$) and thus reaches its terminal velocity almost 30,000 ft after the 30.5° nose cone.[9] The larger nose cone therefore decelerates much faster and sooner with high initial ablation rates, but the smaller nose cone ablates for a longer total period of time. In addition, the equation used for $\dot{q}_{cw}$ is proportional to $(\sin\theta)^{1.567}$ so that the larger nose cone has a greater equivalent value, yet the smaller nose cone has a much larger surface area to ablate.

---

[9] The 30.5° and 15° nose cones reach their terminal velocities at just over 30 kft and 60 kft, respectively.

Chapter 6

Conclusions

6.1 Introduction

This study has shown that there are a whole series of often interrelated forces which act on a reusable booster during each mission. When the booster is designed to reenter the atmosphere nose first (which is required by having reusable liquid rocket engines), altering the shape of this nose cone can have a decisive effect on these forces. This chapter will use the results from the previous chapter to obtain an "optimum" shape given several different criterion, and then will discuss the major sources of error and recommendations for further research.

6.2 Determining the Best Shape

The results from the water impact calculations and tests will be looked at first. Because the maximum impact force occurs during vertical entry, Figure 5.14 will be used to obtain a maximum cone angle and entry velocity. Limiting the impact force to well under 30 g's gives a maximum cone angle ranging from about 25° at $V_o = 30$ ft/sec to about 5° at $V_o = 80$ ft/sec. However, when the buoyancy force is included these angles are reduced even further. As seen in Figures 5.9 – 5.11, this effect is more pronounced for smaller nose cone angles. Because of this, it is felt that a nose cone half angle of 10° to 20° and an impact velocity of 30–40 ft/sec are necessary in order to at least have a chance of maintaining the structural integrity. However, the drop test results show that from a vehicle dynamics standpoint, a larger nose cone angle was better. This reduces both whip and rebound height. The test on the 20° nose cone at "40 ft/sec" did show a relatively mild reaction during rebound. However, as Figure 5.21 shows, the buoyancy force causes the booster to rebound to a height sufficient for an off-vertical initial impact case to have enough time on rebound for the booster to come down on its side or aft end with considerable force. Obviously, no matter what is done, a splash (and maybe impact) protection system will have to be devised to deploy over the engines/aft end before impact. Even so, this "second" impact must be kept to a minimum if the engines are going to survive.[1] The best way to do this is to prevent the buoyancy-rebound effect. This can be cone by increasing the nose cone angle, but it has already been shown that the corresponding impact force is too great. The alternative is to use a collapsable nose cone. This will serve to both attenuate impact forces and prevent rebound. The resulting vehicle impact dynamics will probably be like those described for the minimum heating shape. Along with the reduced buoyancy would come a deeper penetration depth and possible cavity collapse loads on the vehicle. However, both reducing the impact velocity and adding stiffener rings to the structure would counter the effects of these loads. (See page 71.) Though the booster would no longer be completely reusable, the engines are the expensive portion of it, and a replaceable nose cone can then be at least partially constructed out of ablative materials. In addition, having the nose cone collapsible on impact reduces the constraints on the shape and allows it to be optimized for drag, mass, and heating.

First of all, as Figure 5.30 and the corresponding discussion show, a minimum drag body does not improve the performance any measurable amount, and may actually lower it. If the nose cone is expendable, the increased costs of manufacturing such a shape would have to be justified. Because, unlike a fairing, the booster nose cone is not used to house anything, there is less of a need for a cone-frustum

---

[1] Survive here means to undergo no expected damage, since the cost of testing, fixing, and requalifying a large number of liquid engines would most likely make expendable boosters the cheaper alternative.

combination. The configurations considered will thus be various cone angle and nose tip combinations.

Figure 5.6 shows the minimal tip radii needed for various nose cone half angles in order to prevent ablation. The performance penalties due to drag for many of these configurations are given in Table 5.1. Since these shapes are quite different from those in Table 2.1, no mass penalties were computed. However, the nose cone with $r = 11$ ft and $\theta = 2^o$ obviously has a mass penalty which will more than overcome the drag improvement of 5000 lbs. Using Figures 5.27, 5.28, and 5.29, the total effect on the payload can be roughly estimated for the other nose cones in Table 5.1. The best nose cone thus obtained has a half angle of about 20^o with a corresponding tip radius of 10.1 ft. The effect on performance is most likely a gain of about 1000 lbs of payload over the nominal case.[2]

Allowing at least part of the cone to ablate on reentry can have a substantial improvement on drag however. As shown in Figures 5.27–5.29, reducing the tip radius increases the mass to orbit by thousands of pounds, and reducing the cone angle can increase this payload mass by up to tens of thousands of pounds. Figures 5.1–5.5 show that the resulting heating is primarily confined to the stagnation regions on the hemispheres. Thus, just allowing the tip to ablate provides most of the improvement. Taking these factors into account, the best nose cone design would have a small half angle of around 20^o and a medium-sized tip radius. For

---

[2] As explained in the next section, these performance numbers are very rough, and should really only be used in comparison with other similarly derived numbers in this report.

example, a tip radius of 6 ft on a 20° cone would only ablate down to $\delta = 45^o$ (see Figure 5.2). This nose cone also has a gain of about 3000 lbs of payload over the nominal case. Minimizing the area which ablates provides two advantages. First of all, an ablating material may flow onto other non-ablating parts of the nose cone and vehicle, potentially increasing the heat conduction in these areas and damaging a radiative heat shield or the booster itself (which is to be reused). Secondly, ablative materials are much heavier than non-ablative ones, and thus could potentially greatly increase the nose cone mass. This latter effect was partially assessed in Section 5.4, and the mass increases calculated when an ablative material was used are apparently small enough (due to a small ablation rate) as to be within the error of the drag calculations. Assuming that this is an accurate assessment (the next section discusses some of the limitations of the ablation calculations), a completely ablative nose cone appears to be the best solution. Using Figure 5.27, a 15° cone half angle provides an increase in payload to orbit of around 7500 lbs over the nominal. Since the tip of such a cone would burn off immediately during reentry, and probably in an uneven fashion, it would be best to have a slightly blunted tip. This would not only reduce both the mass of ablative material and the nose cone structural mass slightly, but, as pointed out by Hoerner, a slightly blunted cone gives a shape that is closer to the parabolic minimum drag shapes, and thus would also reduce the drag [4, p. 18–5].

In summary, this study shows that for vehicles like the JRB, building a reusable nose cone that allows the rocket/booster to survive water impact with no damage is not possible. Making the nose cone collapseable (and thus expendable) is the best solution.[3] Such a nose cone can be designed arround performance and surviving reentry heating. The next decision to be made is how much, if any, of the nose cone should ablate. The three nose cones arrived at for non-ablative, partially ablative, and ablative heat shields are shown on the JRB in Figure 6.1.

6.3 Sources of Error

This study has examined the relationship between various nose cone shapes and the forces acting on them by using the best simplified techniques the author could find. However, many approximations had to be made in order to obtain workable results. Though these were justified because the majority of the study dealt with comparisons between different nose cone configurations, the actual values obtained for things like impact force, mass, drag, and heating, should be regarded as rough approximations. Because of this, the results should be considered as a "first cut" only. They can be used to provide a guideline until more detailed studies like those discussed in Section 6.4 can be done. Specific sources of error and their relative magnitudes are now covered.

The calculation of drag was reliant on the results of the *Datcom*. It is felt that

---

[3] Deployable impact attenuators could also work, but they are an additional system which both adds weight and reduces reliability.

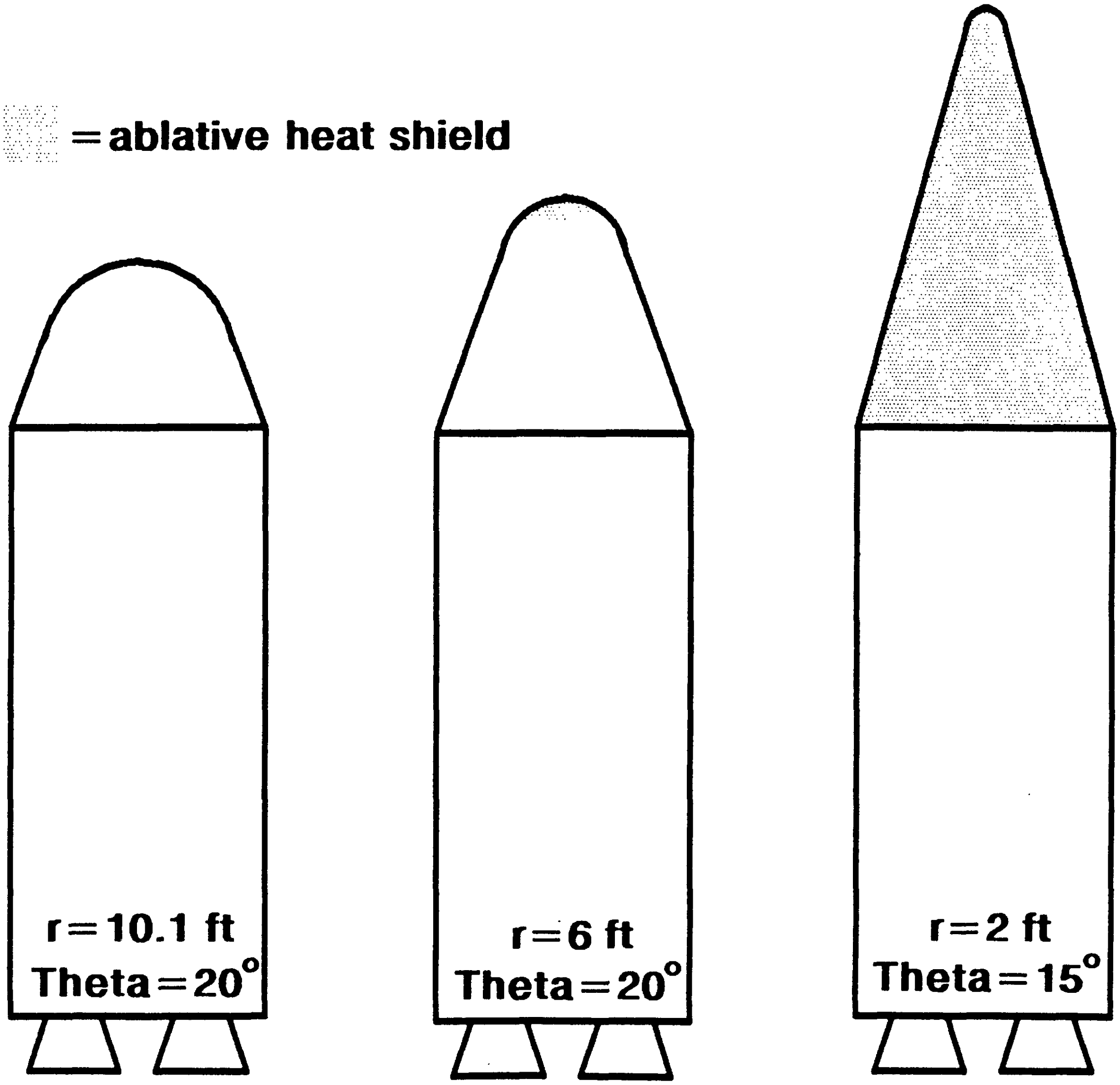

Figure 6.1: "Best Nose Cones"

overall the calculated C_D's were fairly accurate, however in the transonic range they were very approximate. Since it was in this range that the peak dynamic pressures occured, the corresponding values of average drag are reduced in accuracy. Though the skin friction drag was assumed to be turbulent for every case, it was only a small part of the total C_D. In addition, the shapes conducive to a higher value of R_{tran}, and thus a reduced C_f, were those which had the least overall relative drag. (See page 29.) As mentioned previously, though the base drag was assumed constant it was actually larger for bodies with smaller forebody drags. However, the fact that C_{DB} is much less than C_D shows that this influence is very small. Finally, the influences of interference drag in subsonic flow and the Mach wave off of the fairing in supersonic flow should be better approximated in Equation 2.15. These effects are very difficult to estimate, and are one of the largest sources of error in the drag calculations.

The mass calculations were obviously very rough. Though the results for the Saturn V fairings given in Table 2.1 are fairly accurate, they encompass a very small range of shapes. Approximating the JRB nose cone masses using them in the manner explained gave reasonably correct values for conical shapes, however, the larger the spherical tip, the greater the chance for error. As in other calculations, these results are most valuable when used to compare various nose cones.

The greatest potential for error in the heating calculations is in Equations 3.8 and 3.9. In these equations assumptions like a spherical surface, a Prandtl number of unity, and incompressible flow reduce their accuracy. The values of C_D and P_s obtained are well within the accuracy of these equations, and Equations 3.6 and 3.7 are highly accurate for this stage of the study.

As shown by the miscalculation in SRB loads (see page 71), water impact calculations are very difficult, and really require both a detailed understanding of the problem and well-executed drop tests. The Von Kármán-type theory used (Equations 4.2 and 4.3) assumed a vertical impact, neglected gravity and buoyancy forces, assumed a constant $V = V_o$ at several points in its derivation, and approximated the nose cones as ellipsoids. The assumption of vertical impact was fine, since this is the condition when maximum loads occur, and gravity is very small compared to the loads obtained. The assumptions of constant velocity do limit the accuracy of the equation, but should still provide a reasonably accurate picture of the loading until maximum forces occur. Though approximating the nose cones as ellipsoids does prevent comparisons between different shapes with the same cone angle, this approximation is about as accurate a simple representation as possible. Finally, it is the buoyancy force which appears to have the greatest effect on the results. For small nose cone angles it is often larger than the "impact force." Because the relationship between the buoyancy force and the impact force for light boosters is unknown at his time, the results of Equation 4.2 must be considered very conservative for nose cone half angles below about 30°.

The model tests conducted are felt to present an accurate reflection of the dynamics of the full-scale booster. Though there is no other similar test data available to compare with, the theoretical calculations (especially with respect to the magnitude of the buoyancy force) support these results. Possible small sources of error include the following: Though the model did not visibly deform, it was not modeled elastically to the full-scale version and small deformations may have incorrectly attenuated some of the impact forces. The use of additional scaling relationships could also help increase the accuracy. For example, modeling the atmospheric pressure and density using K_P and K_D, called cavitation-number and gass-density scaling, respectively, would help insure accurate modeling of the cavity forces since both the pressure and density act to close the cavity.[4] In addition, the test data showed that in most cases water clung to the nose cone on rebound and may have attenuated some of the rebound force/height. This was caused in part by surface tension, so thus an attempt at scaling the surface tension may improve the results. In order to scale the surface tension the following scale factor must be used: $K_\sigma = (1.0)(K_L^{\frac{1}{2}})^2(K_L)/(1.0) = K_L^2$. This shows that the surface tension for the model should *ideally* be several orders of magnitude smaller than it is, and any reduction in the surface tension would be beneficial.

Finally, though the ablation analysis conducted in Section 5.4 was very approximate, it at least provides a general feel of the magnitude of the effects of using an ablative heat shield. The trajectory calculations and approximations used in Refer-

---

[4] See page 4 in Reference [37].

ence [51] were from Allen and Eggers [20], and are used with a heating analysis to obtain the equation and plots for $\dot{q}_{cw}$. Though this equation is supposed to be for convective heating, its only relationship to nose cone geometry has $\dot{q}_{cw} \propto (\sin\theta)^{1.567}$, as previously mentioned. Thus, larger nose cones at the same altitude experience greater heating,[5] which is not correct for the JRB trajectory. It most likely was derived for faster vehicles like missiles, which experience some radiative heating. The calculation of H_w is also very rough, since it is reliant on a wall temperature which must be estimated from the reentry trajectory (or obtained through testing). The calculation of H_s is much more accurate, for the formula used was found to compare accurately to a detailed computer calculation. This leaves q^*, which is reasonably accurate since it comes from test data. Now, assuming a negligible radiative heat flux, the solution to Equation 5.4 is obtained from these other results. Since both nose cones had low ballistic coefficients and stopped ablating before terminal velocity was reached, a more detailed computation should also compute the heating during this portion of the flight. This heating must, in combination with the heat absorbed during ablation, remain low enough for the vehicle skin. The maximum heat that can be absorbed during ablation is thus limited this way. With all of these limitations, individual nose cone ablation comparisons are not very accurate, yet at least an approximate feel for the magnitude of this ablation has been obtained.

---

[5] This is counterballanced by its much stronger proportionality to velocity, which is reduced for the higher drag, lower heating nose cones.

6.4 Suggestions for Future Research

Although this study provides a starting point for designing a booster nose cone, more advanced studies would obviously have to be done before a final design is settled on. These should involve the following:

- Drag Calculations
    - Improve the estimates of transonic C_D's by testing boosters with different nose cones in a wind tunnel.
    - Improve the estimates of interference drag and shock wave interference effects by testing models of the full launch vehicle configuration in a wind tunnel.
    - Include the effects of lift in the trajectory data used.
- Mass Calculations
    - Design the nose cone structures (skin thickness and support ring placements) using data from a finite element code which analyzes the forces the cone will see.
- Heating Calculations
    - Use a detailed software package (many are available) to calculate the heating over the whole trajectory, and thus the maximum heat flux at various locations.

  - Use this program to compute the various temperature gradients and the total heat input and use these values to select a nose cone/thermal protection system.

- Water Impact Calculations
  - Use more advanced theoretical models of water impact in order to account for some of the following: F_b, spherically-tipped cones, $V \neq$ const., and $\alpha \neq 0$.
  - Testing
    - Model the booster elastically using K_I in Table 4.3. (This may require pressurizing the inside of the model.)
    - If feasible, use cavitation-number and gas-density scaling.
    - Reduce the surface tension of the water by adding very small amounts of Aerosol. ("A solution of .1% Aerosol by weight results in ... a reduction of 47%" of the surface tension.)[6]
    - Conduct a series of tests on impact at a variety of angles to help define the whip of the booster.
- Ablation
  - Use a detailed software package with current data to calculate the ablation rates, and thus the total mass of the heat shield.

---

[6] See page 5 in Reference [37]

  - Look into recently developed ablative materials.
  - Study the possible effects ablation has on a non-ablative part of the nose cone and on the booster.
- Cost (This was not covered in this study, but obviously must be considered in future ones.)
  - Determine the manufacturing costs for a variety of nose cone shapes.
  - Convert what this study has used for comparison — payload mass to orbit — to dollars so that it can be compared to relative manufacturing and operations costs for different nose cones.

On a more general note, during the course of this study it was discovered that there is virtually no information available on the water impact of structures as light as the booster tested. It is thus recommended that future work be done in the impact testing of buoyant structures. Open areas include analyzing how various nose cone geometries affect the increased forces, the rebound height, and the "second impact" which occurs.

Appendix A

Nomenclature

Note Additional symbols are used in this thesis, however they are defined when used. In addition, a few of the symbols below have different meanings on certain pages—they are redefined on those pages when this is the case.

A = cross-sectional area (ft^2)

C_D = total coefficient of drag

C_{DB} = coefficient of base drag

C_{DP} = coefficient of pressure drag

C_{FB} = coefficient of forebody skin friction drag

C_f = coefficient of skin friction drag

C_f' = equivalent skin friction coefficient (see Equation 3.4)

C_x = $D_w/(q_w A) \equiv$ axial force coefficient

D = drag (lb)

F = force (lb)

Fr = $V^2/(gL) \equiv$ Froude number

H = enthalpy (Btu/lbm)

I_{sp} = specific impulse

JLV = Jarvis Launch Vehicle

JRB = Jarvis Recoverable Booster

K = scale factor

L = characteristic length (ft)

M = mass of the booster (slugs)

M_{PL} = payload mass (slugs)

M_{Sat} = mass of Saturn V fairing (lb)

M_∞ = free-stream Mach number

N/C = nose cone

P = pressure (lb/ft^2)

R = radius of the base of the nose cone (ft)

R_e = radius of the Earth (ft)

$R_l = Vl\rho/\mu \equiv$ Reynolds number of the body dimension l

S = surface area (ft^2)

S_w = surface area of the submerged portion of the booster (ft^2)

T = temperature (R)

T' = thrust (lb)

V = velocity (ft/sec)

V' = volume (ft^3)

$W = (\rho_w V^2 L)/\sigma \equiv$ Weber number

$W/(C_D A) \equiv$ ballistic coefficient (lb/ft^2)

X = penetration depth (ft)

a = speed of sound (ft/sec)

g = acceleration due to gravity (ft/sec^2)

$g_o = 32.23$ ft/sec^2

h = height (ft)

k = coefficient used in the calculation of virtual mass (see Table 4.1)

m = virtual mass of water (slugs)

$\dot{m}$ = mass flow rate of exhaust (slugs/sec) (Chapter 2) or the ablative rate (lbm/ft^2-sec) (Chapter 5)

$q = \frac{1}{2}\rho V^2 \equiv$ dynamic pressure (lb/ft^2)

$\dot{q}$ = heat flux (Btu/ft^2-sec)

q^* = thermochemical heat of ablation (Btu/lb)

r = nose radius (ft)

t = time (sec)

t_B = total ascent burn time (sec)

t' = skin thickness (ft)

u = exhaust velocity (ft/sec)

y = altitude (ft)

α = entry angle (angle between the booster's longitudinal axis and the normal to the water's suface)

β = angle between the booster axis and the velocity vector

$\gamma = \rho g$ = specific gravity (lb/ft^3)

γ_E = reentry angle

δ = angle to the axis of revolution (see Figure 3.1)

ϵ = emissivity

θ = nose cone half angle

$\lambda = \frac{1}{22{,}000}\ \text{ft}^{-1}$

μ = viscosity

ξ = running distance down the nose cone from the tip (ft)

π = dimensionless product

ρ = density (slugs/ft^3)

ρ_0 = .0034 slugs/ft^3

σ = either the Stefan-Boltzmann constant (Chapter 3) or the surface tension (Chapter 4)

τ = either the fineness ratio (diameter/length) or the skin friction

ψ = angle between the free-stream direction and the tangent to the body

Subscripts

A = air

B = at the base of the nose cone

E = at an altitude of 200 kft (effectively the beginning of the atmosphere)

a = atmospheric

ave = average value (over an integral)

b = buoyancy

cw = cold wall (when $T = 0^o$ R)

e = at the exit plane of the engine nozzle

f = either the final condition (Chapter 2), skin friction (Chapter 2), or the full-sized booster (Chapter 4)

hw = hot wall (actual)

lam = laminar flow

m = booster model

mat = model construction material

o = at either the initial condition (Chapter 2), the stagnation point (Chapter 3), or water impact (Chapter 4)

p = pressure

s = stagnation

$term$ = terminal

$tran$ = transition region

w = water

wi = wind

∞ = free-stream

Appendix B

Surface Area Program

```
10 'This program computes the surface area of different nose cones.
20 '***Initialize variables***
30 LTCHECK=0: Y=0: ST=0: D=10: DIM L(D), CHOICE(D), S(D)
40 DIM M(40),N(40)
50 PI=3.14159: RADIUS=0: N=1: MARK=0
60 PRINT
70 PRINT"How can the shape of the nose cone best be approximated-"
80 PRINT"           A-as either a formula or a set of data points, or"
90 PRINT"           B-as a particular geometric shape?"
100 Q$=INKEY$: IF Q$="" THEN 100
110 IF (Q$="A") OR (Q$="B") THEN GOTO 120 ELSE PRINT"Not a valid entry":GOTO 70
120 IF Q$="A" THEN CHOICE(1)=4: MARK=1: GOTO 290
130 PRINT
140 INPUT"What is the radius of the base of the nose cone (in inches)";R
150 INPUT"What is the total length of the nose cone (in inches)";LT
160 INPUT"How many different sections can it be divided into";N
170 '***Initialize arrays***
180 FOR I=1 TO N
190     L(I)=0: CHOICE(I)=0: S(I)=0
200 NEXT I
210 '***Input the lengths of each section.***
220 FOR I=1 TO N-1
230     PRINT"Parallel to the booster's longitudinal axis,";
240     PRINT"how long (in inches) is section ";I;
250     INPUT L(I)
260     LTCHECK=LTCHECK+L(I)
270 NEXT I
280 L(I)=LT-LTCHECK
290 FOR I=1 TO N
300     IF MARK=1 THEN GOTO 410
310     Z=3
320     PRINT"How would you describe section ";I;"?"
330     PRINT"          (1) As a cone"
340     PRINT"          (2) As a cylinder"
350     IF I=1 THEN PRINT"          (3) As the tip of a sphere":Z=4
360     Q$=INKEY$: IF Q$="" THEN GOTO 360
370     IF (Q$="1") OR (Q$="2") THEN GOTO 390
380     IF Q$="3" THEN GOTO 390 ELSE PRINT"Not a valid entry":GOTO 320
390     CHOICE(I)=VAL(Q$)
400     IF (CHOICE(I)<0) OR (CHOICE(I)>Z+1) THEN PRINT"Try again:":GOTO 310
410     '***Go to the proper subroutine to compute the surface area of***
420     '***the section.                                              ***
430     IF CHOICE(I)=1 THEN GOSUB 500
440     IF CHOICE(I)=2 THEN GOSUB 640
450     IF CHOICE(I)=3 THEN GOSUB 1350
460     IF CHOICE(I)=4 THEN GOSUB 730
470     ST=ST+S(I)
```

```
480 NEXT I
490 GOTO 1570
500 '**********************************************************
510 '***This subroutine computes the surface area of a cone.***
520 RA=RADIUS
530 IF I<>N THEN INPUT"What is the radius at the end of the cone";RB ELSE RB=R
540 INPUT"What is the half-angle of the cone (in degrees)";OMEGA
550 OMEGA=OMEGA*PI/180:'Convert OMEGA to radians.
560 '***Check to make sure this is a valid value for omega.***
570 N=INT(OMEGA*100)/100
580 IF N=INT(100*ATN((RB-RA)/L(I)))/100 THEN GOTO 600
590 PRINT"This is not a valid half-angle.":GOTO 1620
600 S(I)=(PI/(SIN(OMEGA)))*(RB^2-RA^2)
610 IF I=1 THEN S(I)=S(I)+PI*RA^2:'Allow for a flat ended cone,
620 RADIUS=RB
630 RETURN
640 '**************************************************************
650 '***This subroutine computes the surface area of a cylinder.***
660 IF I>1 THEN GOTO 700
670 IF N=1 THEN RADIUS=R: GOTO 700
680 INPUT "What is the radius of this section (in inches)";RADIUS
690 PI=3.14159
700 S(I)=PI*2*RADIUS*L(I)
710 IF I=1 THEN S(I)=S(I)+PI*RADIUS^2:'Allow for a cylinder at the tip.
720 RETURN
730 '************************************************************
740 '***This subroutine computes the surface area of a segment***
750 '***represented by a formula or a set of data points.     ***
760 PRINT
770 PRINT"Do you want to enter a formula (F) or data points (D)?"
780 Q$=INKEY$: IF Q$="" THEN 780
790 IF (Q$="F") OR (Q$="D") THEN GOTO 810 ELSE PRINT"Not a valid entry."
800 GOTO 770
810 IF Q$="D" THEN GOTO 1060
820 '***This section solves for the area with a formula.***
830 GOSUB 1420
840 PRINT"1-Using the coordinate system shown above, enter the formula"
850 PRINT"      in the form y=f(x), preceded by the line number 1000."
860 PRINT"      (The top of the nose cone is at (0,0), the x-axis is"
870 PRINT"      equivalent to the longitudinal axis, and the base is"
880 PRINT"      located at (x',y')."
890 PRINT"2-Then type in the formula for dy/dx, in the form d(y)/dx=f(x),"
900 PRINT"      preceded by the line number 1010."
910 PRINT"3-Next type the command <RUN 930>."
920 STOP
930 INPUT"What is the radius of the 'leading edge' in inches";A
940 INPUT"What is the radius at the base of the nose cone (in inches)";R
950 INPUT"What is the total length of the nose cone (in inches)";LT
960 INPUT"How many iteration steps should be used";ITER
970 W0=LT/ITER:'Set the integration "slice width"
980 PI=3.14159
990 FOR X=A TO LT STEP W0
1000     'This line is where the formula y=f(x) goes.
1010     'This line is where the formula for d(y)/dx goes.
1020     W=W0*SQR(1+(DY)^2)
1030     ST=(Y*2*PI)*W+ST
1040 NEXT X
1050 GOTO 490
1060 '***This section solves for the area with a set of data points.***
1070 PRINT
1080 INPUT"What is the radius at the base of the nose cone (in inches)";R
1090 INPUT"What is the total length of the nose cone (in inches)";LT
1100 INPUT"How many data points will be entered";DP
1110 GOSUB 1420
1120 PRINT"Please enter the data points in pairs, in the form X,Y."
1130 FOR X=1 TO DP
```

```
1140    INPUT M(X),N(X)
1150    IF M(1)=0 THEN GOTO 1180
1160    PRINT"The x-value of the first data point must be zero.";
1170    PRINT "Please reenter this data","point:": GOTO 1130
1180 NEXT X
1190 CHECK=INT(M(DP)+.5)
1200 IF CHECK=INT(N(DP)*LT/R+.5) THEN GOTO 1250
1210 PRINT"The ratio of the last two data points, ";M(DP);"/";N(DP);"=";
1220 PRINT M(DP)/N(DP);","
1230 PRINT "does not correspond to the ratio of the length to the radius."
1240 PRINT "(";LT;"/";R;"=";LT/R;").": GOTO 1620
1250 FOR X=1 TO DP
1260    M(X)=M(X)*LT/M(DP): N(X)=N(X)*R/N(DP)
1270 NEXT X
1280 FOR X=1 TO DP
1290    IF X=1 THEN DS=SQR(((M(X+1)-M(X))/2)^2+((N(X+1)-N(X))/2)^2): GOTO 1320
1300    IF X=DP THEN DS=SQR(((M(X)-M(X-1))/2)^2+((N(X)-N(X-1))/2)^2):GOTO 1320
1310    DS=SQR(((M(X+1)-M(X-1))/2)^2+((N(X+1)-N(X-1))/2)^2)
1320    ST=N(X)*2*PI*DS+ST
1330 NEXT X
1340 RETURN
1350 '**********************************************************
1360 '***This subroutine computes the surface area of part of***
1370 '***a spherical section.                                ***
1380 INPUT"What is the radius at the end of this spherical tip";RADIUS
1390 S(I)=2*PI*RADIUS*L(I)
1400 RADIUS=SQR(2*RADIUS*L(I)-L(I)^2)
1410 RETURN
1420 '**********************************************
1430 '***This subroutine prints out an example of***
1440 '***the coordinate system used for option #4***
1450 PRINT "                          ";CHR$(24)
1460 PRINT "                        y ";CHR$(179)
1470 FOR G=1 TO 9
1480     PRINT "                          ";CHR$(179)
1490 NEXT G
1500 PRINT "                         ";CHR$(192);
1510 FOR G=1 TO 25
1520     PRINT CHR$(196);
1530 NEXT G
1540 PRINT CHR$(26)
1550 PRINT "                                                  x"
1560 RETURN
1570 '******************************************************************
1580 '*****This part of the program rounds of the value for surface*****
1590 '*****area and prints it out.                                 *****
1600 ST=INT(ST+.5)
1610 PRINT"The total surface area is ";ST;" square inches."
1620 END
```

Bibliography

[1] E. S. Hendrix and D. L. Baccus, "Launch Vehicle Nose Shroud Optimization," NASA Report N66-22331, 1966.

[2] M. Summerfield and H. S. Seifert, "Flight Performance of a Rocket in Straight-line Motion," in *Space Technology,* John Wiley and Sons, Inc., New York, 1959.

[3] J. N. Nielson, *Missile Aerodynamics,* McGraw-Hill Book Company, Inc., New York, 1960.

[4] S. F. Hoerner, *Fluid Dynamic Drag,* Copywright 1965 by Sighard F. Hoerner.

[5] W. G. Vincenti and C. H. Kruger, Jr., *Introduction to Physical Gas Dynamics,* Robert E. Krieger Publishing Company, Malabar, Florida, 1965.

[6] A. M. Kuethe and C. Chow, *Foundations of Aerodynamics: Bases of Aerodynamic Design,* Third Edition, John Wiley & Sons, New York, 1976.

[7] H. W. Liepmann and A. Roshko, *Elements of Gasdynamics,* John Wiley & Sons, Inc., New York, 1957.

[8] T. Von Kármán, "The Problem of Resistance in Compressible Fluids," GALCIT Pub. No. 75, 1936.

[9] H. M. Parker, "Minimum-Drag Ducted and Pointed Bodies of Revolution Based on Linearized Supersonic Theory," NACA Report 1213, 1955.

[10] C. Ferrari, "Bodies of Revolution Having Minimum Pressure Drag," in *Theory of Optimum Aerodynamic Shapes,* A. Miele ed., Academic Press, New York, 1965, pp. 103-124.

[11] A. Miele, ed.,*Theory of Optimum Aerodynamic Shapes,* Academic Press, New York, 1965.

[12] A. J. Eggers, Jr., M. M. Resnikoff, and D. H. Dennis, "Bodies of Revolution Having Minimum Drag at High Supersonic Speeds," NACA Report 1306, 1957.

[13] R. N. Cox and L. F. Crabtree, *Elements of Hypersonic Aerodynamics,* Academic Press, New York, 1965.

[14] L. H. Jorgensen, "Nose Shapes for Minimum Pressure Drag at Supersonic Mach Numbers," *Journal of Aeronautical Science,* Vol. 21, No. 4, pp. 276-279.

[15] R. D. Finck, principal investigator, *U.S.A.F. Stability and Control Datcom,* Flight Control Division, Air Force Flight Dynamics Laboratory, Wright-Patterson Air Force Base, Ohio, April 1978 revision.

[16] J. R. Wertz, "Spherical Geometry," Appendix A in *Spacecraft Attitude Determination and Control,* J. R. Wertz, ed., D. Reidel Publishing Company, Holland, 1985.

[17] G. B. Thomas and R. L. Finney, *Calculas and Analytic Geometry,* Fifth Edition, Addison-Wesley Publishing Company, MA, 1982.

[18] J. J. Martin, *Atmospheric Reentry—An Introduction to its Science and Engineering,* Prentice-Hall, Inc., Englewood Cliffs, N. J., 1966.

[19] L. Lees, "Recovery Dynamics—Heat Transfer at Hypersonic Speeds in a Planetary Atmosphere," in *Space Technology,* John Wiley and Sons, Inc., New York, 1959.

[20] H. Allen and A. J. Eggers Jr., "A Study of the Motion and Aerodynamic Heating of Ballistic Missiles Entering the Earth's Atmosphere at High Supersonic Speeds," NACA Report 1381, 1958.

[21] *U. S. Standard Atmosphere, 1976,* National Oceanic and Atmospheric Administration, NOAA-S/T 76-1562, Washington, D.C., October 1976.

[22] R. L. Trimpi, F. C. Grant, and N. B. Cohen, "Aerodynamic and Heating Problems of Advanced Reentry Vehicles," in *Aerodynamics of Space Vehicles,* NASA SP-23, 1962.

[23] J. D. Anderson, *Fundamentals of Aerodynamics,* McGraw-Hill Inc., New York, 1984.

[24] R. L. Baker and R. F. Kramer, "Evaluation of Total Heat Transfer in Hypersonic Flow Environments," Aerospace Corp., El Segundo, Calif., Rept. TR-0078(3550-15)-4, 1978.

[25] R. L. Baker and R. F. Kramer, "Nose-Tip Shape Optimization for Minimum Transpiration Coolant Requirements," AIAA Paper 77-780, 1977.

[26] R. Vaglio-Laurin, "Laminar Heat Transfer on Three-Dimensional Blunt Nosed Bodies in Hypersonic Flow," *ARS Journal,* pp. 123-129, February 1959.

[27] R. Vaglio-Laurin, "Turbulent Heat Transfer on Blunt-Nosed Bodies in Two-Dimensional and General Three-Dimensional Hypersonic Flow," *Journal of the Aero/Space Sciences,* January 1960.

[28] L. L. Perini, "Compilation and Correlation of Stagnation Convective Heating Rates on Spherical Bodies," *Journal of Spacecraft,* Vol. 12, No. 3, March 1975, pp. 189-190.

[29] R. K. Miyakawa and A. Rogers, "Launch Systems Integration — Aerothermal Analysis Report," Hughes Aircraft Company, SR31070-637, August 1978.

[30] R. Madden and D. A. Kross, "Scaling of Water Impact Data for Space Shuttle Solid Rocket Booster," *The Shock and Vibration Bulletin 44,* pp. 165-175, August 1974.

[31] R. T. Keefe, E. A. Rawls, and D. A. Kross, "Space Shuttle Solid Rocket Booster Water Entry Cavity Collapse Loads," N83-30694, *The Shock and Vibration Buletin 55,* pp. 21-26, May 1982.

[32] A. May, "Review of Water-Entry Theory and Data," AIAA Paper No. 70-531.

[33] S. V. Denk, "Water Entry Impact Shock on Flat Faced Cylindrical Missiles," Naval Surface Weapons Center, White Oak, Maryland, NSWC TR 82-438.

[34] E. A. Rawls and D. A. Kross, "A Study of the Space Shuttle Solid Rocket Booster Nozzle Water Impact Recovery Loads," *The Shock and Vibration Bulletin 46,* pp. 149-162, August 1976.

[35] J. O. Gurney, "A Preliminary Study of the Mechanism of Water-Entry Whip of 20° Cone Nosed Models," U. S. Naval Ordnance Laboratory, White Oak, Maryland, NOLTR 66-148.

[36] J. L. Baldwin, "An Experimental Investigation of the Axial Forces Generated by the Oblique Water Entry of Cones," *The Shock and Vibration Bulletin 46,* August 1976.

[37] J. G. Waugh and G. W. Stubstad, "Hydroballistics Modelling," Naval Undersea Center, San Diego, CA, distributed by NTIS, Report AD-A007 529, January 1975.

[38] A. A. Schmidt, D. A. Kross, and R. T. Keefe, "Water Impact Testing of a Filament Wound Case," N86-16652, *The Shock and Vibration Bulletin 55,* pp. 57-67, June 1985.

[39] T. Von Kármán, "The Impact of Seaplane Floats During Landing," NACA TN-321, 1929.

[40] M. Shiffman and D. C. Spencer, "The Force of Impact on a Cone Striking a Water Surface (Vertical Entry)," *Comm. Pure Appl. Math,* Vol. 4, No. 4, 1951, pp. 379–417.

[41] L. Trilling, "The Impact of a Body on a Water Surface at an Arbitrary Angle," *The Journal of Applied Physics,* Volume 21, February 1950.

[42] V. G. Szebehely and M. K. Ochi, "Hydrodynamic Impact and Water Entry," *Applied Mechanics Surveys,* Abramson et al., ed., Spartan, Washington D.C., 1966, pp. 951–957.

[43] C. F. Kettleborough, "Hydrodynamic Water Impact," N74-19915, March 1972.

[44] H. E. Benson, "Water Impact of the Apollo Spacecraft," *Journal of Spacecraft and Rockets,* Vol. 3, No. 8, pp. 1282-1284, August 1966.

[45] W. E. Baker and P. S. Westine, "Model Tests for Structural Response of Apollo Command Module to Water Impact," *Journal of Spacecraft and Rockets,* Vol. 4, No. 2, pp.201-208, February 1967.

[46] H. N. Abramson, "Hydroelasticity — Some Problems and Some Solutions," in *Fluid-Solid Interaction,* The American Society of Mechanical Engineers, New York, N. Y., 1967, pp. 187-222.

[47] A. M. Mackey, "A Mathematical Model of Water Entry," Admiralty Underwater Weapons Establishment, Portland, AUWE Technical Note No. 636/79, October 1979.

[48] R. C. Pankhurst, *Dimensional Analysis and Scale Factors,* The Institute of Physics and The Physical Society, Reinhold Publishing Corporation, New York, N. Y., 1964.

[49] H. L. Langhaar, *Dimensional Analysis and Theory of Models,* John Wiley & Sons, Inc., New York, N. Y., 1951.

[50] R. T. Savage, W. Love, and F. Bloetscher, "High Temperature Performance of Flexible Thermal Protection Materials," AIAA Paper No. 84-1770, 1982.

[51] C. J. Katsika, G. K. Castle, and J. S. Higgins, *Ablation Handbook, Entry Materials Data and Design,* Air Force Materials Laboratory, Wright-Patterson Air Force Base, Ohio, AFML-TR-66-262, November 1966.

[52] "Buckling of Thin-Walled Truncated Cones," *NASA Space Vehicle Design Criteria (Structures),* NASA SP-8019, September 1968.